Title

Evaluation of the performance of the oceanic hydrate accumulation at site NGHP-02-09 in the Krishna-Godavari Basin during a production test and during single and multi-well production scenarios

Authors

Moridis, George J
Reagan, Matthew T
Queiruga, Alejandro F
et al.

Publication Date

2019-10-01

DOI

10.1016/j.marpetgeo.2018.12.001

Peer reviewed

Evaluation of the Performance of the Oceanic Hydrate Accumulation at Site NGHP-02-09 in the Krishna-Godavari Basin During a Production Test and During Single and Multi Well Production Scenarios

George J. Moridis[1,2], Matthew T. Reagan[1*], Alejandro F. Queiruga[1], and Ray Boswell[3]

[1]: *Energy Geosciences Division, Lawrence Berkeley National Laboratory, Berkeley, CA 94720, USA*

[2]: *Petroleum Engineering Department, Texas A&M University, College Station, TX 77843, USA*

[3]: *U.S. Department of Energy, National Energy Technology Laboratory, Pittsburgh PA 15236, USA*

*: *Corresponding author.*

Keywords: Gas hydrates, geomechanical analysis, reservoir simulation, India National Gas Program

Abstract

The objective of this study is to quantify, by means of numerical simulation, the response of the complex system of gas hydrate accumulations at Site NGHP-02-09, Krishna-Godavari Basin, Indian Ocean, to different production conditions, and to determine the technical feasibility of gas production through depressurization-induced dissociation. The study assesses the suitability of the site for a long-term production test involving a single vertical well, and the long-term potential of the deposit under full-field production using a system of multiple vertical wells. We simulate gas and water flow, estimate the production performance of the accumulation and separately investigate the corresponding geomechanical response of the system. Results indicate that production from Site NGHP-02-09 under the conditions of a long-term field test involving a single vertical well is technically feasible and can yield high gas production rates. However, an inability to fully isolate the water bearing zones results in production that is largely from dissolved gas rather than hydrate dissociation and is thus burdened by excessive water production. Given the estimated physical properties of the reservoir system, Site NGHP-02-09 does not appear to be a promising location for a single-well field test of gas production, but may be a promising production target for full-field production operations using a multi-well system in which exterior wells can mitigate water inflows to allow interior wells to more effectively depressurize the formation and capture methane from gas hydrate dissociation. Geomechanical issues need to be carefully considered as significant displacements are possible, which can be challenging to well construction and stability.

1. Introduction

1.1. Background

The present study focuses on the analysis of a particular oceanic hydrate accumulation in the Krishna-Godavari Basin (hereafter referred to as the KG Basin) off the eastern coast of India, and its evaluation as a potential energy source and a hydrocarbon gas production target. More specifically, the hydrate deposit under investigation is located at Site NGHP-02-09 in the KG Basin that was recently drilled and cored during the National Gas Hydrate Program Expedition 02 (NGHP-02) that was conducted from 3-March-2015 to 28-July-2015 (Figure 1).

The NGHP-02 expedition involved participation and support by a large international team representing several government and private organizations and included a wide range of investigations. NGHP-02 downhole logging, coring and formation pressure testing confirmed the presence of large, highly saturated, gas hydrate accumulations in coarse-grained sand-rich depositional systems throughout the KG Basin within the regions defined during NGHP-02 as Area-B, Area-C, and Area-E (Figure 1). The existence of a fully developed gas hydrate petroleum system was established in Area-C of the KG Basin with the discovery of a large slope-basin interconnected depositional system, including a sand-rich, gas-hydrate-bearing channel-levee prospect at Sites NGHP-02-08 and -09 (*Collett et al., this issue*: Figure 2). The elevation (measured from the ocean surface) of the upper surface of a system of Hydrate-Bearing Sediments (HBS) in the vicinity of these sites is described in the contour plots of Figure 3. Further analysis of cores and geophysical data collected at these sites yielded important information on the system stratigraphy and hydrate occurrence, revealing a very complicated geology that involved a HBS sequence consisting of alternating layers of high-porosity hydrate bearing sandy layers, hydrate-free intervals of the same water-saturated sandy medium and mud/clay interlayers (Figure 4). Investigation of all available data showed that the gas hydrates at these sites have very desirable reservoir properties, i.e., high gas hydrate saturation S_H and high intrinsic and effective permeability (k and k_{rel}, respectively), making these accumulations ideal candidate sites for consideration of future gas hydrate production testing. The present study focuses its effort on Site NGHP-02-09.

1.2. Objectives

The objective of this study is to quantify, by means of numerical simulation, the response of the complex system of hydrate accumulations at Site NGHP-02-09 to different production conditions in an effort to determine: a) the technical feasibility of gas production through depressurization-induced dissociation, b) the suitability of the site for a production test of several months duration involving a single vertical well, and c) the long-term potential of the deposit as a hydrocarbon resource in a full-field production operation using a system of multiple vertical wells. The study predicts fluid (gas and water) flow and production performance of the accumulation through the analysis of the coupled flow, thermal and phase-change processes that occur during the course of production. These production estimates do not incorporate the effects of progressive reservoir compaction during depressurization. The corresponding geomechanical response of the geologic system is calculated separately, using one-way coupling to draw inputs from the production model at certain moments in time to provide estimates of the in situ stress fields, formation compaction and seafloor subsidence.

1.3. Cases investigated in this study and general approach

We investigated a total of 4 different cases that involved different geometries and production scenarios. These were the following:

(1) The reference case, hereafter referred to as *Case R*, which describes production from a radially infinite-acting (*open*) system using a single vertical well during a long-term (about 180 days) field test. The infinite-acting nature of this system is defined by radial boundaries located at a sufficiently large distance from the single vertical well called by the test design that their conditions and properties remain time-invariant during the test period. Through scoping calculations, we determined that a cylindrical system with a radius r = 2000 m satisfies these conditions. Case R is designed to address the issue of suitability of Site NGHP-02-09 as the location for the planned long-term field test of gas production from the hydrate accumulations of the KG Basin.

(2) *Case C1*, which describes production operations involving a system of vertical wells on a regular grid. The effect of multiple wells on a regular pattern creates conditions that approach no-flow boundaries of the drainage area of individual wells in the *interior* of the pattern. Here we provide production estimates by assuming no-flow boundaries exist, meaning we model a single interior well as a

closed system with no external source of fluid or heat. In Case C1, the distance between wells is 1000 m, the radius of the domain (drainage area) of each interior well is r = 500 m. Case C1 is designed to evaluate the potential of the hydrate deposit at Site NGHP-02-09 as a target for full-field reservoir development through multiple wells.

(3) *Cases C2* and *C3* are similar in concept to Case C1, from which they differ in the domain radius (r = 100 m and 75 m, respectively). The reason for investigating the three cases is to evaluate the effect of well spacing on the gas production performance from the NGHP-02-09 hydrate deposits under multi-well production operations.

All the simulations were conducted using a single set of flow, thermal, and geomechanical properties as reported in companion papers in this Special Volume (*ex., Yoneda et al., this issue-a,b; Waite et al., this issue*). Thus, the present study does not include a parametric sensitivity analysis of the system production performance and overall behavior in response to variations in the values of key flow, thermal and geomechanical conditions and properties and does not consider heterogeneity in any of these parameters. The enormous execution time requirements (hundreds of thousands of supercomputer hours and months of wall-clock time – see later discussion) needed to complete the study of the four cases using the standard set of properties and conditions precluded such an activity within the time frame of this study. As a result of the computational costs, it was infeasible to perform fully coupled simulations including geomechanics, and the geomechanical response was estimated by post-processing the results of the costly multiphase flow simulations.

2. System Description and Production Strategy

The discussion and analysis in this section is based on the data provided by the entire multinational team involved in the NGHP-02 scientific expedition and the subsequent study (as summarized in *Collett et al., this issue; Boswell et al., this issue; Kumar et al., this issue*). The methods used for the measurement and derivation of these data—and in the estimation of the relevant parameters, where direct measurements were not possible—are beyond the scope of this study and are not discussed in detail. Although a very large number of data were obtained in the course of the NGHP-02 expedition and the subsequent associated work, in the present modeling study we include and discuss only the data used in the simulations. The interested reader is directed to other relevant papers associated with the NGHP-02 expedition.

2.1. System description and geometry

The water depth at Site NGHP-02-09 of the KG Basin (see Figure 5) is 2,219.5 m. The available information at the time of the study indicated that the hydrate accumulation at a promising location at that site is buried under a relatively thin layer of 214.9 m of mud below the sea floor (Figures 3, 4, and 5). The complex, 53.6 m-thick system of the HBS sequence is characterized by 49 alternating layers of (a) hydrate-rich sands, (b) clays (muds) that are nearly devoid of hydrates, and (c) hydrate-free sands. Figure 5 shows a sketch of this system (based on the most recent data), and provides some basic information on the geology and geometry of the system such as the stratification, the thickness of the various layers and the texture of the corresponding sediments. The base of the gas hydrate stability zone (BGHSZ) is estimated to be well below the base of the hydrate accumulation, i.e., this is a thermodynamically stable system.

This complex, 53.6 m-thick hydrate-bearing system is overlain and underlain by very low-permeability boundaries, i.e., the mud overburden and assumed underburden, respectively (Figure 5). Based on experience gained in earlier studies (Moridis and Reagan, 2007a,b; Moridis et al., 2007; 2009a; 2013) and preliminary scoping calculations, the simulation domain extends from the ocean floor (the upper boundary of the domain) to a depth of 600 mbsf (Figure 5). This was necessary because the consideration of coupled flow, thermal, chemical and the one-way coupling to the geomechanical processes in this numerical study have effects that extend beyond the narrow confines of the hydrate-bearing sediments. The resulting dimensions of the simulation domain provided a representative reservoir description that (a) allowed heat and fluid exchanges between the deposit and its boundaries during the production period and (b) were shown to be sufficiently large to act as true boundaries for all processes considered in this study.

2.2. Classification of the hydrate deposit at Site NGHP-02-09

The analysis here hews very close to that of Moridis et al. (2013). Based on the geology and stratification indicated by Figure 5, the layered structure of the hydrate accumulation at Site NGHP-02-09 appears to be a combination of Class 2 and 3 systems, but can be better considered a hybrid of two hydrate classes (Moridis and Reagan, 2007a; 2007b Moridis et al., 2011; 2013): (a) Class 2, comprising a hydrate-bearing layer (HBL) overlying a zone of mobile water, and (b) Class 3, involving HBLs confined between two strata of near-zero permeability. Near the top of the HBL sequence, the features of a typical Class 2 deposit are dominant because of alternating HBL and hydrate free sands. The same can be said about the deeper mud interlayers (Figure 5), which are not impermeable. However, because of the very low permeability of the muds in the overburden, underburden and in the interlayers, the characteristics of a near-Class 3 deposit are evident toward the bottom of the 53.6 m-thick system. Note that, although the water mobility in the mud layers is limited, it is not zero, and this has implications in the course of production that will be discussed later.

2.3. Method of production and well design

Gas production necessitates hydrate dissociation. Because of the geology at Site NGHP-02-09 (involving the low-permeability overburden, underburden and 14 mud layers in contact with HBLs), depressurization is the most effective dissociation strategy for reasons explained in detail by Moridis and Reagan (2007a) and Moridis et al. (2009b). This is accomplished by constant-pressure production (involving a constant bottomhole pressure P_w at the well), which is desirable because of its simplicity, its technical and economic effectiveness, the fast response of hydrates to the rapidly propagating pressure wave, the near-incompressibility of water, and the large heat capacity of water. Because of the high initial hydrate saturation S_H in the HBL and the very low permeability of the muds in the interlayers, the effective permeability k_{eff} at the onset of gas production can be very low, and constant-rate production is impractical because the associated pressure drop is rapid, large, and very difficult to control, with a near certainty of ice formation and severe restriction (or even blockage) of flow to the well. On the other hand, pure thermal stimulation is an unattractive option because of its limited and ever decreasing effectiveness and efficiency (Moridis and Reagan, 2007a).

The use of horizontal wells was deemed impractical for the planned long-term field production test in the KG Basin due to the presence of alternating layers of highly permeable hydrate-free sand lenses and low intrinsic permeability mud interlayers, and the considerable cumulative thickness of the three types of units. Thus, vertical wells were used exclusively in the study. The simple well design uses a perforated interval that covers the entire 53.6 m-thickness of the hydrate-bearing interval. Alternative well completions were investigated and rejected that will be discussed later. A significant advantage of constant-P_w production is the elimination of the possibility of ice formation (with its consequent detrimental effects on permeability and gas production) through the selection of an appropriate P_w>P_Q (where P_Q is the quadruple point pressure, 2.56 MPa).

The use of vertical wells and the absence of any information on heterogeneity at the site (in particular) and in the KG Basin (in general) led to the use of a cylindrical domain in (r,z) that can be modeled as a 2D axisymmetric problem. In all studies, the well was located at r = 0 with radius r_w = 0.1 m. For the various cases of production we investigated, scoping calculations indicated that the domain radii and a total thickness of Δz = 600 m were sufficient to provide constant condition boundaries by confirming that the pressure, thermal and geomechanical disturbance caused by the bottomhole pressure did not reach these boundaries for the duration of the study period.

3. The Numerical Models and Simulation Approach

3.1. Numerical methodology and codes

The simulations are performed using the TOUGH+Millstone suite, comprised of the integral finite difference method simulator TOUGH+HYDRATE and the finite element method simulator Millstone. The TOUGH+HYDRATE code (T+H) can model all the known processes involved in the system response of natural CH_4-hydrates in complex geologic media (Moridis et al., 2014; Moridis and Pruess, 2014). T+H is a fully compositional simulator, descended directly from the TOUGH2 family of codes (Pruess et al., 1999; Pruess, 2003), and it accounts for heat and up to four mass components (i.e., H_2O, CH_4, CH_4-hydrate, and water-soluble inhibitors such as salts) that are partitioned among four possible phases (gas, aqueous liquid, ice, and hydrate). It can describe 15 possible thermodynamic states (phase combinations) of the CH_4+H_2O system and can handle the phase changes, state transitions, strong nonlinearities and sharp fronts that are typical of hydrate dissociation problems. Because of the very large computational requirements that are the norm in hydrate problems, both a serial and a parallel version (Zhang et al., 2008) of the code were used in this study. The T+H code has been used for a wide range of investigations of gas production from hydrates in both oceanic deposits and in accumulations associated with the permafrost that cover the entire spectrum of hydrate types, i.e., Class 1 (Moridis et al., 2007), Class 2 (Moridis and Reagan, 2007b; Moridis et al., 2011a; 2011b), Class 3 (Moridis and Reagan, 2007a; Moridis et al., 2011c), and Class 4 (Moridis and Sloan, 2007; Li et al., 2010; Moridis et al., 2011d). In addition, the code has been used extensively to model natural hydrates and environmental impacts (Thatcher et al., 2013; Marin-Moreno et al., 2015; Stranne et al., 2016). For this study, we activated 3 components, 4 phases, and 4 equations to model systems containing water, methane, and salt partitioned over gas, liquid, hydrate, and ice phases.

Geomechanical analysis of the new set of hydrate reservoirs is enabled by a new geomechanical simulation framework, Millstone (Moridis et al., 2017). Millstone solves the incremental stress formulation using the Finite Element Method with the standard Galerkin formulation with bilinear-quad nodal shape functions for displacement fields and Gauss point-centered stresses. A small-deformation linearized strain assumption is used at each increment, with elastic moduli that are functions of the flow variables. This code introduces two new key features: (1) use of a separate mesh for the mechanical solution, alleviating the frequent problem of the ill-conditioned linear systems; and, (2) formulations for plane-strain and axisymmetry using 2D elements (in addition to standard 3D Cartesian formulations). The Millstone code yields significant speed improvements by reducing system unknowns and improving the stability, conditioning and accuracy of the solution compared to earlier used geomechanical solvers based upon 3D formulations using one-volume-to-one-element coupling schemes. Millstone is typically operated embedded inside of the TOUGH+Hydrate simulation loop, wherein it solves the quasistatic balance of momentum inside of the nonlinear solution loop of the flow solver. The solver iterates between solving displacements and flow primary variables, performing interpolations of required fields back-and-forth between the two meshes, until convergence for each time step.

The computational cost of the highly-detailed system precluded the use of the complete two-way coupling between the flow and geomechanics, in which both systems are solved at every step of the Jacobian system until convergence. Beyond adding more unknowns, the inclusion of geomechanics in a coupled simulation greatly increases the cost by both increasing the number of iterations per time step (the staggered scheme does not have quadratic convergence) and decreasing the size of viable time steps due to the increased difficulty of solving the nonlinear equations. A time step sequential scheme, in which the geomechanics is solved only once per time step, performs worse due to smaller time step requirements.

Motivated by this problem, a two-stage simulation process was developed to estimate the geomechanical response with only one-way coupling. The time-varying pressure and saturation fields at snapshots from the flow simulation are used to solve the total stress and displacements. The complete analysis procedure has four stages:

1. Preprocessing to generate meshes and input files,
2. Running TOUGH+Hydrate on HPC resources to solve multiphase, multicomponent flow,
3. Running Millstone on workstation to solve displacements and stresses resulting from depressurization and hydrate dissociation, and
4. Postprocessing to calculate additional quantities of interest and generate plotting and visualization formats.

In this methodology, there is no feedback from the stress distributions to the flow problem, and as a result, the production values do not reflect potential reduction in production rates due to progressive reservoir consolidation (see Boswell et al.-b, this issue). The solution of the mechanics is linear and quasistatic in absence of the flow effects, and thus each case can be solved in only ten minutes on a desktop workstation given the flow fields to provide the estimates presented here. The open source tough_convert post-processing utility (Queiruga, 2018) is used in a standalone script for the Millstone simulator in this system.

A saturation dependent poroelastic constitutive response is used. The stress update is linear elastic with respect to the displacements, and the bulk and shear modulus depend on the hydrate saturation linearly by the relations $K(S)=K_0 S+K_1(1-S)$ and $G(S)=G_0 S+G_1(1-S)$ (Rutqvist and Moridis, 2009). The values K_0 and G_0 correspond to the hydrate-free moduli of the sediments, and K_1 and G_1 are calculated based on the *in situ* saturation and field-determined elastic moduli. Plastic yielding is not included in the stress integration, but the value of the Drucker-Prager yield criteria is calculated as an estimate of possible geoemechanical failure.

3.2. Domain dimensions and discretization

Very fine grids were used in the simulation of production from the vertical well in all cases of this study. The 2D cylindrical (axisymmetric) domains of the single vertical well problems in the four cases were discretized as follows:

- Case R (Reference, *r* = 2000 m): 452 x 525 in (*r,z*) = 2.37x10^5 gridblocks

- Case C1 (r = 500 m): 351 x 525 in (r,z) = 1.84×10^5 gridblocks
- Case C2 (r = 100 m): 239 x 525 in (r,z) = 1.25×10^5 gridblocks
- Case C3 (r = 75 m): 219 x 525 in (r,z) = 1.15×10^5 gridblocks

The meshes are aligned with the r-z axes. Drawing on past experience, the discretization along the z-axis within the 53.6 m of the HBS sequence had a maximum subdivision size Δz = 0.1 m, and ensured that each layer was subdivided in at least 3 segments regardless of the layer thickness (thus providing sufficient description of thermal gradients, and of heat and fluid flows). The same fine discretization along the z-axis was maintained in the first few subdivisions of the overburden and the underburden in contact with the HBS sequence (necessary to describe fluid and heat exchanges between the hydrate-bearing system and its boundaries during the endothermic dissociation process that feeds gas production). The discretization was non-uniform (with Δz increasing) in the mud of the overburden and underburden away from the top and bottom hydrate interfaces, i.e., near the top and bottom of the domain.

Particular emphasis was given to fine discretization in the first 50 m along the r-axis, with 0.1 m radial subdivisions to 5 m, then linearly increasing Δr to 0.5 m at 50 m. Discretization past that point in the x- and y-directions was non-uniform, increasing logarithmically using a starting value of Δr = 0.5 m to 2,000 m (452 elements total). Past experience has indicated that such fine discretizations are necessary when steep thermal and pressure gradients are involved (Moridis et al., 2007). This high degree of refinement provided the level of detail needed to capture important processes near the wellbore and in the entire hydrate-bearing zone, and especially in the thin interlayers that characterize the NGHP-02-09 systems.

Treating hydrate dissociation as an equilibrium reaction (Kowalsky and Moridis, 2007) and accounting for the effect of the salinity on hydrate dissociation, resulted in a system of about 9.48x10^5, 7.36x10^5, 5.0x10^5 and 4.6x10^5 equations for Cases R, C1, C2, and C3, respectively. The size of the problem precluded the use of desktop computational platforms (except for scoping calculations) and necessitated the use of the parallel version of T+H (pT+H) and high-performance computing resources. The full two-way coupling between flow and geomechanics was intractable as the coupled simulation requires a smaller timestep size and more iterations per timestep. The complexity of the geology of the system and of the coupled processes involved were so extreme that the flow simulations alone required between 900,000 to 2,000,000 timesteps (total) to cover the study periods of the various cases, and required hundreds of thousands of CPU-hours. The resources of LBNL Lawrencium cluster farm were used to perform the pT+H simulations in this paper using 256 to 1,024 cores per submission.

The dual-mesh algorithm enables a coarser mesh to be used for the geomechanical response, where Millstone automatically handles the interpolation between the structured finite difference grid and unstructured finite element mesh. The final geomechanical results were solved on an unstructured quadrilateral mesh with 48,954 nodes and 48,777 elements, resulting in a system of 97,908 equations for displacement updates and 195,108 additional stress degrees of freedom. The mesh was structured near the well in the hydrate bearing layer with square elements of side length of approximately 0.25 m to capture the fine scale deformation. The post-processing-based one-way coupling algorithm allowed the geomechanical results to be calculated in approximately ten minutes for each case, for which only considering the one-way effects allowed us to only use 20 intermediate snapshots to compute the quasi-static deformation path.

3.3. Baseline system properties and well description

Key baseline hydraulic and thermal properties of the various geological media in the various layers of the geologic model in Figure 5 were provided from studies conducted by other members of the NGHP-02 expedition and are listed in Table 1. The corresponding geomechanical properties are listed in Table 2. These values were used in the simulation of all four cases. In the absence of relevant information, the relative permeability and capillary pressure relationships and corresponding parameters were approximations based on similarly textured media or calculated from estimated effective permeabilities. Note the relatively low thermal conductivity values measured from samples from Site NGHP-02-09. A possible explanation for the low values was the “watery” texture of the samples, as indicated by their very high porosity. Reasonable specific heat values were used for all the geologic media because data from direct measurements were unavailable.

The same layer geometry is applied to the finite element mesh for the geomechanical properties. In this study, material is modeled using a rate-based formulation that does not consider plastic behavior. We considered two material groups: a sandy (hydrate-bearing or hydrate-free) medium, and a clay (mud) medium of the overburden, underburden and of the interlayers between the sandy HBS. The relevant geomechanical properties (Young’s modulus, Poisson’s ratio, and skeletal grain density for each medium) are listed in Table 2. We used values of the Young’s modulus that are linear functions (interpolations) of S_H in the hydrate-bearing media. Based on Rutqvist and Moridis (2009) and Rutqvist et al. (2009), a constant Poisson’s ratio was used, and the Biot coefficient was b = 0.99.

Based on earlier studies that confirmed the validity of the approach (Moridis and Reagan, 2007a,b; Liu et al., 2017), we approximated wellbore flow by Darcian flow through a pseudo-porous medium describing the interior of the well. This pseudo-medium had φ = 1, a very high $k = 5\text{x}10^{-9}$ m^2 (= 5,000 Darcies), a capillary pressure $P_c = 0$, a relative permeability that was a linear function of the phase saturations in the wellbore, and a low (but nonzero) irreducible gas saturation $S_{irG} = 0.005$ to allow for the emergence of a free gas phase in the well. While discretely treating the wellbore is required to solve the flow, the structure is neglected in the mechanical analysis and the coarser size of the mesh elements extends to the center axis of the domain, using only the mechanical properties of the sediments.

3.4. Initial and boundary conditions

We determined the initial conditions in the reservoir by following the initialization process described by Moridis and Reagan (2007a,b). Based on initial measurements at the site, the geothermal gradient at the site was dT/dz = 5.82 ^{o}C/100 meter with a seafloor temperature of T = 3.46 ^{o}C (later updated—see *Waite et al. this issue*). The uppermost and lowermost gridblock layers (i.e., at the top of the overburden at the ocean floor, and at the bottom of the simulated domain) were treated as constant-condition boundaries (maintaining constant *P* and *T*). Knowing that a) the pressure *P* = 25.45 MPa at the ocean floor and b) the pressure distribution with depth was hydrostatic (as is almost universally the case in hydrate accumulations), we determined the pressure P_T using the *P*, *T*- and salinity-adjusted water density. Then, using P_T and the boundary temperatures T_T and T_B, the hydrostatic gradient and representative thermal conductivity values, we determined the vertical *P*- and *T*-profiles in the domains by means of a 1-D column simulation.

The numerical representation of a constant bottomhole pressure P_w involves imposing a constant P_w at the topmost element of the well in the manner used to impose other constant-condition boundaries. In our study, the system behavior and performance was evaluated at a single value of P_w (= 3.0 MPa). Based on the results of the Moridis et al. (2014) study, this bottomhole pressure was the most desirable (although not necessarily practical or attainable under the conditions of the Site NGHP-02-09 deposit), and useful in providing the upper estimate of production. This P_w value is larger than the CH_4-hydrate quadruple point pressure P_Q = 2.56 MPa, eliminating the possibility of ice formation and the corresponding adverse effect on k_{eff}, flow and production.

The boundary conditions of the geomechanical system include an assumption of no-horizontal displacement at both sides along the *r*-axis, and a no-vertical displacement boundary at the bottom. The overburden pressure (at the top of the first HBL) is set at 27.70 MPa. The initial stress state of the geomechanical system is determined by solving for a set of discarded displacements that solve the static equilibrium of the domain given the mechanical loading conditions, the spatially-variably material properties, and the initial fluid pressures and saturations used for the flow simulation.

4. Results and Discussion

4.1. Production performance in the reference Case R

Figure 6 shows the expected evolution of the hydrate dissociation (overall rate of gas release into the reservoir from hydrate dissociation) rate Q_D and of the gas production rate at the well, Q_P, as a result of the depressurization caused by the operation of a single vertical well at the center of the cylindrical infinite-acting domain. Although Q_P rises very fast to a high level (exceeding 5 MMSCFD in less than a month), even a cursory inspection of Figure 6 reveals a problem: Q_D is substantially smaller than Q_P, throughout the period of the test, indicating that hydrate dissociation is not the dominant source of the produced gas in this timeframe. Hydrate deposits that are promising targets for production are characterized by Q_D exceeding Q_P early in the production period, and their desirability increases with an increasing gap between the two. In the absence of free gas zones in the system, the only possible alternative source of gas is exsolution of CH_4 dissolved in the aqueous phase of the deposit. Given the very small solubility of CH_4 in H_2O, this indicates that very large amounts of H_2O need to be produced to provide the significant level of Q_P estimated by the simulation, raising significant questions about the viability of such an endeavor. The semi-log plot in Figure 7 shows the same Q_D and Q_P results, but focused on the early-time behavior. It shows net hydrate formation (denoted by the negative Q_D values) in the reservoir for the first 20 days of production. This means that CH_4 dissolved in the aqueous phase forms hydrate on the way to the well at a rate that exceeds the hydrate dissociation at elsewhere in the reservoir. An even more worrisome feature in Figures 6 and 7 is the declining trend in Q_D as time advances: this is the opposite of what would be expected in a desirable production target and is an indication of ineffective depressurization.

Review of the composition of the produced fluids in Figure 8 provides further evidence of the problem with this production test: gas dissolved in the produced water amounts to almost 50% of the total methane produced at the well. This means a very large water production rate is needed to achieve the rate of methane production predicted by the simulation. The cumulative volumes of methane produced and hydrate-originating methane in the reservoir (V_D and V_P, respectively) in Figure 9 depict clearly the increasing discrepancy between hydrate dissociation and gas production at the well (with $V_D << V_P$). Further evidence of the challenges facing a long-term production test at Site NGHP-02-09 is provided by the free gas volume V_F in Figure 10, which reaches a plateau within 50 days from the onset of production, and actually appears to decline slowly after this time (hinting at the possibility of secondary hydrate formation capturing free gas within the reservoir). Hydrate deposits that are desirable production targets are characterized by an increasing V_F over time (at least until a large part of the resource is exhausted) that acts as the primary source of gas for production. The inability of V_F to increase with time (in addition to the low Q_D) is further evidence of ineffective depressurization.

The water production results (Q_W and M_W) in Figure 11 confirm these problems and indicate the significant technical and economic challenge of moving the very large and increasing volumes of H_2O that are necessary to maintain the depressurization needed to support the production rate Q_P, mainly through transport of aqueous CH_4 in the produced water. The high level of Q_W and its non-declining (actually increasing) value with time even after t > 180 days is an indication of continuous inflow of H_2O from the boundaries. The water-to-gas ratio (WGR), $R_{WG} = M_W/V_P$, and the salt mass fraction X_S in the produced water (Figure 12) confirm the earlier observations, deductions and conclusions. WGR appears practically constant over time at a very high level (about 170 kg of H_2O per standard m^3 of CH_4) that is economically unsustainable and technically challenging (although perhaps feasible). The high and persistent WGR level during the duration of the test period is an additional indication of continuous inflow of H_2O from the boundaries. The evolution of X_S over time provides further support to the initial Q_D behavior—its value exceeding the natural salinity of ocean water (0.035) is a clear evidence and confirmation of the net hydrate formation identified in Figure 7, as hydrate formation in saline water results in localized salinity increases as the hydrate crystal does not admit salt. The fact that X_S remains above the 0.035 level indicates a combination of limited hydrate dissociation, hydrate formation at other locations, and inflow of ocean water from the boundaries, all of which point toward ineffective depressurization.

4.2. Spatial distributions of important parameters in the reference Case R

The pressure distributions in Figure 13 provide direct evidence of the indications of ineffective depressurization surmised from the analysis of the figures in Section 4.1. Thus, there appears to be practically no change in the *P*-distribution past $t \geq 56$ days. Note the relatively thin depressurization zone, indicative of a higher effective permeability compared to its adjacent units. The depressurization band, however, does not expand beyond the range seen at $t = 17$ days, thus further supporting the conclusion of ineffective depressurization. As expected, the largest pressure drop in the domain (depicted by the yellow-blue range of color) occurs close to the vertical well at $r = 0$ and corresponds to hydrate dissociation there.

The *T*-distributions in Figure 14 are different in pattern than the *P*-distributions in Figure 13, but it is these differences that confirm the observations and conclusions drawn from the *P*-profile analysis and from the earlier results. At $t = 17$ days, there is a narrow band of lower temperature in the upper part of the HBS sequence (within layers 1 through 28 as shown on Figure 5), which indicates cooling caused by active hydrate dissociation. However, this temperature disturbance is attenuated at $t = 56$ days, and practically disappears after that time. This is an indication of water inflows from the infinite-acting radial boundaries, which counters the initial cooling and at the same time provides the pressure support observed in Figure 13. The limited dissociation discussed in Case R is further indicated by the absence of any noticeable change in the *T*-distributions for $t > 56$ days.

The evolution of the S_H and S_G distributions are shown in Figures 15 and 16, respectively. The hydrate saturation appears practically unchanged after $t \geq 56$ days, as does the distribution of gas, S_G. The limited occurrence of free gas (derived from dissociation) is consistent with the V_F results of Figure 10 and confirms both the observations of limited dissociation and its stagnation as time advances. In addition to poor dissociation performance, some localized formation of hydrate occurs in the uppermost layers, resulting in hydrate saturations that exceed the initial saturation (indicated by arrows in Figure 15). Further proof is provided by the X_S distribution in the aqueous phase that is shown in Figure 17: the absence of significant freshening of the water and the limited footprint of the areas where X_S is different from the background level are consistent with limited (or non-occurring) dissociation, and is in agreement with all previous observations.

Figure 18 describes the pressure profile inside the well (i.e., along z at r = 0) and provides clear evidence of the culprit for the ineffectiveness of depressurization and the consequent limited hydrate dissociation. Although there is no resistance to flow within the well casing (being in essence an “infinite permeability” system, leading to an expectation of a near-linear pressure decline in the well), there is no significant pressure drop at any time below about z = -241 m. The obvious inference is that there is a source of water at and above this level that can easily replenish the water produced by the well, thus preventing any pressure drop below this point. This source of water is the hydrate-free sandy layers Aqu01 through Aqu10 (see Figure 5), which have very high permeability (on the order of $k_r = 10^{-11}$ m^2 = 10 D, Yoneda et al. (this issue-b)), thus having enough capacity to resupply all the water withdrawn by the well and preventing a pressure drop below the z = -241 m (with Aqu10, at z = -248 m and with a thickness of nearly 7 m, capable of contributing significant flows) . In addition, the low-permeability layers Mud01 through Mud05 (-230 m < z < -226 m) separate the upper hydrate and aquifer layers and are reflected by the near step-change in pressure within the reservoir below -226 m seen in Figure 13. Consequently, effective depressurization is not possible below this level.

4.3. Conclusions drawn from the production performance in Case R

The results of the study indicate that gas production from Site NGHP-02-09 under the conditions of a long-term field test involving a single vertical well is technically feasible and can yield high gas production rates. However, the high gas production is based mainly on exsolution of dissolved gas rather than hydrate dissociation and thus necessitates excessively large water production, the management of which appears to be a technical challenge.

The conclusion from this analysis is that Site NGHP-02-09 is not a promising location for a field test of gas production from the hydrate deposits of the KG Basin. Despite encouraging conditions (high permeability and hydrate saturation) and ample hydrate resources at the site (with a combined thickness of HBLs in excess of 36 m and an excellent permeability regime of these units), the presence and attributes of the hydrate-free and extremely permeable aquifer layers are sufficient to singlehandedly short-circuit the depressurization process and preclude the consideration of Site NGHP-02-09 as a possible test location. In essence, such a test would be a demonstration of production more of exsolution of dissolved gas rather than of dissociation of hydrates. Note that attempts to isolate the Aqu10 layer by modifying the location of the perforated interval of the well (e.g., confining it to intervals above and below this layer) in several scoping simulations had no practical effect, with production behavior very similar to that of the fully perforated HBS sequence as there are still many sources of water inflow.

4.4. Production performance in Cases C1, C2 and C3

The importance of the assumed no-flow radial boundaries in Cases C1, C2 and C3 is amply demonstrated by the evolution of the corresponding gas release rates Q_D in Figure 19, which also includes the Q_D for Case R for comparison. The differences in both pattern and performance are notable. In all three cases, we observe an early surge of gas release at rates that are between 3 and 3.3 m^3/s (9 and 10 MMSCFD) and are caused by the large initial driving force of depressurization, i.e., the difference ΔP between the bottomhole and the reservoir pressure in the vicinity of the well that is at its maximum at the beginning of production. Because the Aqu10 unit is now unable to function as a practically infinite source of water, depressurization is effective and leads to the large initial Q_D that occurs almost immediately after the onset of production in the limited volumes of the domains in Cases C2 and C3. In this first gas release, Q_D is higher for the cases with reduced domain volumes because of stronger response to depressurization, although the lack of enhancement from Case C2 to C3 suggests there is a practical limit to tighter well spacing. The response in the larger-volume domain of Case C1 is slower because of the correspondingly larger mass of water in the Aqu10 unit. This is the reason why the Q_D for Cases R and C1 initially coincide, with the point of deviation at about t = 20 days marking the first effect of the closed boundaries.

The initial spike in Q_D is followed by longer periods of large Q_D that peak at similar levels of about 3 MMSCFD for Cases C2 and C3, but are larger (peaking at about 4 m^3/s or 12 MMSCFD by t = 300 d) in the larger system of Case C1. In this second gas release, Q_D increases with an increasing domain volume because of an increasing mass of dissociating hydrate. Although the driving force difference ΔP is smaller, the effect of dewatering of the system leads to an effective depressurization of the hydrate over a large volume of the reservoir, significant dissociation and gas release. The peak in this second phase of hydrate dissociation is followed by a continuous decline in Q_D that is attributed to the reduction in the reservoir temperature (caused by the endothermic nature of dissociation, which inhibits dissociation) and in the driving force of dissociation, i.e., the difference between wellbore and reservoir P). The same behavior is more evident in Cases C2 and C3.

The evolution of the gas production rate Q_P in cases C1, C2, and C3 (Figure 20) follows a similar pattern as Q_D, and differs substantially from that in Case R in terms of pattern, magnitude and relationship to Q_D. Q_P also exhibits the two-lobe pattern of Q_D in the C1, C2, and C3 cases (Figure 20), with similar relationships of the relative magnitudes between the cases. Thus, the first surge of production peaks at about Q_P = 4.5, 6, and 6.5 MMSCFD in Cases C1, C2, and C3, respectively. The second (long term) surge of production peaks at about Q_P = 8, 3.5, and 3 MMSCFD in Cases C1, C2, and C3, respectively. The effective hydrate dissociation in these closed systems is demonstrated in the analysis of the origin of gas in Cases C1 and C3 (Figure 21), which now shows a far smaller contribution to Q_P from methane dissolved in the produced water than in Case R. Both the Q_P and Q_D results are positive indicators of the potential of the site as a target for multi-well production rather than as a test site. Note that these enhancements assume a degree of uniformity across the larger multi-well reservoir system and that these results reflect the performance of *inner wells* shielded from water inflow by outer wells in the pattern. Interference between wells due to unknown pathways or heterogeneities in hydrate dissociation could reduce the effectiveness of a multi-well pattern.

The cumulative volumes of produced gas V_P in Figure 22 indicate (a) similar initial production in all closed-system cases, with deviations marking the beginning of exhaustion of the different hydrate masses (or severe reduction in dissociation) in the 3 systems, and (b) V_P that are consistently lower than that for Case R during the initial 200 days of the simulation. The evolution of free gas volume V_F in the three domains (Figure 23) also shows a striking difference from that in Case R and explains some of the V_P observations: V_F are now much larger by orders of magnitude, as released gas is stored in the reservoir, and is used as a source of gas for production. The severe reduction in hydrate dissociation (attributed to the causes discussed earlier) is evident in Cases 2 and 3, but has not yet begun during the production period in the larger system of Case 1. As expected, both V_P and V_F increase with an increased volume of the closed domain of the cases.

The evolution of water production (rates Q_W and cumulative mass M_W in Figures 24 and 25, respectively) shows the clear production superiority of closed systems compared to Case R. Following an initial surge of very short duration, Q_W decreases continuously in all three cases (in contrast to the increasing Q_W in Case R), leading to M_W that are much smaller than those in Case R and posing a much easier water management problem that becomes easier as the reservoir volume corresponding to each well in the closed systems decreases. Thus, the attractiveness of the larger V_P in Case R is negated by the much larger M_W, but Cases C1, C2, and C3 emerge as possible production options. This is further confirmed by the WGR in Figure 26, which indicates a generally improving gas vs. water regime in all three closed-system cases, and is consistent with promising production targets. Note the slight increase in the WGR for Cases 2 and 3 at late times, which is attributed to water inflows from the top (overburden and ocean floor) and bottom (deep subsurface) boundaries that are enhanced by the depressurized interior of the reservoir. This is confirmed by the pattern of X_S evolution in Figure 27, which exhibits the effect of active hydrate dissociation in the initial X_S decline (water *freshening*) that is caused by the release of salt free water from the hydrate dissociation. The X_S decline is faster where hydrate dissociation is at its most intense, i.e., it is enhanced in decreasing system volumes. However, in the smaller volumes of Cases 2 and 3, there is a pattern reversal and an increase in X_S for t > 300 days (when hydrate dissociation is at its minimum and the system pressure is at its lowest), which is an indication of saline water inflows, as well as of hydrate regeneration in the reservoir.

4.5. Spatial distributions of important parameters in the Cases C1, C2, and C3

In Case C1, the pressure distributions in Figure 28 clearly indicate a more effective depressurization than in Case R. The thin band identified in Figure 13 is clearly discernible initially, but the lack of inflows from the radial boundaries results in pressure drops over the entire reservoir depth interval that, as expected, continuously expand radially with time and are a positive indicator of production potential. The effective depressurization and its positive impact on hydrate dissociation in Case C1 is further demonstrated in the evolution of the T-distribution of Figure 29, which shows a continuous cooling of the system beyond the immediate wellbore and is another indicator of occurrence of the endothermic process of hydrate dissociation. Further confirmation of the enhanced hydrate dissociation in Case C1 (compared to that in Case R) is provided by the evolution of the S_H, S_G and X_S spatial distributions in Figures 30, 31 and 32, respectively. The footprint/occurrence of S_H indicates a continuously shrinking hydrate mass, which is by no means near exhaustion at the end of the 360-day production period. However, some localized hydrate reformation (indicated by arrows) still occurs, with local $S_H > S_{H,initial}$. This is accompanied by ever-expanding footprints of increasing S_G and decreasing X_S in the reservoir, as well as by increasing S_G and decreasing X_S levels, providing direct evidence of enhanced dissociation.

In Case C2, the system behavior is similar to that in Case C1, but far more intense. Thus, the pressure distributions in Figure 33 indicate a continuous and an even more effective depressurization, as depicted by larger pressure drops over a larger system volume. Similarly, the evolution of the T-distribution in Figure 34 shows a continuous and faster (than in case C1) cooling of the system that affects a larger portion of the system volume, and is an indicator of intense hydrate dissociation. Further confirmation of intense hydrate dissociation in Case C2 (compared to that in Cases R and C1) is provided by the evolution of the S_H, S_G, and X_S spatial distributions in Figures 35, 36 and 37, respectively. The footprint/occurrence of S_H indicates a continuously shrinking hydrate mass. However, given the production behavior discussed in the previous section, there is no indication of hydrate exhaustion (only of mass reduction) at the end of the 540-day production period. This explains the production behavior and eliminates the possibility of exhaustion of hydrate as a possible reason for the near-cessation of dissociation and the consequent severe reduction in production at later times.

This explanation can be further strengthened by an inspection of the spatial distributions in Figures 33 to 37, in addition to a re-evaluation of the production results. Once again, closer inspection of the S_H distribution at t = 540 days indicates localized increases in S_H (arrows). The S_G distribution indicates gas exhaustion, as indicated by the reduction in the S_G levels at t = 540 days, and is consistent with the V_F results in Figure 23. At the same time, the footprints of X_S in the reservoir, as well as the increasing X_S levels, providing direct evidence of continuing (albeit localized) dissociation. All these results taken together indicate that there is no hydrate exhaustion in Case C2, and the reason for the significant reduction in gas release and production is that (a) the driving force of dissociation, i.e., the ΔP between well and reservoir, is now at a minimum and (b) the system temperature has fallen so much that further hydrate dissociation is not only severely reduced, but can also lead to localized hydrate reformation. This can also partly explain the increase in the salinity of the produced water observed in Figure 27.

The evolutions over time in the spatial distributions of the same key parameters in Case C3 are very similar to those in Case C2, and will not be discussed in detail.

4.6. Conclusions drawn from the production performance in Cases C1, C2, and C3

The conclusion from the analysis of the closed systems in Cases C1 to C3 is that Site NGHP-02-09 may be a promising production target for full production operations despite its unsuitability as a location for a single vertical well test. However, this requires controlling the water inflows from the radial boundaries to increase the productivity of interior wells. For those interior wells of the multi-well pattern, depressurization can induce significant hydrate dissociation and gas production while water production can be manageable. The hydrate accumulations at this site seem to meet both an absolute criterion of high gas production and a relative criterion of manageable/low water production. Confounding costs and challenges include the need for installing lower-performing wells at the boundaries of the pattern that serve to control water influx at a single interior well. Larger arrays, though more expensive to construct, would offer more interior wells per exterior well.

5. Geomechanical system behavior

The geomechanical response was calculated for each of the cases discussed in the previous section using the one-way coupling process. The maximum strains found in the simulation domain for each of the cases is plotted in Figure 38. The evolution of the vertical displacements u_z along the z-axis (indicating uplift or subsidence) at the seafloor, top of the reservoir, and bottom of the reservoir are plotted in Figures 39. Snapshots of the displacement fields for each of the cases at three times are presented in Figures 40 to 42. The snapshots are zoomed in at the production zone clearly indicate increasing magnitudes as time advances, as well as a progressive contraction (“squeezing”) of the reservoir as the top subsides and the bottom is uplifted in response to depressurization. This is clearly demonstrated in Figure 39, which shows the evolution of the maximum and minimum u_z displacements in the vicinity of the vertical wells in cases R, C1 and C2. The displacements in Case R are minimal: practically zero at the ocean floor, a slight uplift at the base of the accumulation because of the effect of the Aqu10 layer that prevents depressurization, and a slight subsidence at the top of the accumulation in response to the proximity of the location of the maximum pressure drop near the top of the well operating at a constant P_w. This minimal impact allows for the de-coupling of the geomechanical and production flow simulations that allow for tractable production simulations to be accomplished given the requirement for exceedingly fine reservoir discretizations. We recognize that in many systems with other characteristics, most notably more aggressive hydrate dissociation, full two-way coupling will be required to achieve more reliable production simulations.

The displacements in the closed systems in cases C1 and C2 are far more substantial, and increase with a decreasing radius (and volume of the reservoir portion served by the individual wells). The depressurization of the system is primarily isolated to the reservoir layers, and consequently the reservoir sediments exhibit the most pronounced deformation. Because the overburden does not deform significantly, the subsidence at the ocean floor in these cases for the interior wells closely follows that at the top of the accumulation, and reaches about 4 m and almost 9 m at the end of their production periods in Cases C1 and C2, respectively, at which levels they appear to stabilize. The underburden is pulled up towards the well from the fixed based, so that the uplift at the base of the Case C1 reservoir is about 0.55 m, which, when combined with the subsidence at the top, indicated clear contraction “squeezing” of the reservoir at the well. These results indicate that production simulations for these alternative cases will be optimistic in comparison to fully-coupled simulations of these multi-well cases, should such simulations become practically possible in the future.

The u_z displacements at the base of the accumulation in Case 2 follow a different pattern. There is an initial uplift that reaches a maximum of about 0.55 m, but the severe and progressing depressurization in the case leads to a pattern reversal after about t = 30 days and a continuous decline in the uplift, ending in subsidence that begins at about t = 270 days and reaches very modest levels (0.2 m) at the end of the 540-production period. The displacement behavior in Cases C1 and C2 may have important implications for the construction, completion and stability of the well, and may impose specific material requirements in order to meet the mechanical challenges posed by such behavior. Obviously, the situation can change significantly if production from Cases C1 and C2 ceases earlier than the production period of this study, and this is entirely possible because of the low (and declining, and eventually uneconomical) Q_P level after a certain point (see Figure 20).

Plasticity was not incorporated in the one-way calculations of the geomechanical response, but the important stress factors were post-processed to estimate regions of possible failure. In Figures 43 to 45, the value of the Drucker-Prager yield criterion, a smooth version of the Mohr-Coulomb yield criterion, is plotted in the reservoir case for each region. Yield would be indicated by a criterion that is less than zero, where zero is the yield surface itself. We do not use a hydrate-dependent yield criterion and use only the cohesion of the hydrate-less sediment everywhere to serve as a lower bound for the estimates. Because of ineffective depressurization in Case R, the stresses are limited.

This not the case in cases C1 and C2, which show increasing stress as depressurization becomes more effective with a decreasing volume of the domain under investigation. In case C2 with the most extreme depressurization, the hydrate-less sediments deform significantly, with one region indicated yielding in the second layer from the top, marked by a red circle in Figure 45. This is clearly demonstrated in Figure 38, which shows the evolution of the maximum and minimum ε_{zz} and ε_{rr} strains (over the reservoir volumes) over time. The strains are minimal in Case R, but can be significant (and possibly severe) in Case C2 where maximum depressurization and hydrate dissociation occurs.

The conclusion drawn from these results is that full-field production from the hydrate accumulations at Site NGHP-02-09 site needs to carefully consider geomechanical issues that can be challenging. The authors of this study are unable to authoritatively proffer an opinion on whether the geomechanical criterion of the reservoir desirability as a production target can be met because of lack of the required well construction expertise to address the issue, and because other issues (e.g., when production should cease, decision that can be driven by both Q_P and economic considerations) can affect the maximum displacements experienced during production. As noted, to render these simulations tractable, progressive compaction in the reservoir, and the implied decrease in permeability, were not incorporated into the estimates of gas and water flow rates. Thus, the overall production values estimated in this study should be a first order review of a highly complex system.

6. Overall conclusions

The following conclusions can be drawn from this study:

- Gas production from Site NGHP-02-09 under the conditions of a long-term field test involving a single vertical well is *technically feasible* and can yield high gas production rates. However, the high gas production is based mainly on exsolution of dissolved gas rather than hydrate dissociation and is thus burdened by an excessively large water production.
- Given the properties and the geological model used in this study, Site NGHP-02-09 does not appear to be a promising location for a field test of gas production from the hydrate deposits of the KG Basin because of the presence and attributes of the hydrate-free and extremely permeable Aqu10 layer short-circuit the depressurization process.
- Site NGHP-02-09 may be a more promising production target for a multi-well operation despite its unsuitability as a single-well test location because the control of the water inflows by the multi-well system promotes more effective depressurization while keeping the water production within manageable limits. These results suggest merit in further evaluation of economics of full-field production of this reservoir. Such evaluation will need also to incorporate the potentially significant geomechanical effects on production for the system.
- The geomechanical issues associated with production from the hydrate accumulations at Site NGHP-02-09 need to be carefully considered as significant displacements are possible, which can be challenging to well construction and

stability. Note that other considerations (such as the point at which cessation of production should occur, as dictated by economic and/or technical reasons) can change significantly the severity of the geomechanical challenges.

Acknowledgment

The authors are thankful to the Ministry of Petroleum & Natural Gas within the Government of India, Oil and Natural Gas Corporation Limited (ONGC), Directorate General of Hydrocarbons (DGH), Oil India Ltd, GAIL (India) Ltd, Indian Oil Corporation Ltd and all other NGHP partner organizations for providing the opportunity to contribute to the NGHP-02 Expedition and this special issue of the Journal of Marine and Petroleum Geology. The technical and science support from Japan Agency for Marine-Earth Science and Technology (JAMSTEC), United States Geological Survey (USGS), U.S. Department of Energy (US-DOE), Japan's National Institute of Advanced Industrial Science and Technology (AIST), Geotek Coring, and Schlumberger is gratefully acknowledged. This work was supported by the Assistant Secretary for Fossil Energy, Office of Natural Gas and Petroleum Technology, through the National Energy Technology Laboratory, under the U.S. Department of Energy, Contract No. DE-AC02-05CH11231.

References

Boswell, R., Yoneda, J., Waite, W., this issue-a: India National Gas Hydrate Program Expedition 02 summary of scientific results: Evaluation of natural gas hydrate-bearing pressure cores.

Boswell, R., Myshakin, E., Moridis, G., Konno, Y., Collett, T., Reagan, M., Ajayi, T., Seol, Y., this issue-b: India National Gas Hydrate Program Expedition 02 summary of scientific results: Numerical simulation of reservoir response to depressurization.

Collett, T., et al., this issue, India National Gas Hydrate Program Expedition 02 – scientific results.

Kowalsky, M. B., and G.J. Moridis, 2007. Comparison of kinetic and equilibrium reactions in simulating the behavior of gas hydrates, *Energy Conversion and Management*, **48**, 1850, doi:10.1016/j.enconman.2007.01.017.

Kumar, P., et al., this issue, India National Gas Hydrate Program Expedition 02 – operational and technical summary.

Li, G., G.J. Moridis, K. Zhang and X.-S. Li, Evaluation of Gas Production Potential from Marine Gas Hydrate Deposits in Shenhu Area of the South China Sea, *Energy & Fuels*, **24**, 6018-6033, 2010 (doi: 10.1021/ef100930m).

Liu, N., Pan, L., Cheng, J., 2017. Numerical Modeling of CO2 and Brine Leakage through Open Fracture in a Fault Zone: Open Channel Flow or Darcy Flow**,** *Geofluids*, 2017, https://doi.org/10.1155/2017/9035032.

Marın-Moreno, H., T. A. Minshull, G. K. Westbrook, and B. Sinha 2015, Estimates of future warming-induced methane emissions from hydrate offshore west svalbard for a range of climate models, Geochemistry, Geophysics, Geosystems, 16(5), 1307–1323.

Moridis, G.J. and E.D. Sloan, 2007. Gas Production Potential of Disperse Low-Saturation Hydrate Accumulations in Oceanic Sediments, *J. of Energy Conversion and Management*, **48(**6)**,** 1834-1849, doi: 10.1016/j.enconman.2007.01.23.

Moridis, G.J., Kowalsky, M.B., Pruess, K., 2007. Depressurization-induced gas production from Class 1 hydrate deposits. *SPE Res. Eval. Eng*. **10** (5): 458-481.

Moridis, G.J., and Reagan, M.T., 2007a. Strategies for Gas Production From Oceanic Class 3 Hydrate Accumulations, *OTC-18865*, 2007 Offshore Technology Conference, Houston, Texas, 30 April – 3 May 2007.

Moridis, G.J., and Reagan, M.T., 2007b. Gas Production From Oceanic Class 2 Hydrate Accumulations, *OTC 18866*, 2007 Offshore Technology Conference, Houston, Texas, U.S.A., 30 April–3 May 2007.

Moridis, G.J., Kowalsky, M.B., and Pruess, K., 2008. TOUGH+HYDRATE v1.0 User's Manual: A Code for the Simulation of System Behavior in Hydrate-Bearing Geologic Media, Report LBNL-00149E, Lawrence Berkeley National Laboratory, Berkeley, CA.

Moridis, G.J., M.T. Reagan, S.-J. Kim, Y. Seol and K. Zhang, 2009a. Evaluation of the Gas Production Potential of Marine Hydrate Deposits in the Ulleung Basin of the Korean East Sea, *SPE Journal*, **14**(4): 759-781, doi: 10.2118/110859-PA.

Moridis, G.J., T.S. Collett, R. Boswell, M. Kurihara, M.T. Reagan, E.D. Sloan and C. Koh. Toward production from gas hydrates: assessment of resources and technology and the role of numerical simulation, *SPE Reservoir Evaluation & Engineering*, **12**(5): 745-771, 2009b (doi: 10.2118/114163-PA).

Moridis, G.J., and M.T. Reagan, 2011a. Estimating the Upper Limit of Gas Production From Class 2 Hydrate Accumulations in the Permafrost, 1: Concepts, System Description and the Production Base Case, *J. Petr. Sci. Eng.*, 76, 194-201, (doi:10.1016/ j.petrol.2010.11.023).

Moridis, G.J., and M.T. Reagan, 2011b. Estimating the Upper Limit of Gas Production From Class 2 Hydrate Accumulations in the Permafrost, 2: Alternative Well Designs and Sensitivity Analysis, *J. Petr. Sci. Eng.*, 76, 124-137, 2011b (doi: 10.1016/j.petrol. 2010.12.001).

Moridis, G.J., Silpngarmlert, S., Reagan, M.T., Collett, T., Zhang, K., 2011c. Gas production from a cold, stratigraphically bounded hydrate deposit at the Mount Elbert site, North Slope, Alaska. *J. Marine Petr. Geol*., **28**, 517-534 (doi: 10.1016/j.marpetgeo.2010.01.005)

Moridis, G.J., M.T. Reagan, K.L. Boyle, and K. Zhang, 2011d. Evaluation of the Gas Production Potential of Challenging Hydrate Deposits, *Transport in Porous Media*, **90**, 269-299 (doi: 10.1007/s11242-011-9762-5).

Moridis, G.J. and Pruess, K. 2014. User’s manual of theTOUGH+ Core code v1.5:A general-purpose simulator of non-isothermal flow and transport through porous and fractured media, LBNL Report 6871E, *https://pubarchive.lbl.gov/islandora/object/ir%3A1005566.*

Moridis, G.J. 2014. User’s manual for the HYDRATE v1.5 option of TOUGH+ v1.5:A code for the simulation of system behavior in hydrate- bearing geologic media, LBNL Report 6869E, *https://pubarchive.lbl.gov/islandora/object/ir%3A1005569.*

Moridis, G.J., A.F. Queiruga and M.T. Reagan, The T+H+M Code for the Analysis of Coupled Flow, Thermal, Chemical and Geomechanical Processes in Hydrate-Bearing Geologic Media, Paper 1195, Proceedings of the 9th International Conference on Gas Hydrates, Denver, Colorado, 25-30 June 2017.

Pruess, K., Oldenburg, C.M., Moridis, G.J., 1999. TOUGH2 Users Guide, Version 2.0, LBNL Report 43134, *http://tough.lbl.gov/assets/docs/TOUGH2_V2_Users_Guide.pdf.*

Pruess, K., 2003. The TOUGH Codes – A Family of Simulation Tools for Multiphase Flow and Transport Processes in Permeable Media, LBNL Report 53630, *https://pubarchive.lbl.gov/islandora/object/ir%3A121930.*

Queiruga, A.F. and M.T. Reagan. (2018, February 2). tough_convert: Version 1.0. Zenodo. http://doi.org/10.5281/zenodo.1164418

Rutqvist J. and G.J. Moridis, 2009. Numerical studies on the geomechanical stability of hydrate-bearing sediments, *Soc. Pet. Eng. J.*, **14**(2), 267–282 (doi: 10.2118/126129-PA).

Rutqvist J., Moridis G.J. and T. Grover, 2009. Geomechanical response of permafrost-associated hydrate deposits to depressurization-induced gas production, *J. Pet. Sci. Eng.*, **67**, 1-12.

Shukla, K.M., et al., this issue, Gas hydrate reservoir identification, characterization and delineation in Krishna-Godavari Basin using surface and subsurface data from Expedition NGHP-02, offshore India.

Stranne, C., O’Regan, M., Jakobsson M., 2016, Overestimating climate warming-induced methane gas escape from the seafloor by neglecting multiphase flow dynamics, *Geophys. Res. Lett.*, 43, doi:10.1002/ 2016GL070049.

Thatcher, K.E., Westbrook, G.K., Sarkar, S., Minshull, T.A., 2013, Methane release from warming-induced hydrate dissociation in the West Svalbard continental margin: Timing, rates, and geological controls, *J. Geophys. Res. Solid Earth*, 118(1), 22-38.

Waite, W., Jang, J., Collett, T., Kumar, P., this issue, Downhole physical property-based description of gas hydrate petroleum system in NGHP-02 Area C: a channel, levee, fan complex in the Krishna-Godavari basin offshore eastern India.

Yoneda, J., Oshima, M., Kida, M., Kato, A., Konno, Y., Jin, Y., Jang, J., Waite, W., Kumar, P., Tenma, N., this issue-a, Pressure-core based onshore laboratory analysis on mechanical properties of hydrate-bearing sediments recovered during India's National Gas Hydrate Program Expedition (NGHP) 02.

Yoneda, J., Oshima, M., Kida, M., Kato, A., Konno, Y., Jin, Y., Kumar, P., Tenma, N., this issue-b, Permeability variation and anisotropy of gas hydrate-bearing pressure-core sediments recovered from the Krishna-Godavari basin, offshore India.

Zhang, K., and Moridis, G.J., 2008. A Domain Decomposition Approach for Large-Scale Simulations of Coupled Processes in Hydrate-Bearing Geologic Media, paper presented at the 6th International Conference on Gas Hydrates, Vancouver, British Columbia, Canada, July 6-10, 2008.

Table 1. Reservoir Conditions and Porous Media Properties in the Site NGHP-02-9 Study

Hydrate dissociation model	Equilibrium
Overburden thickness	214.9 m
Underburden thickness	331.5 m
Initial pressure at top of domain/seafloor (P_T)	25.45 MPa
Pressure distribution with depth	Hydrostatic

Initial temperature at top of domain/seafloor (T_T)	3.46 ºC
Initial temperature at base of domain (T_B)	38.4 ºC
Temperature distribution with depth	Geothermal gradient (as affected by $k_{\Theta C}$)
Gas composition	100% CH_4
Water salinity	3.5%
Hydrate saturation in hydrate-bearing sands (HBS) S_H	0.75
Porosity (all formations) ϕ	0.45
Intrinsic permeability of the HBS layers k_r	10^{-11} m^2 (= 10.0 D)
Initial effective permeability of the HBS layers $k_{r,eff}$	10^{-15} m^2 (= 1 mD)
Intrinsic permeability of the other sand layers k_r	10^{-11} m^2 (= 10.0 D)
Intrinsic permeability of the mud layers k_r	10^{-17} m^2 (= 0.01 mD)
Intrinsic permeability of overburden/underburden k_r	10^{-17} m^2 (= 0.01 mD)
k_r/k_v	1 (all media)
Pore compressibility of sand layers	1.3×10^{-8} Pa^{-1}
Pore compressibility of mud layers	8.3×10^{-8} Pa^{-1}
Grain density ρ_R	2750 kg/m^3 (overburden) 2700 kg/m^3 (all other formations)
Media specific heat (C_R)	1000 J/kg/K (all formations)
Wet thermal conductivity ($k_{\Theta RW}$)	1.76 W/m/K (all formations)
Dry thermal conductivity ($k_{\Theta RD}$)	0.3 W/m/K (all formations)
Composite (water, hydrate, ice, rock) thermal conductivity model (Moridis et al., 2014)	$k_{\Theta C} = k_{\Theta RD} + (S_A^{1/2} + S_H^{1/2})\,(k_{\Theta RW} - k_{\Theta RD}) + \phi\, S_I\, k_{\Theta I}$
Capillary pressure model (van Genuchten, 1980)	$P_{cap} = -P_0 \left[\left(S^* \right)^{-1/\lambda} - 1 \right]^{-\lambda}$ $S^* = \dfrac{(S_A - S_{irA})}{(S_{mxA} - S_{irA})}$
λ	0.45 (sand); 0.25 (clay/mud)
P_0	10^4 Pa (sand); 10^6 Pa (clay/mud)
Relative permeability model (Moridis et al., 2014)	$k_{rA} = (S_A^*)^n$ $k_{rG} = (S_G^*)^m$ $S_A^* = (S_A - S_{irA})/(1 - S_{irA})$ $S_G^* = (S_G - S_{irG})/(1 - S_{irA})$
n; m	3.855; 2.5 (sand) 3.5; 2.5 (clay/mud)
Irreducible gas saturation S_{irG}	0.01 (sand); 0.03 (clay/mud)
Irreducible water saturation S_{irA}	0.10 (sand); 0.90 (clay/mud)
Constant bottomhole pressure BHP (P_w)	3.0 MPa

Table 2. Material Geomechanical Properties in the Site NGHP-02-9 Study						
Layers	**Young's modulus**	**Skeletal density**	**Poisson ratio**	**Shear modulus**	**Cohesion**	**Friction Angle**
Mud zones: Overburden	E=109 MPa	2750 kg/m^3	0.30	6 MPa	0.5 MPa	30°
Sand zones	E=50 MPa (at S_H=0) E=199 MPa (at S_H=1)	2700 kg/m^3	0.40	16 MPa	0.5 MPa	30°
Underburden	E=109 MPa	2700 kg/m^3	0.30	8 MPa	0.5 MPa	30°
Interlayer mud zones	E=109 MPa	2700 kg/m^3	0.30	7 MPa	0.5 MPa	30°

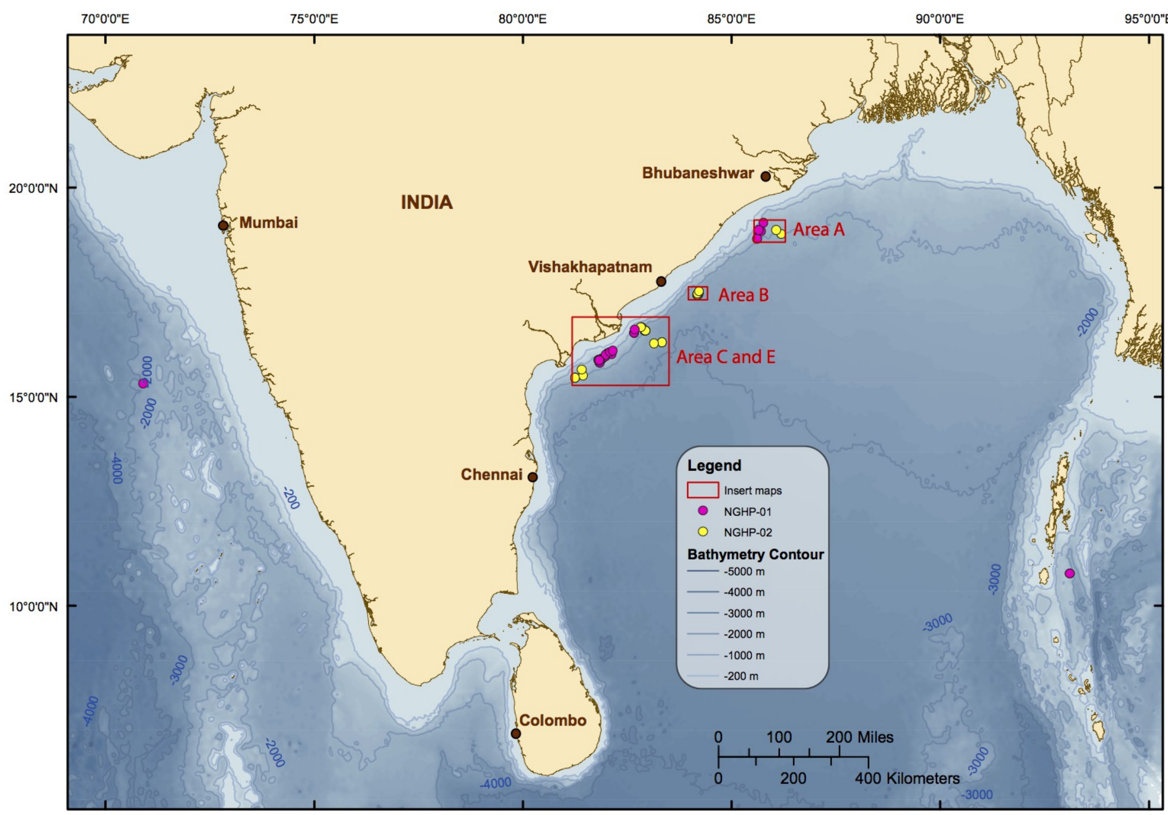

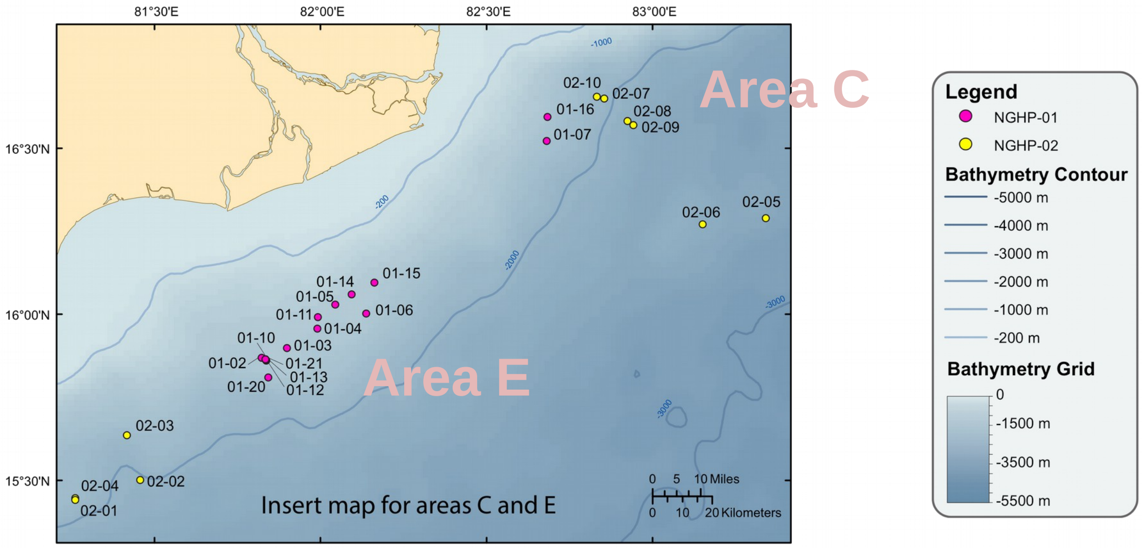

Figure 1. Physiographic map of the Krishna-Godavari (KG) Basin, areas of investigation during the NGHP-02 scientific cruise, and location of Site NGHP-02-09 (NGHP-02 Expedition Scientific Party).

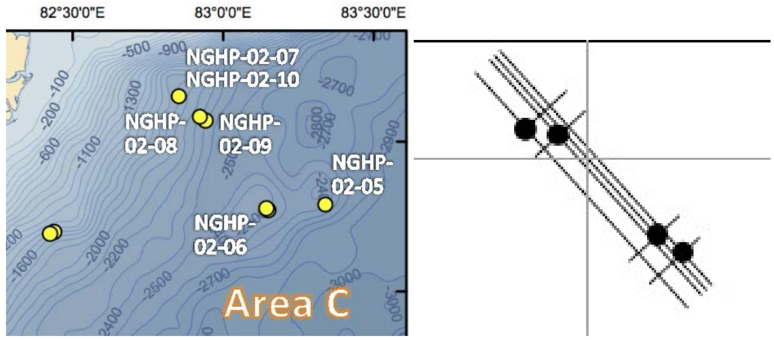

Seismic profile showing slope sediment with channel-levee system in Area C, NGHP Expedition 02.

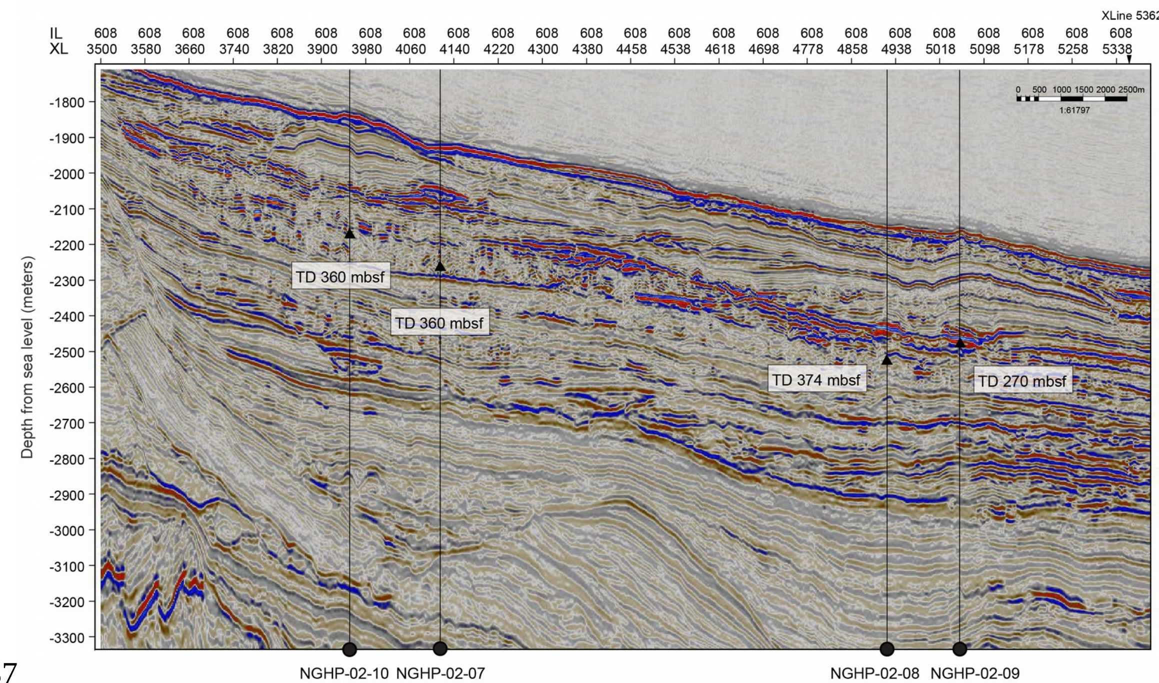

Figure 2 – The gas hydrate petroleum system in the KG Basin, seismic profile showing the slope-rise channel-levee system in Area C. Sites NGHP-02-08 and -09 penetrate levee deposits on either side of the channel near the toe of the continental slope (Collett et al., this issue).

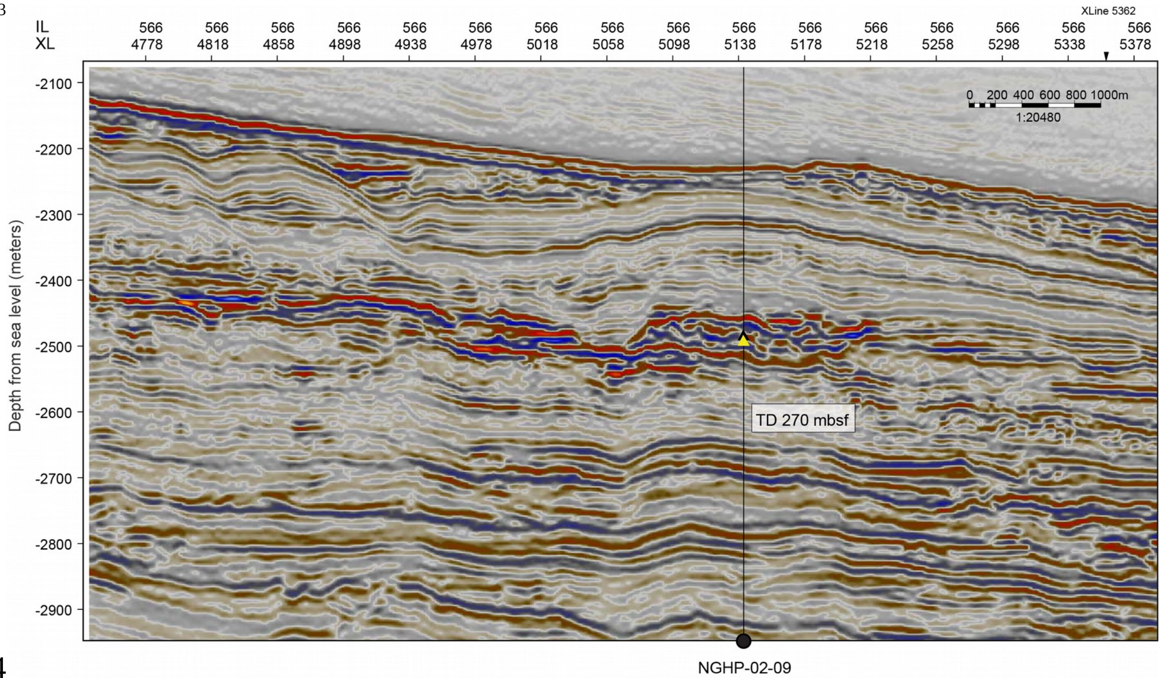

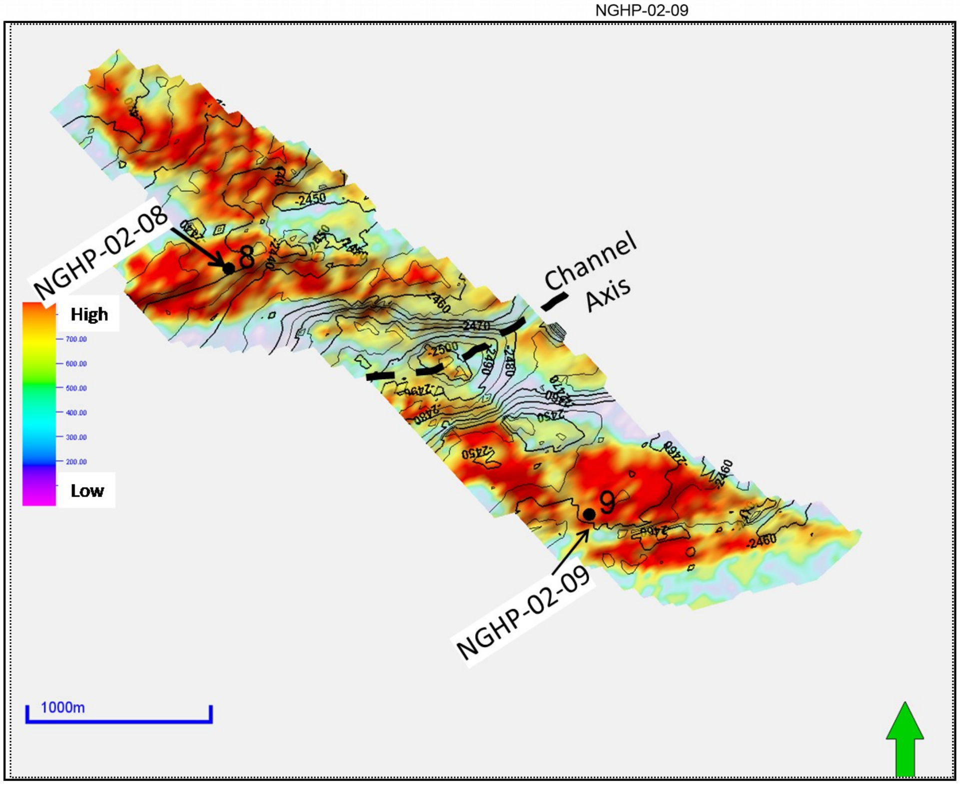

Figure 3. (a) Seismic profile through Site NGHP-02-09 (Collett et al., this issue), showing an image of the slope-rise channel-levee system in Area C.(b) Seismic amplitude distribution at 40 ms (TWT) close to the top of the gas hydrate reservoir at Sites NGHP-02-08 and NGHP-02-09 in Area C (Shukla et al., this issue).

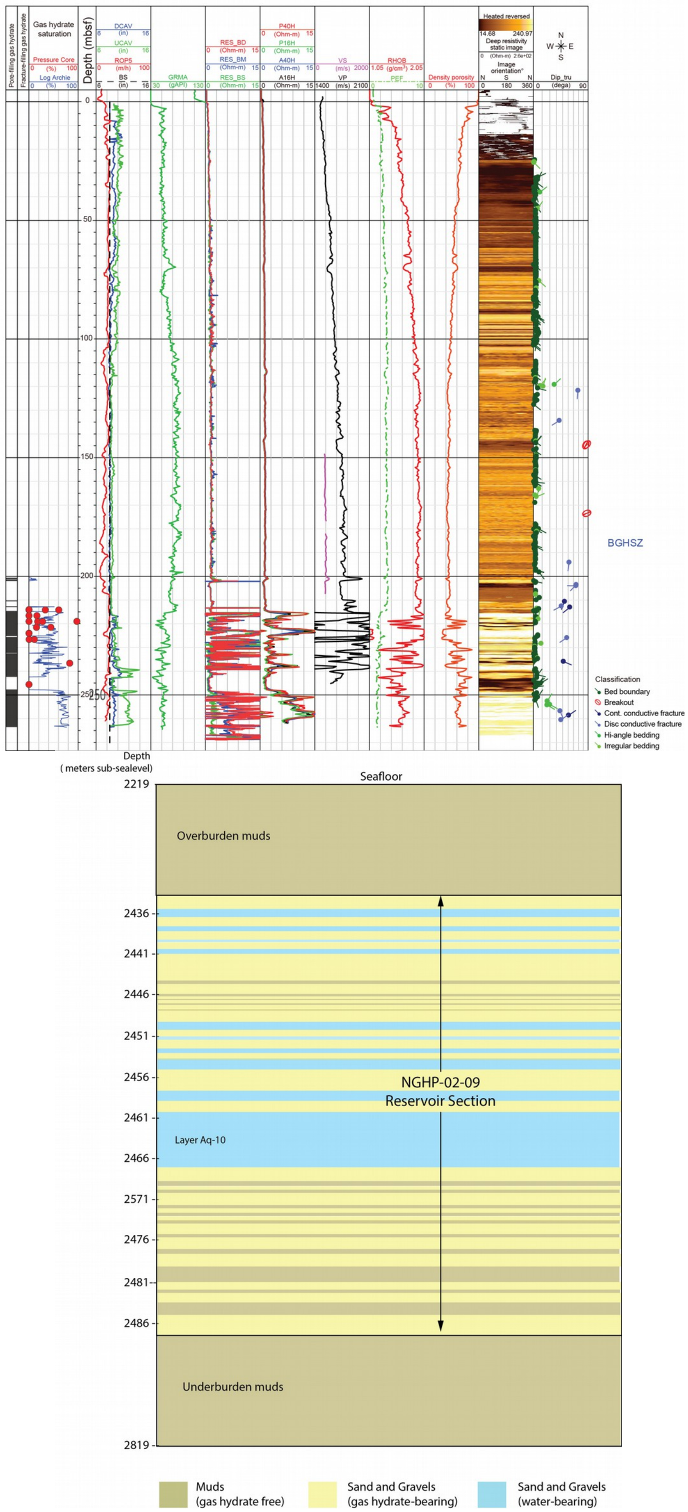

Figure 4. (a) Composite LWD log data display for Hole NGHP-02-09-A. BS =bit size, ROP5 =rate of penetration averaged over the last 5 ft, UCAV = ultrasonic caliper, DCAV = density caliper, GRMA = natural gamma radiation, RES_BD = deep button resistivity, RES_BS = shallow button resistivity, RES_BM = medium button resistivity, P40H/P16H = phase-shift resistivity, A40H/A16H = attenuation resistivity, VS = shear velocity, VP = compressional velocity, PEF = photoelectric factor, RHOB = bulk density (Collett et al.,

this issue). (b) Interpreted layered reservoir geology at Site NGHP-02-09 (Area C) in the KG Basin (Collett et al., this issue).

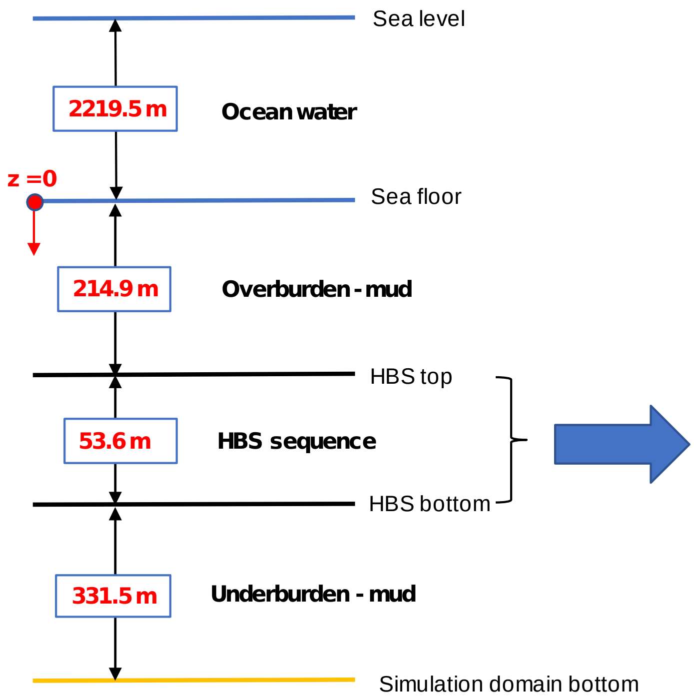

Layer #	Layer Name	Δ z (m)	Z_b (m)
1	Hyd01	1.8	-216.7
2	Aqu01	0.8	-217.5
3	Hyd02	1.3	-218.8
4	Aqu02	0.5	-219.3
5	Hyd03	1.1	-220.4
6	Aqu03	0.2	-220.6
7	Hyd04	0.8	-221.4
8	Aqu04	0.6	-222.0
9	Hyd05	3.3	-225.3
10	Mud01	0.5	-225.8
11	Hyd06	1.3	-227.1
12	Mud02	0.4	-227.5
13	Hyd07	0.3	-227.8
14	Mud03	0.2	-228.0
15	Hyd08	0.4	-228.4
16	Mud04	0.2	-228.6
17	Hyd09	0.5	-229.1
18	Mud05	0.2	-229.3
19	Hyd10	1.3	-230.6
20	Aqu05	1.1	-231.7
21	Hyd11	0.8	-232.5
22	Aqu06	0.3	-232.8
23	Hyd12	1.1	-233.9
24	Aqu07	0.4	-234.3
25	Hyd13	0.7	-235.0
26	Aqu08	1.3	-236.3
27	Hyd14	2.6	-238.9
28	Aqu09	1.2	-240.1
28	Hyd15	1.3	-241.4
30	Aqu10	6.9	-248.3
31	Hyd16	1.7	-250.0
32	Mud06	0.6	250.6
33	Hyd17	2.3	-252.9
34	Mud07	0.4	-253.3
35	Hyd18	0.5	-253.8
36	Mud08	0.4	-254.2
37	Hyd19	0.5	-254.7
38	Mud09	0.4	-255.1
39	Hyd20	1.2	-256.3
40	Mud10	0.4	-256.7
41	Hyd21	1.4	-258.1
42	Mud11	0.6	-258.7
43	Hyd22	1.5	-260.2
44	Mud12	2.0	-262.2
45	Hyd23	0.8	-263.0
46	Mud13	0.4	-263.4
47	Hyd24	1.2	-264.6
48	Mud14	1.4	-266.0
49	Hyd25	2.5	-268.5

Figure 5. A simple representation (not to scale) of the geology, stratification, texture and dimensions in the subsurface at at Site NGHP-02-09 of the KG Basin, as used in the description of the simulation domain. The "Hyd", "Aqu" and "Mud" prefixes in the layer description indicate hydrate-bearing sand, hydrate-free sand and mud, respectively. The origin of the z-axis used in the simulation grid coordinates is also clearly shown.

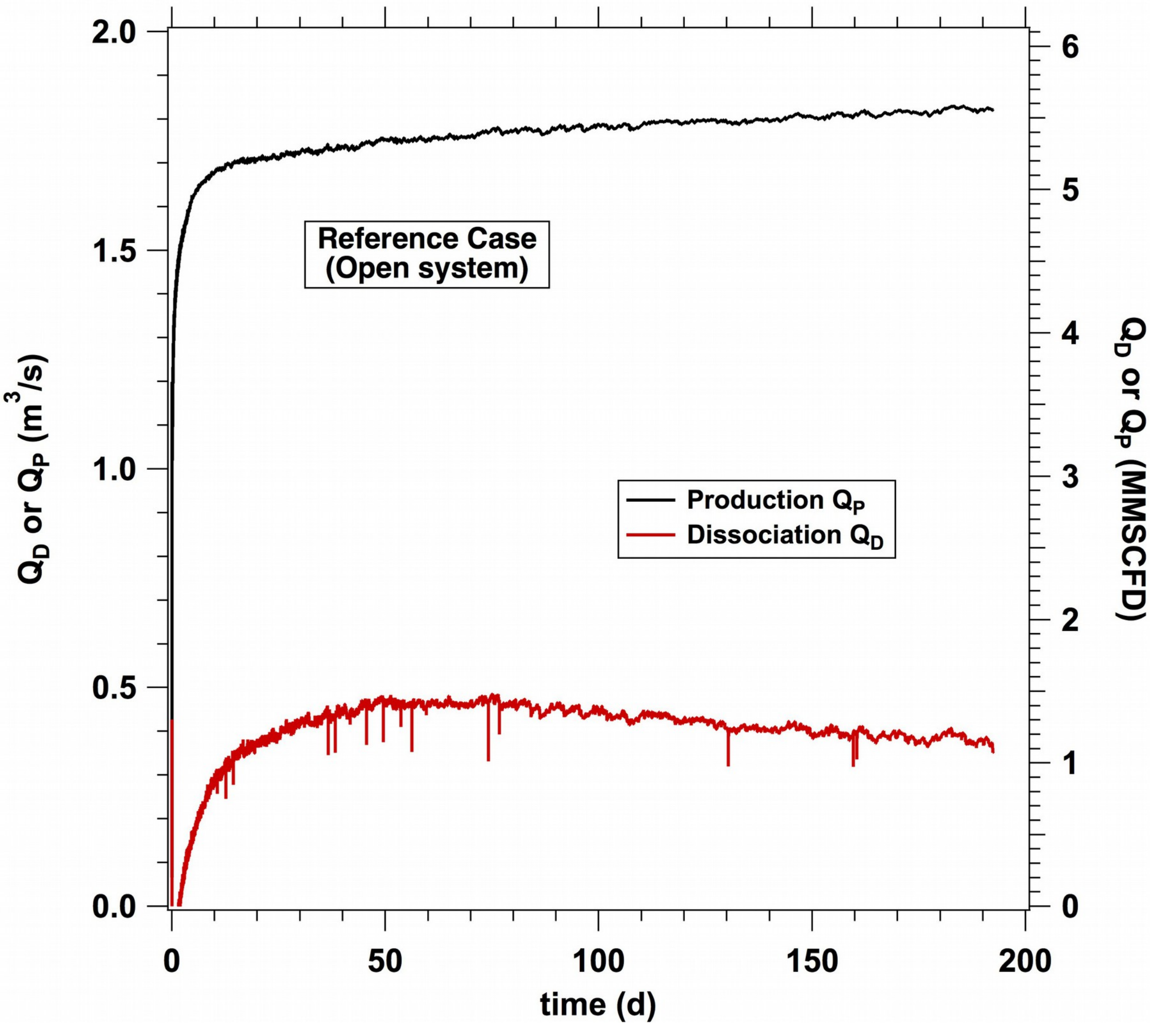

Figure 6. Reference Case R (open system, infinite-acting boundaries): expected evolution of the rate of gas release from dissociation (Q_D) and the rate of gas production (Q_P) over time during the planned long-term field test at Site NGHP-02-09 of the KG Basin. Note that Q_D is consistently (and substantially) lower than Q_P.

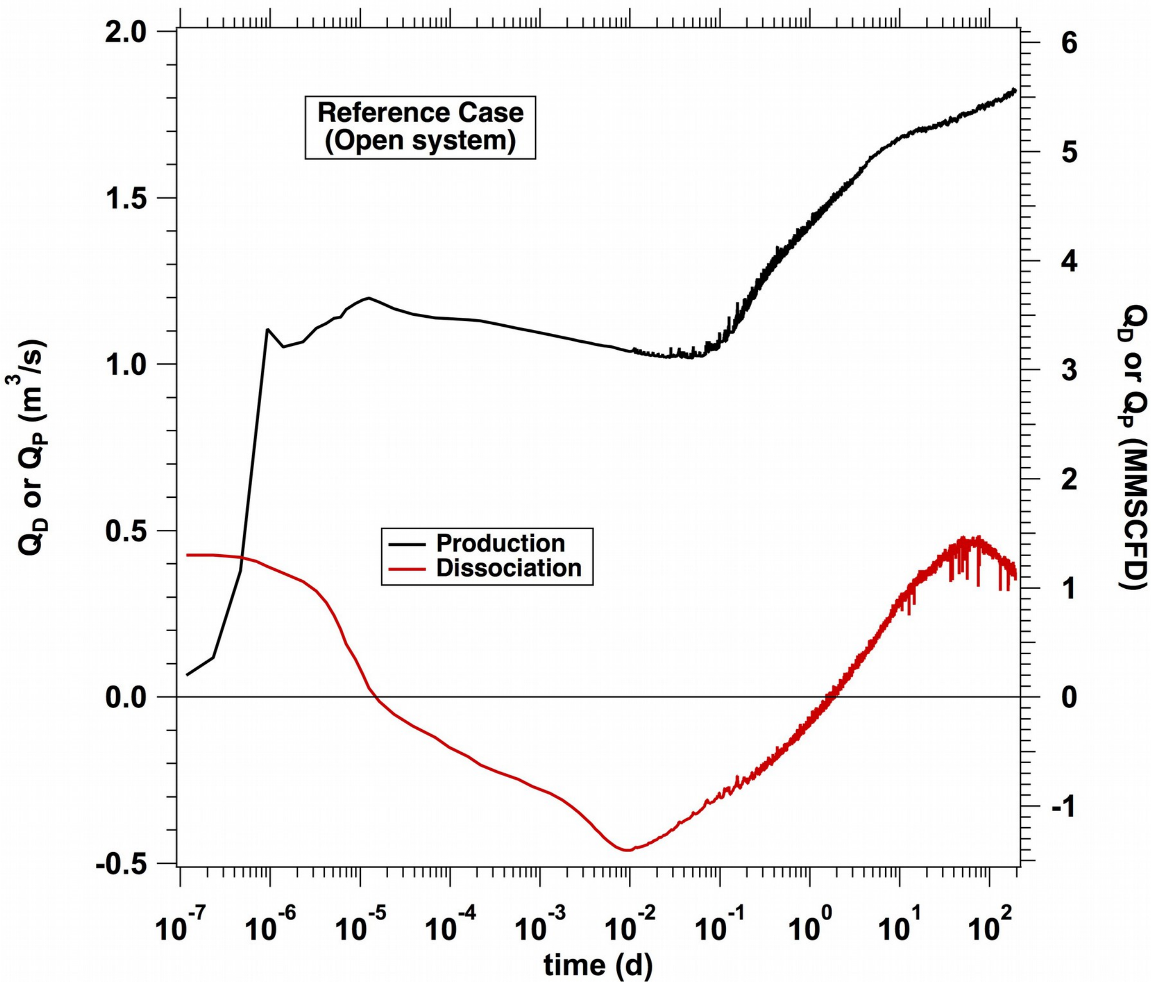

Figure 7. Semi-log plot of the expected evolution of Q_D and Q_P of the reference Case R (shown in **Fig. 6**) that captures the early time behavior of the system. The negative Q_P immediately after the initiation of production is attributed to secondary hydrate formation involving gas released from exsolution in the water.

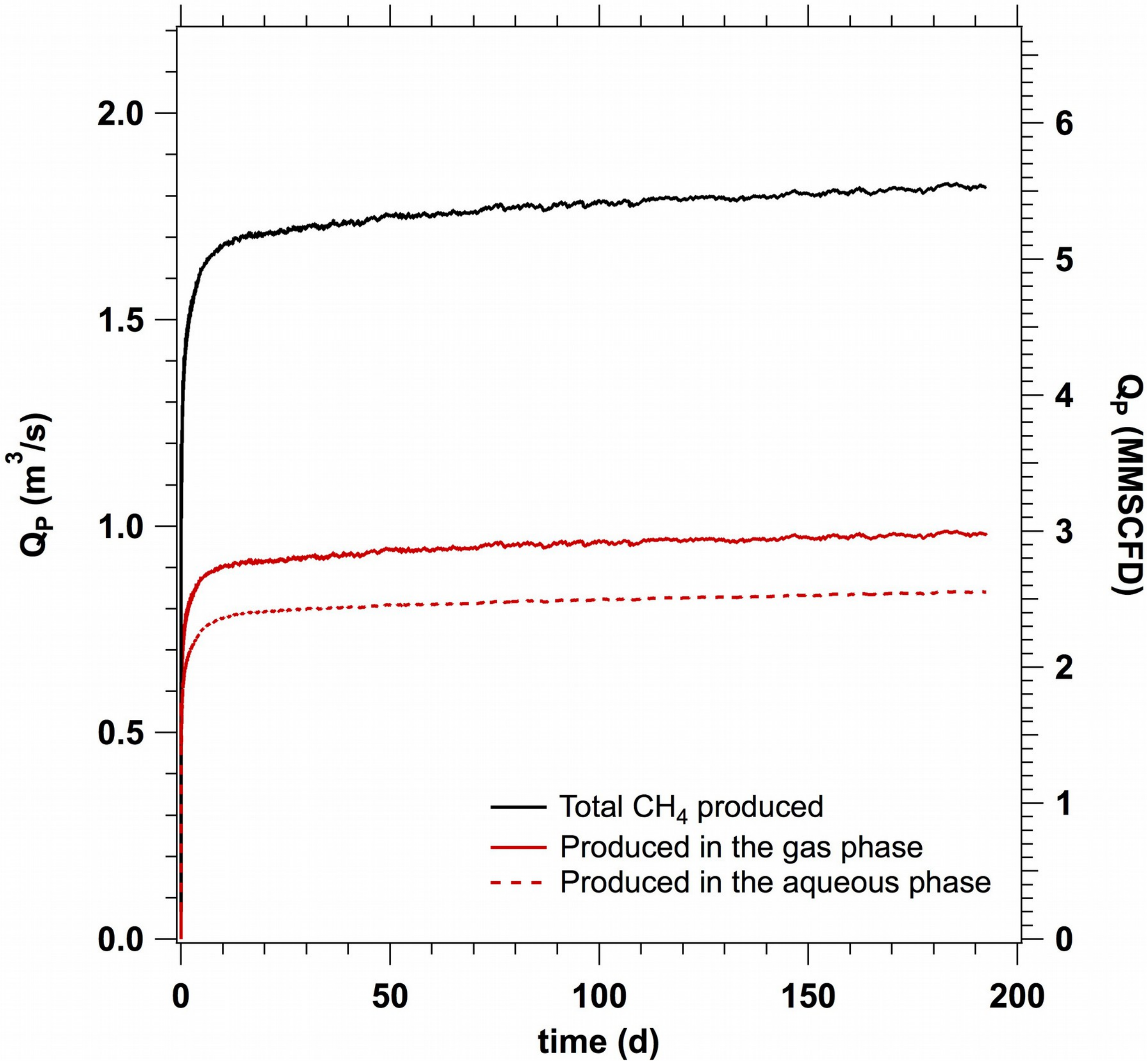

Figure 8. Provenance of gas in the produced fluids for Case R. **E**xsolution of dissolved gas from the produced water provides almost as much gas as as derived from hydrate dissociation to the total produced methane, Q_P, seen in Figure 6.

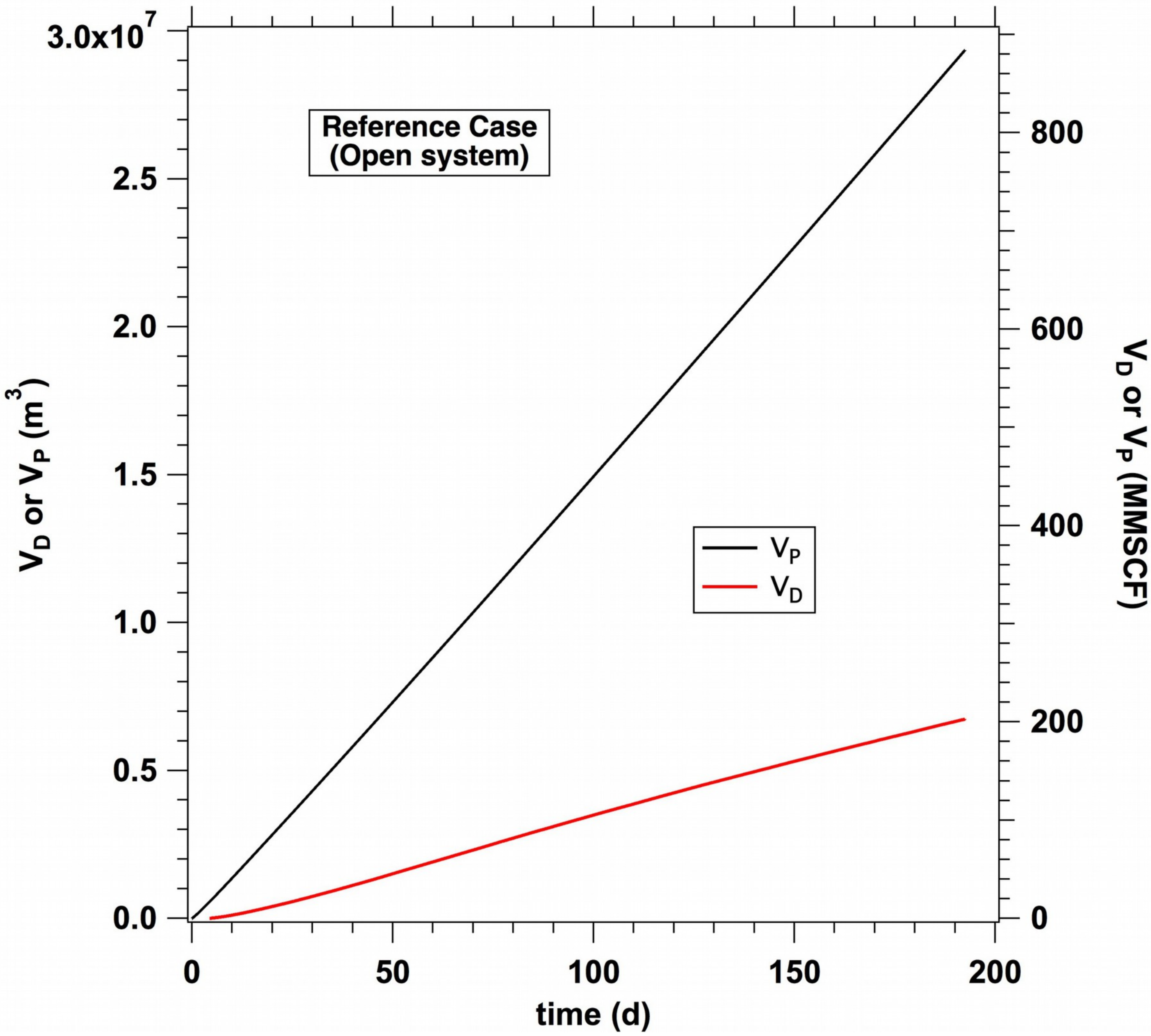

Figure 9. Reference Case R (open system): Cumulative volumes of released and produced gas (V_D and V_P, respectively) over time during the planned long-term test at Site NGHP-02-09 of the KG Basin. Note that V_D < V_P at all times.

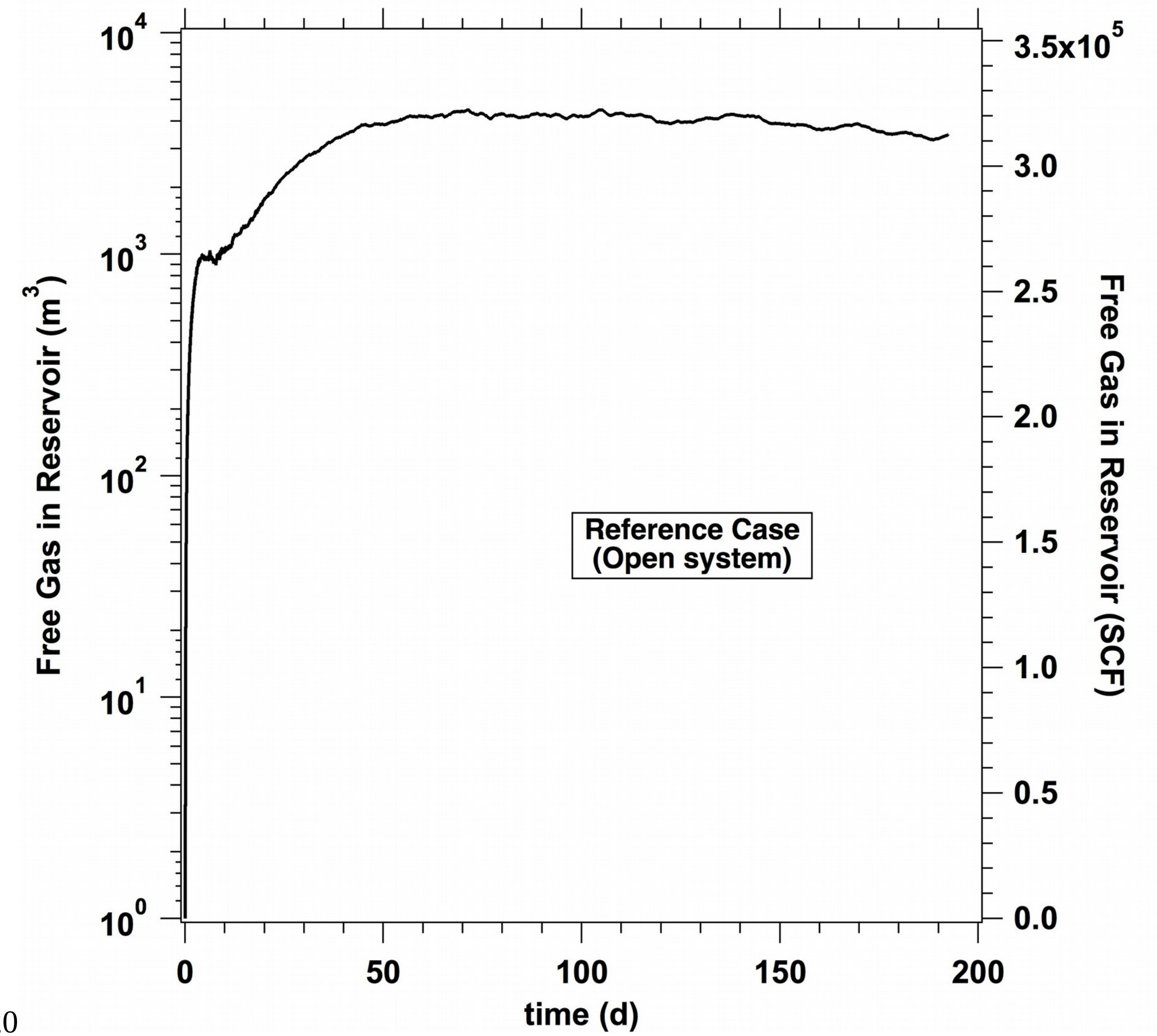

Figure 10. Reference Case R (open system): evolution of the volume of the free gas phase in the reservoir (V_F) over time during the planned long-term test at Site NGHP-02-09 of the KG Basin. Note the modest V_F magnitude and its relative stability for t > 50 days.

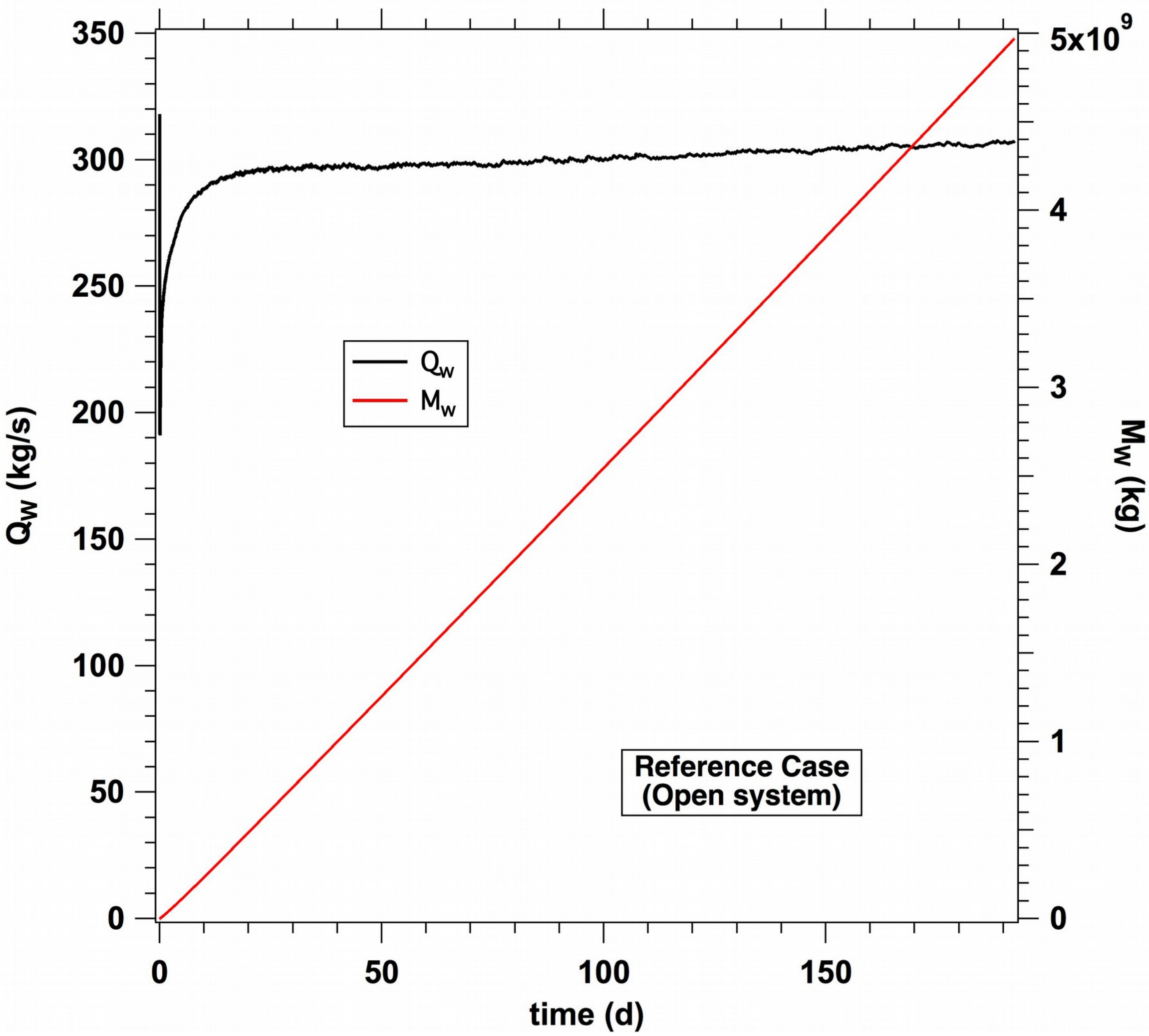

Figure 11. Reference Case R (open system): evolution of (a) the rate of water production (Q_W) and (b) the cumulative mass of water (M_W) over time during the planned long-term test at Site NGHP-02-09 of the KG Basin. Note the non-declining Q_W for practically the entire test period.

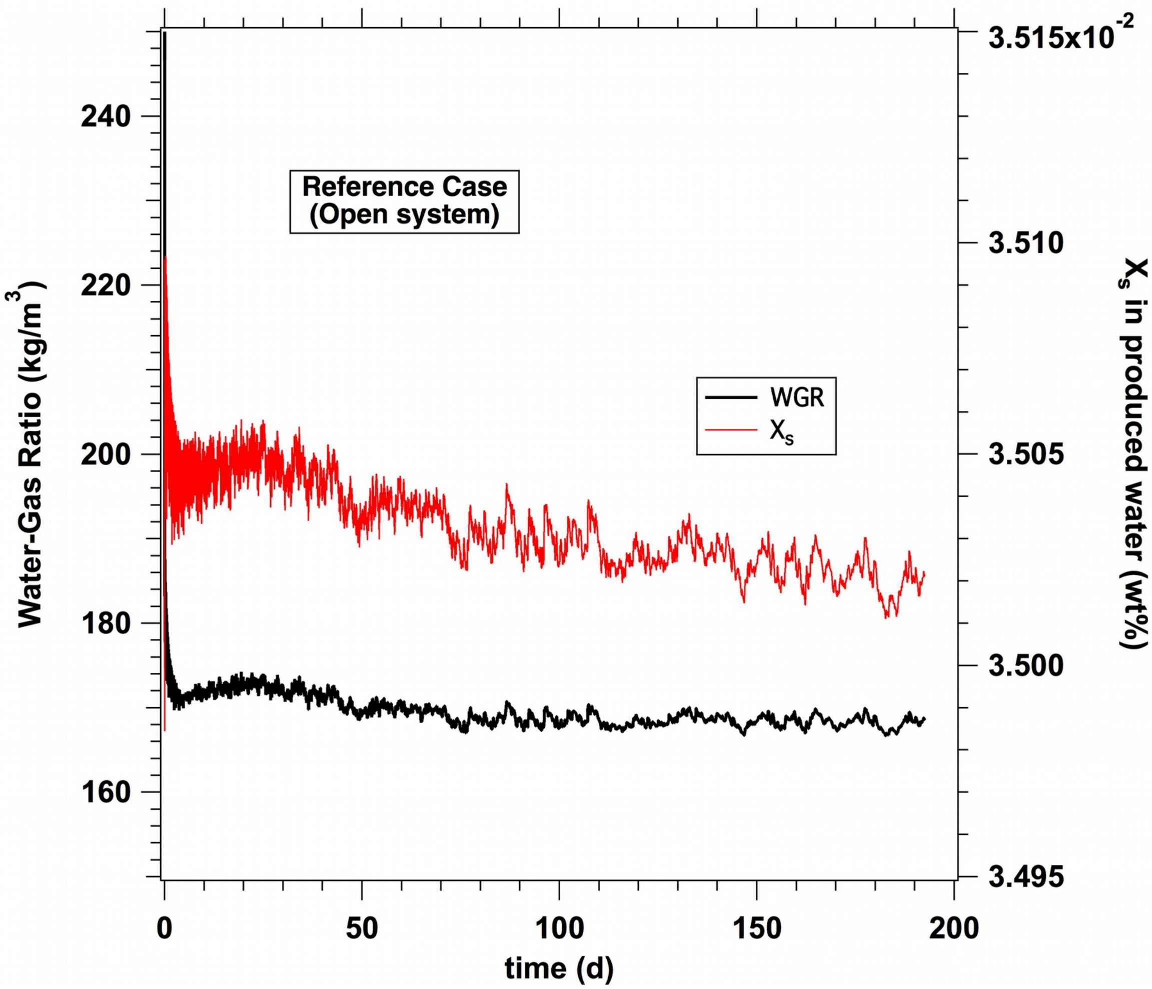

Figure 12. Reference Case R (open system): evolution of (a) the water-to-gas ratio (*WGR*) and (b) the salt mass fraction X_s in the produced water during the planned long-term test at Site NGHP-02-09 of the KG Basin. Note the high-value (and stability) of WGR during the test period, and the high level of X_s.

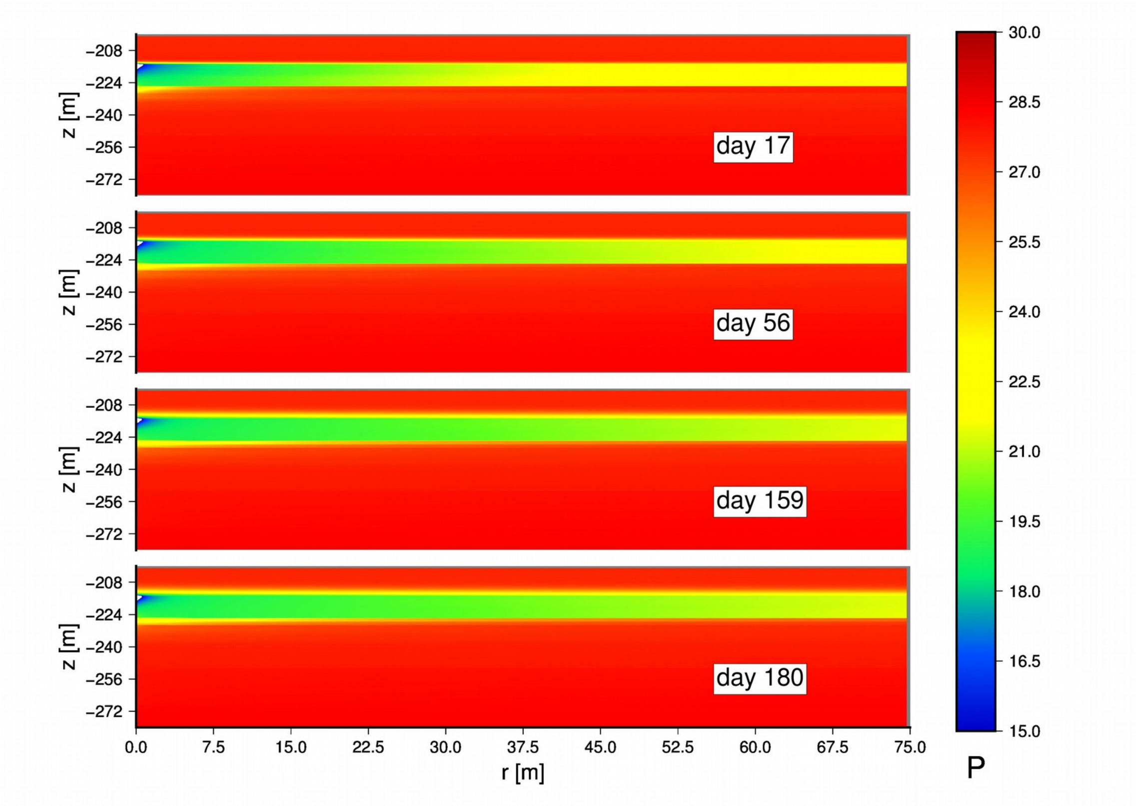

Figure 13. Case R: Evolution of pressure (in MPa) distribution in the system during the long-term production test at Site NGHP-02-09 of the KG Basin (P_w = 3 MPa).

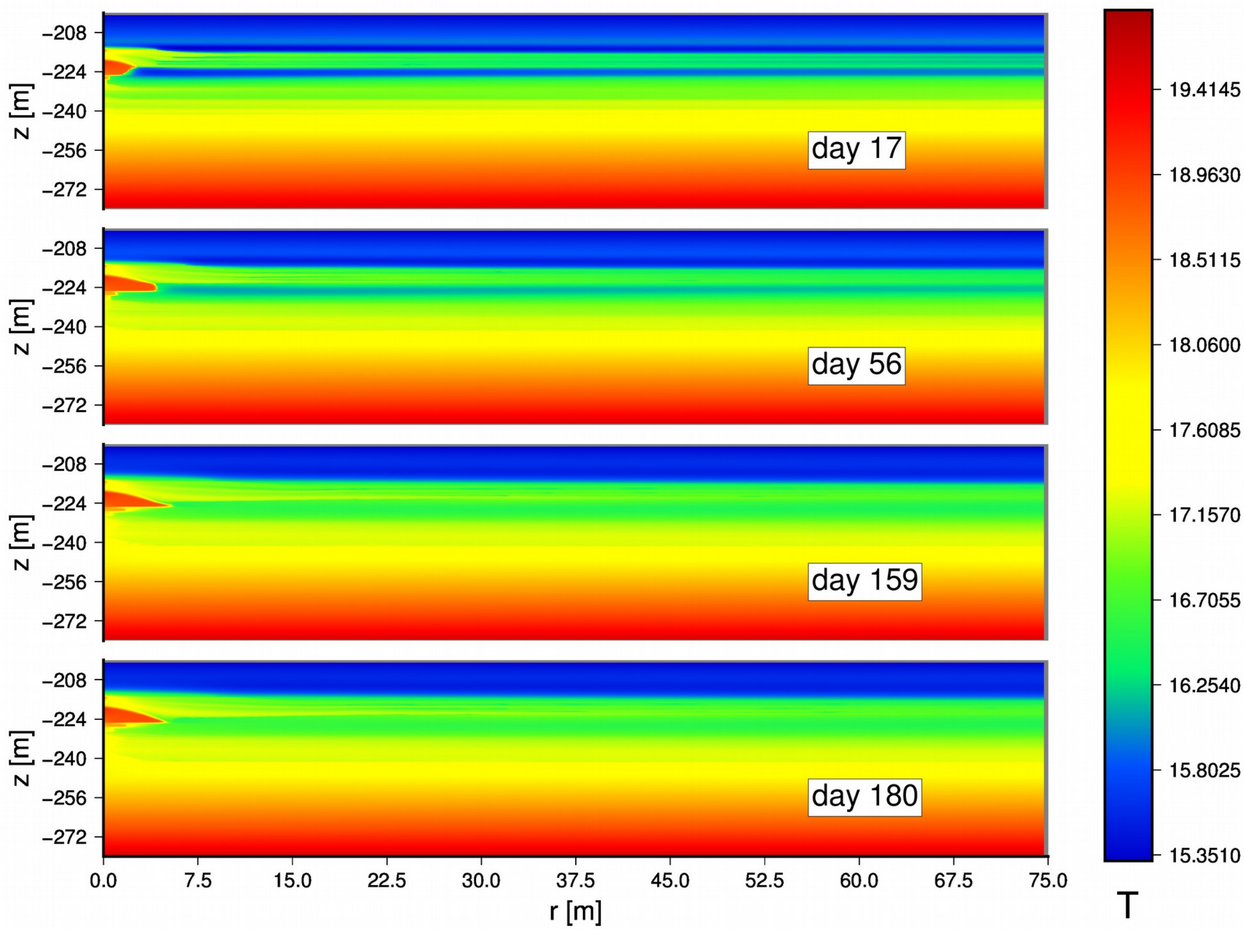

Figure 14. Case R: Evolution of temperature (in ºC) distribution in the system during the long-term production test at Site NGHP-02-09 of the KG Basin (P_w = 3 MPa).

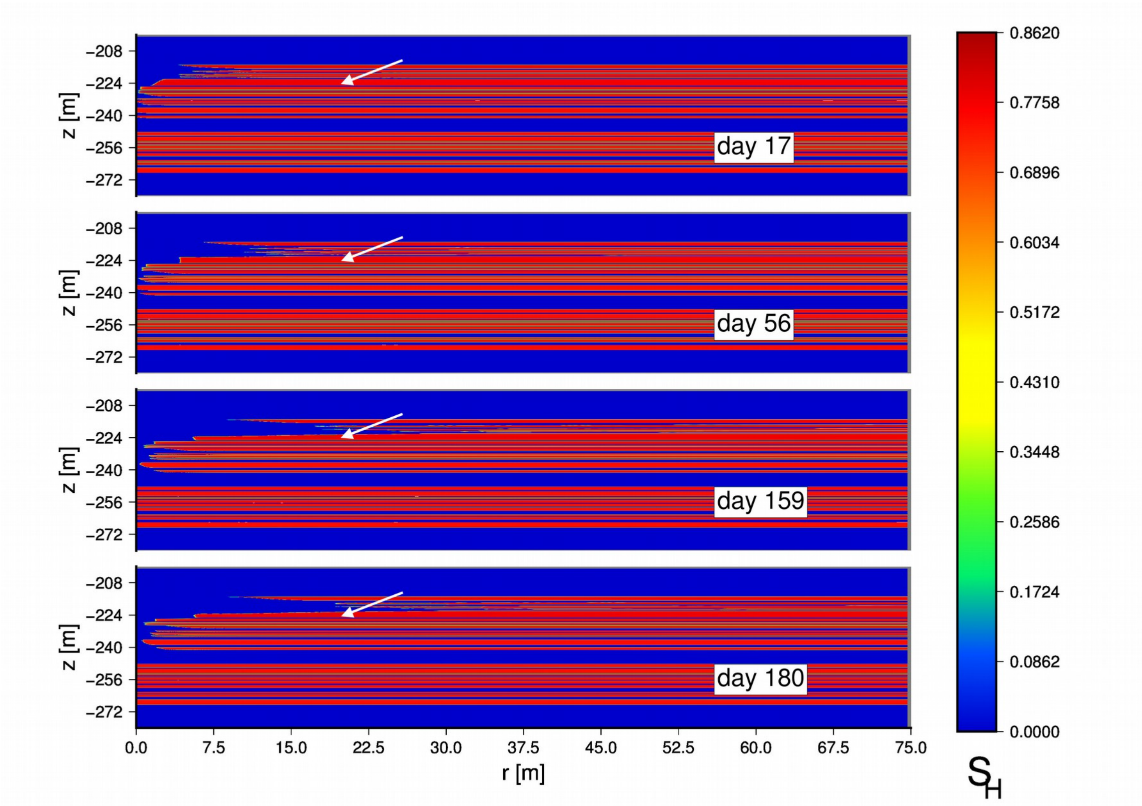

Figure 15. Case R: Evolution of the hydrate saturation S_H distribution in the system during the long-term production test at Site NGHP-02-09 of the KG Basin (P_w = 3 MPa). Arrows indicate layers where S_H > 0.75.

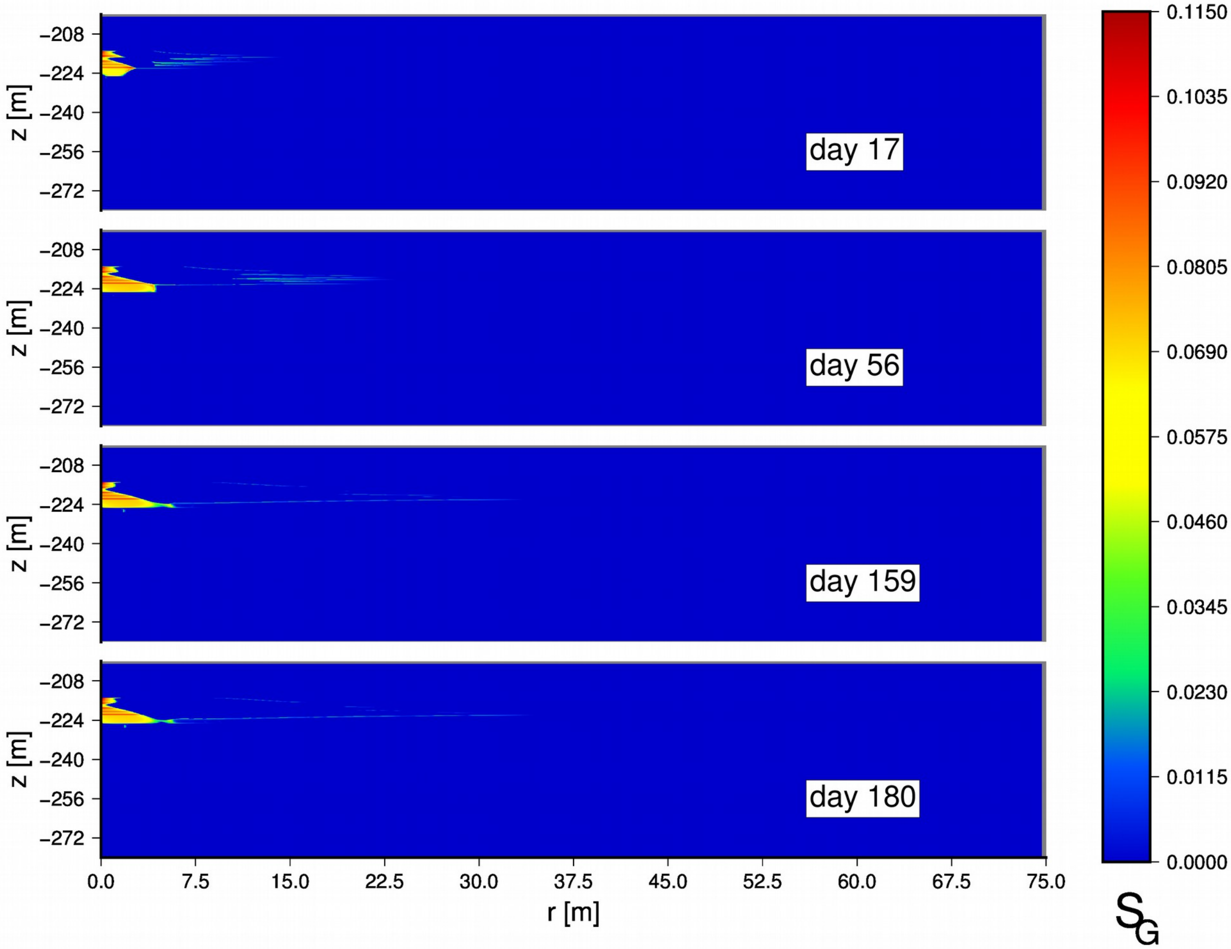

Figure 16. Case R: Evolution of the gas saturation S_G distribution in the system during the long-term production test at Site NGHP-02-09 of the KG Basin (P_w = 3 MPa).

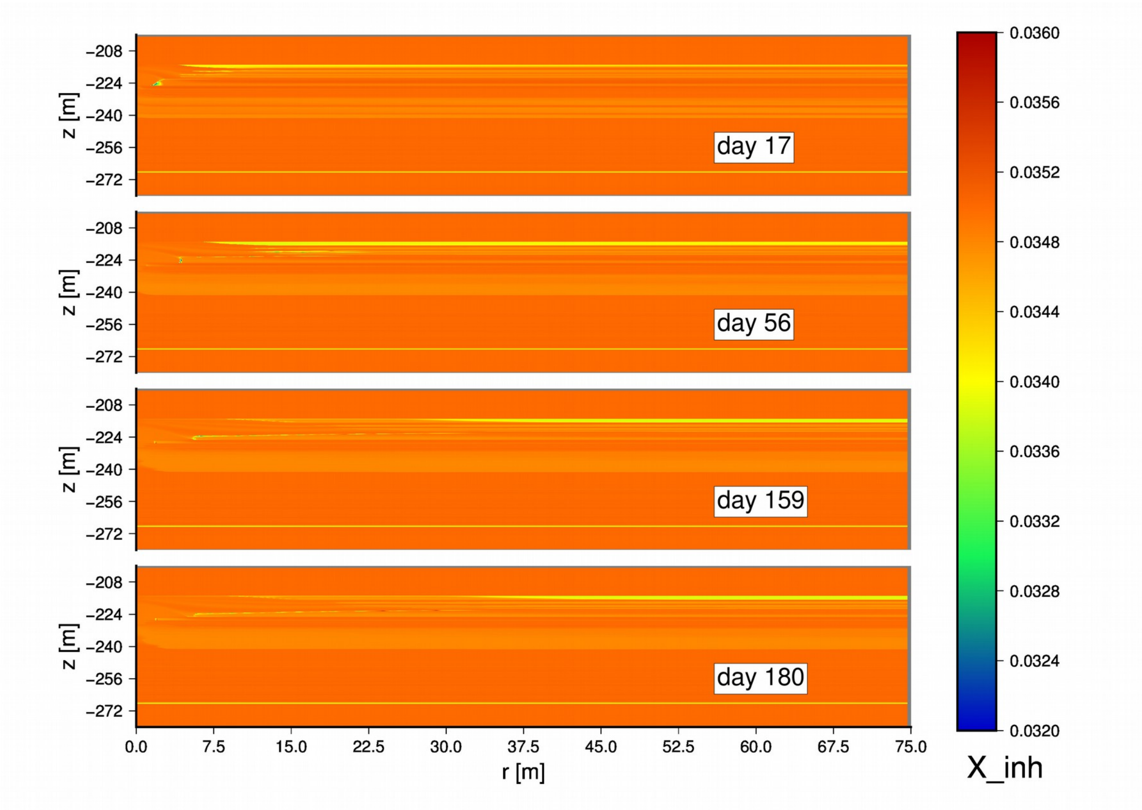

Figure 17. Case R: Evolution of the distribution of the salt mass fraction X_S in the aqueous phase of the system during the long-term production test at Site NGHP-02-09 of the KG Basin.

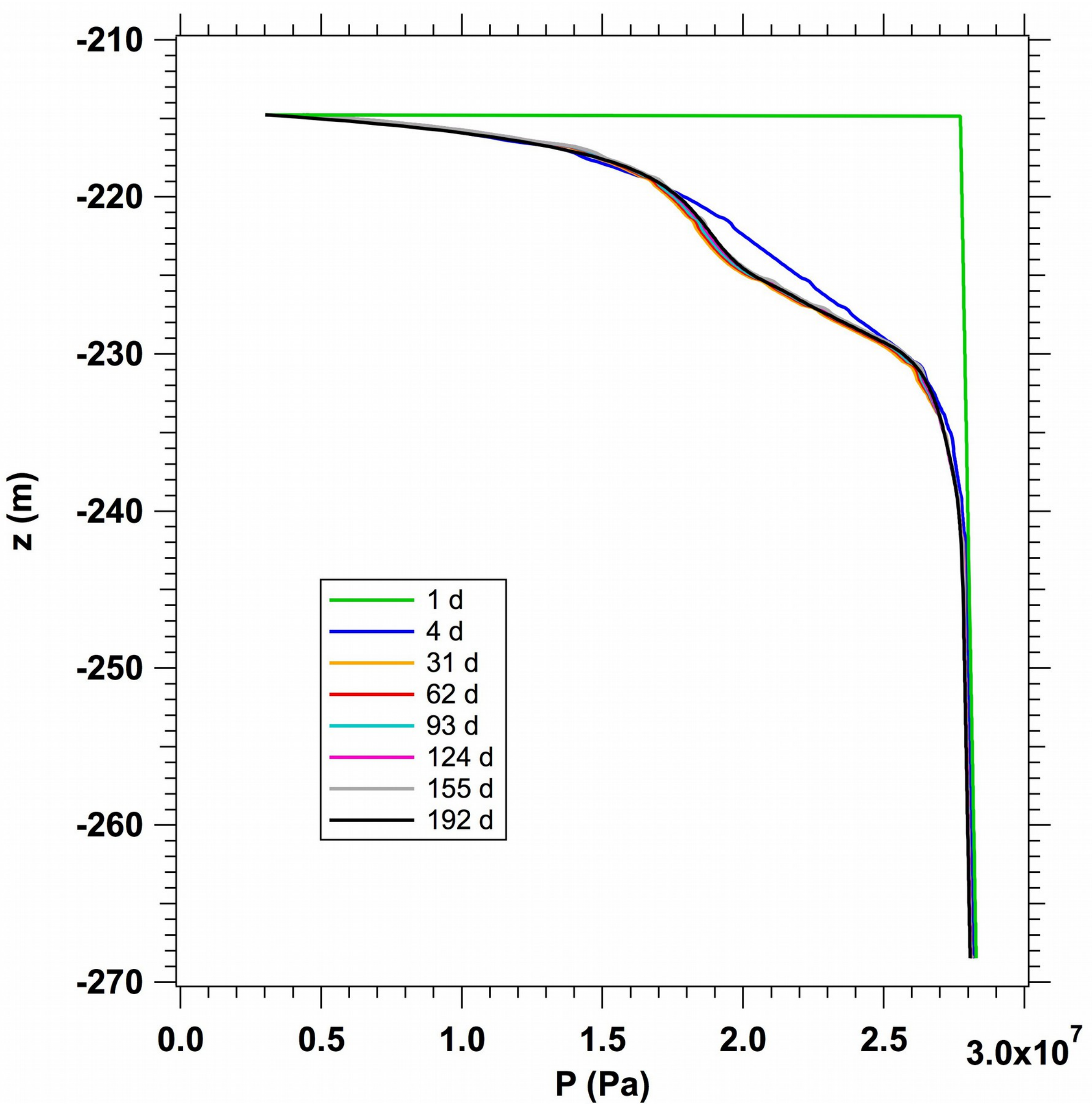

Figure 18. Case R: Evolution of the pressure distribution with depth at the well during the long-term production test at Site NGHP-02-09 of the KG Basin (P_w = 3 MPa). Note the lack of pressure response below z = -240 m (from the ocean floor), where the thick, highly permeable aquifer horizon "Aqu09" begins.

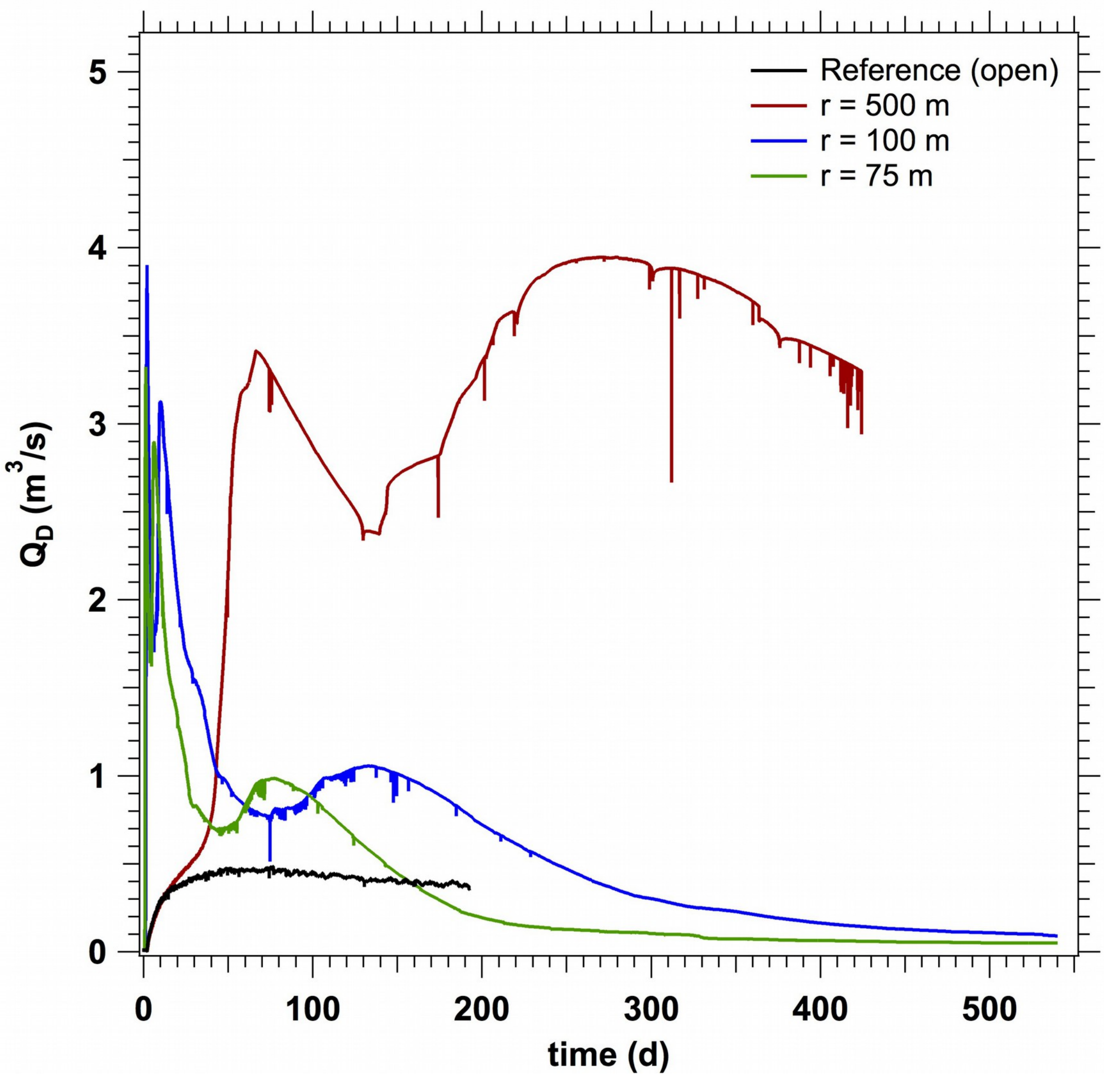

Figure 19. Cases C1, C2, C3 (closed systems): evolution of the rate of gas release from dissociation (Q_D) over time during multi-well operations at Site NGHP-02-09 of the KG Basin. The Q_D for the reference Case R (open system) is included for comparison.

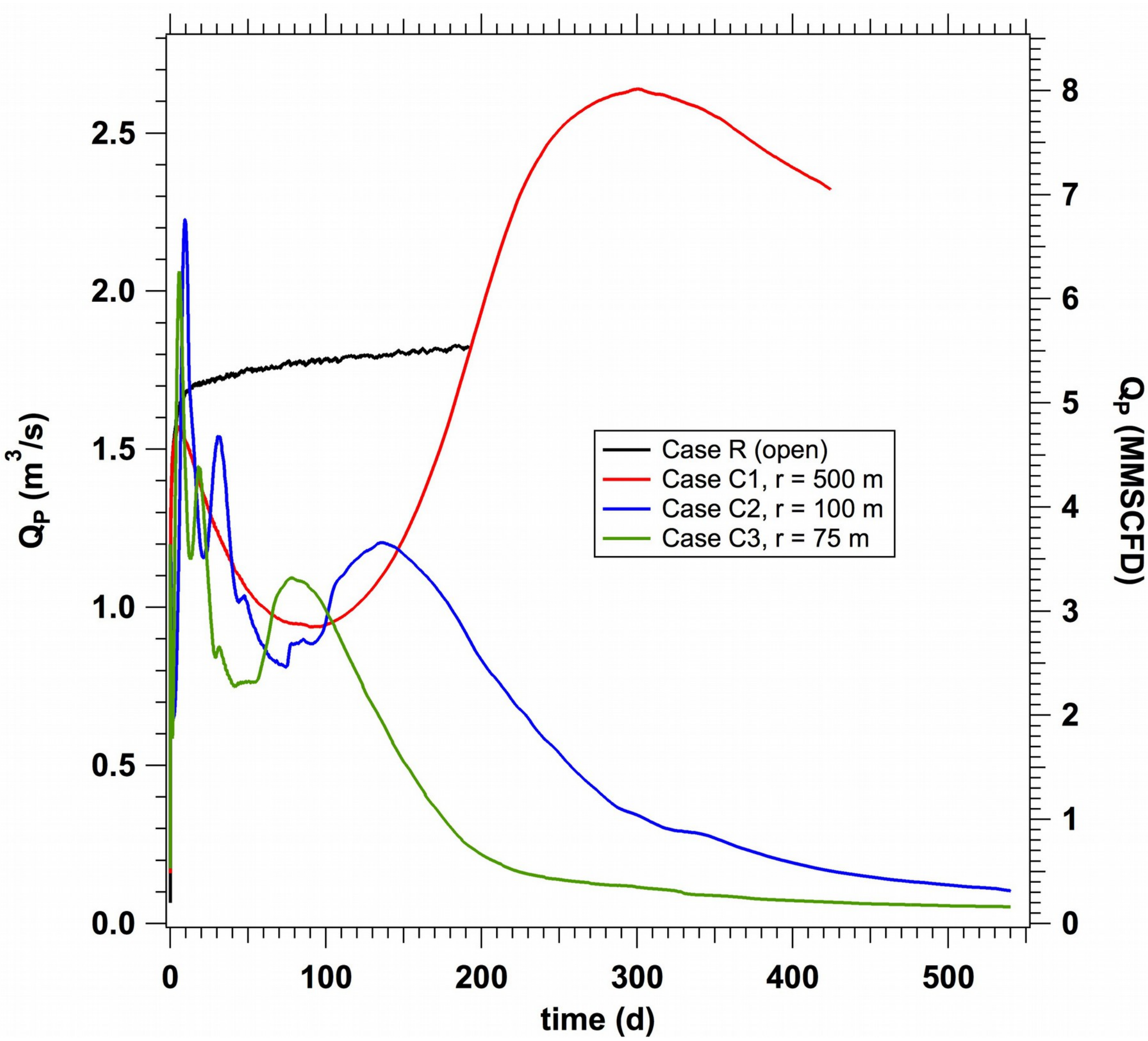

Figure 20. Cases C1, C2, C3 (closed systems): evolution of the rate of gas production (Q_P) over time during long-term multi-well operations at Site NGHP-02-09 of the KG Basin. The Q_P for the reference Case R (open system) is included for comparison.

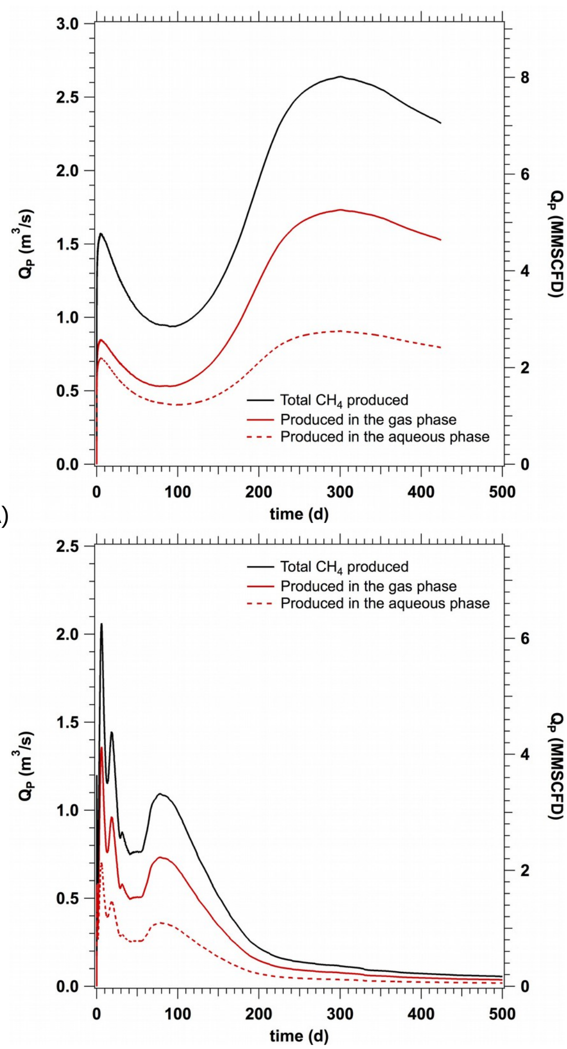

A) B)

Figure 21. Provenance of gas in the production rate Q_P in Case C1 (A) and Case C3 (B).

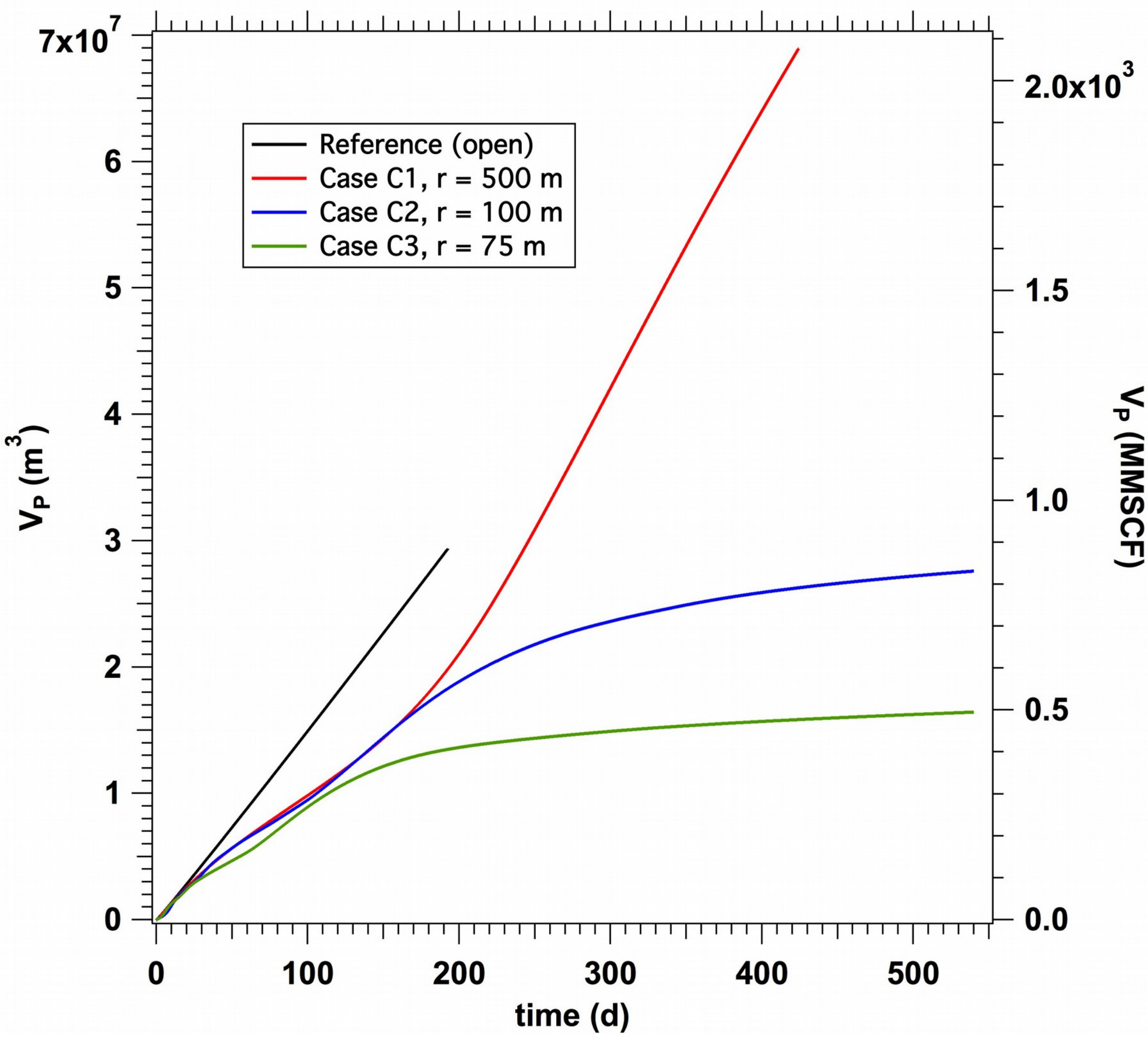

Figure 22. Cases C1, C2, C3 (closed systems): evolution of the volume of produced gas (V_P) over time during multi-well operations at Site NGHP-02-09 of the KG Basin. The V_P for the reference Case R (open system) is included for comparison.

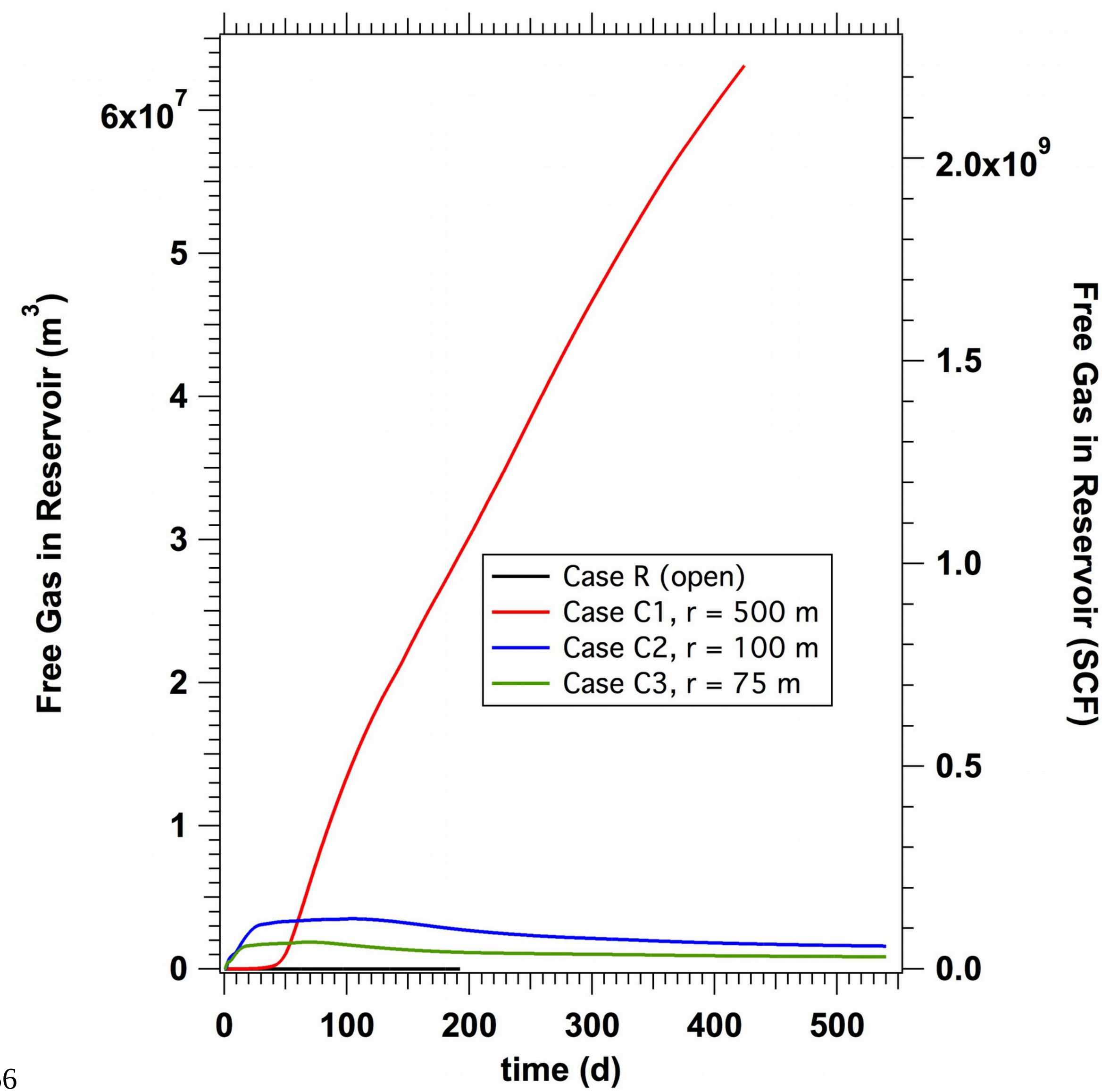

Figure 23. Cases C1, C2, C3 (closed systems): evolution of the volume of free gas in the reservoir (V_F) over time during multi-well operations at Site NGHP-02-09 of the KG Basin. The V_F for the reference Case R (open system) that is included for comparison is significantly smaller than for any other case.

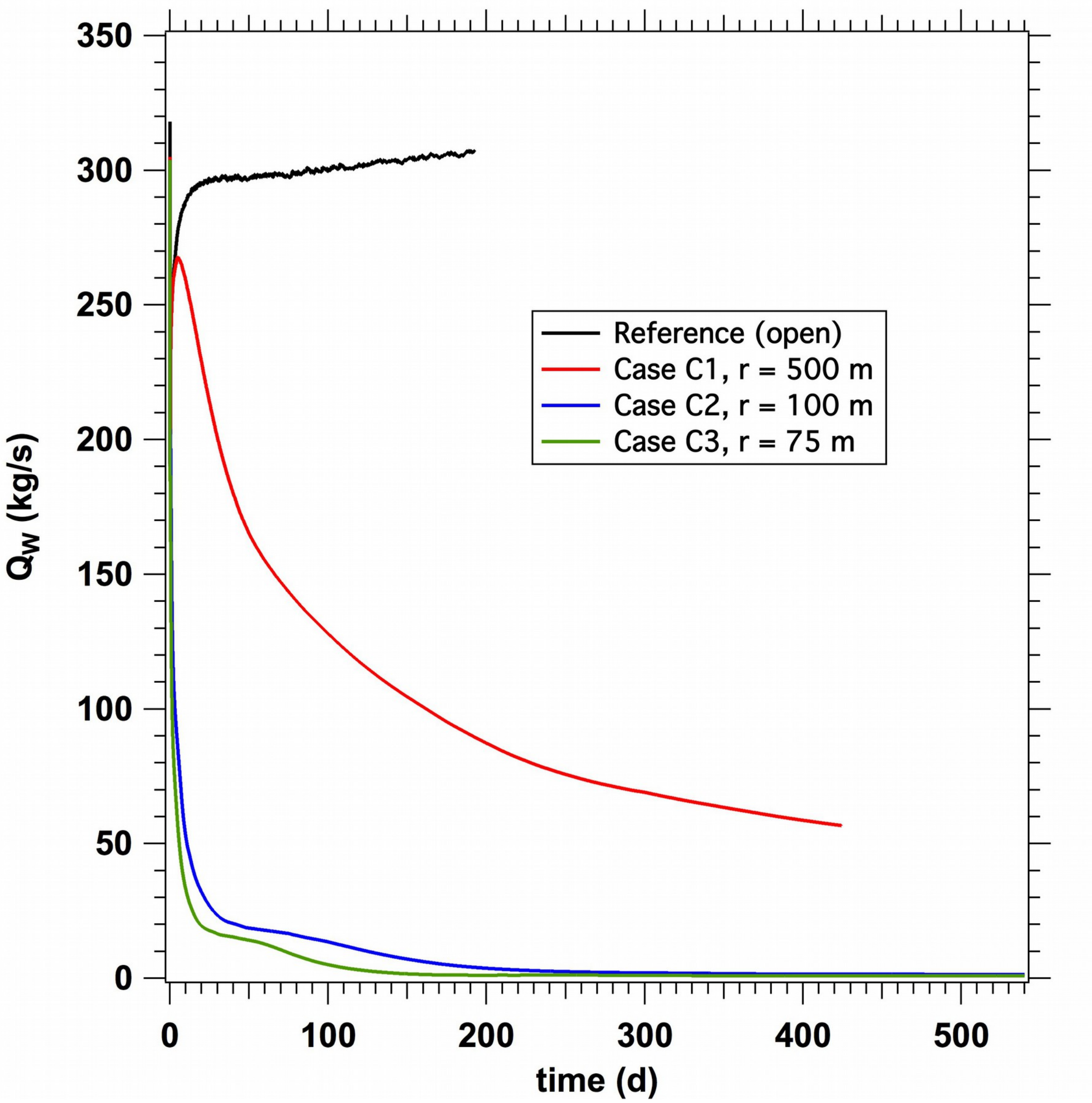

Figure 24. Cases C1, C2, C3 (closed systems): evolution of the mass rate of water production (Q_w) over time during multi-well operations at Site NGHP-02-09 of the KG Basin. The Q_w for the reference Case R (open system) that is included for comparison has a distinctly different behavior.

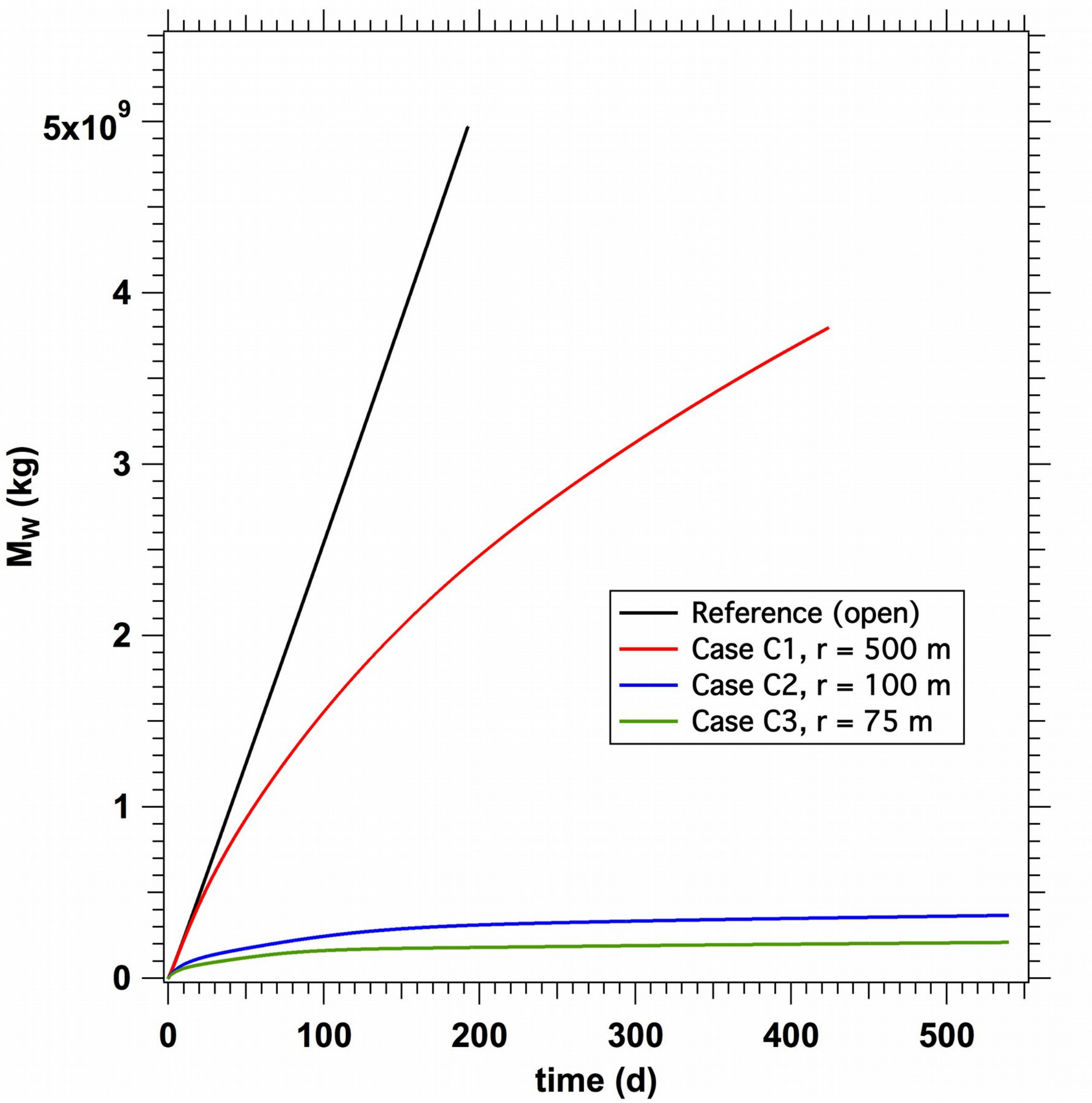

Figure 25. Cases C1, C2, C3 (closed systems): evolution of the cumulative mass of produced water (M_W) over time during multi-well operations at Site NGHP-02-09 of the KG Basin. The M_W for the reference Case R (open system) that is included for comparison is significantly larger than in any other case.

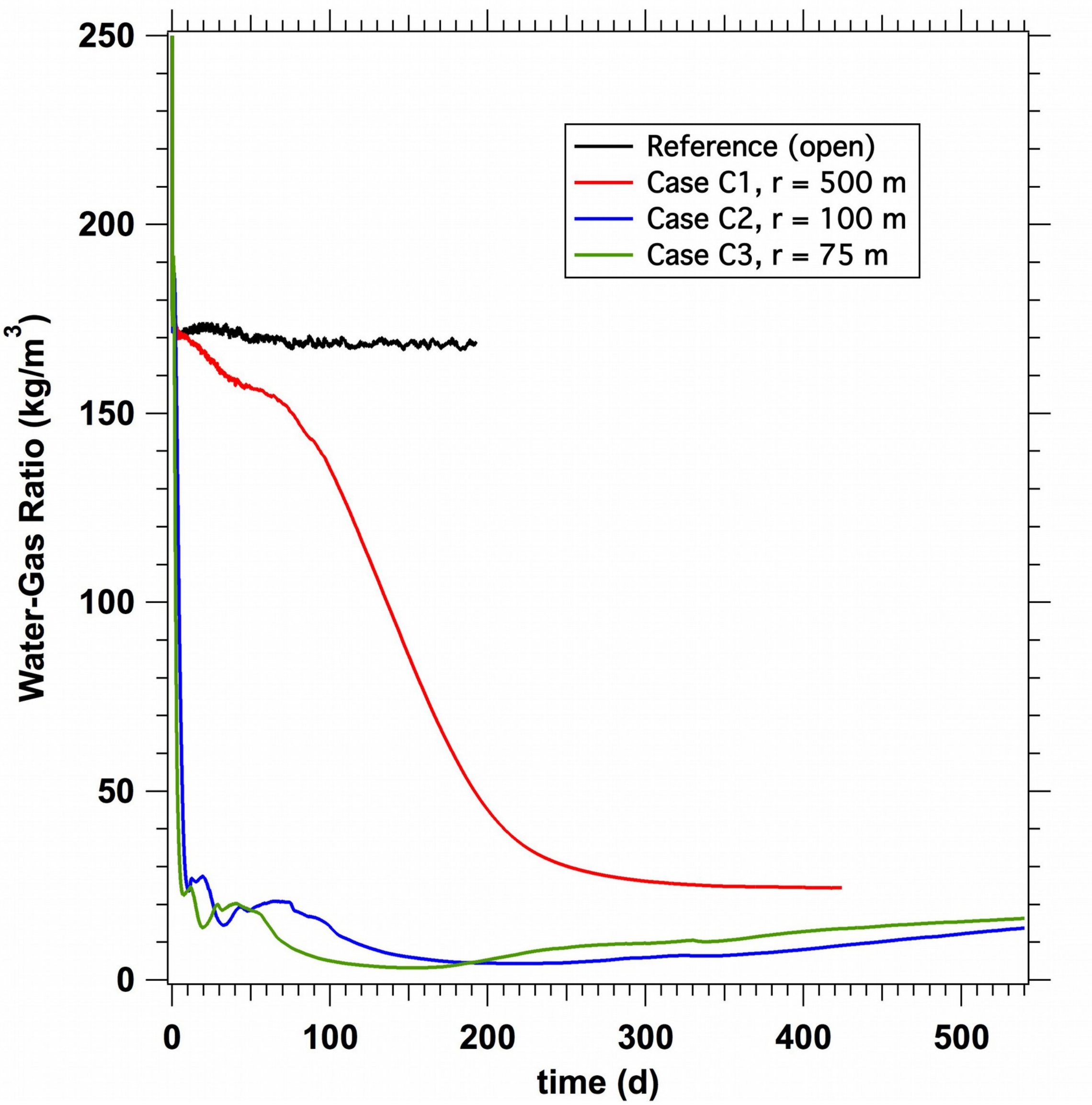

Figure 26. Cases C1, C2, C3 (closed systems): evolution of the water-to-gas ratio (*WGR*) over time during multi-well operations at Site NGHP-02-09 of the KG Basin. Note the different behavior of the *WGR* for the reference Case R (open system) that is included for comparison.

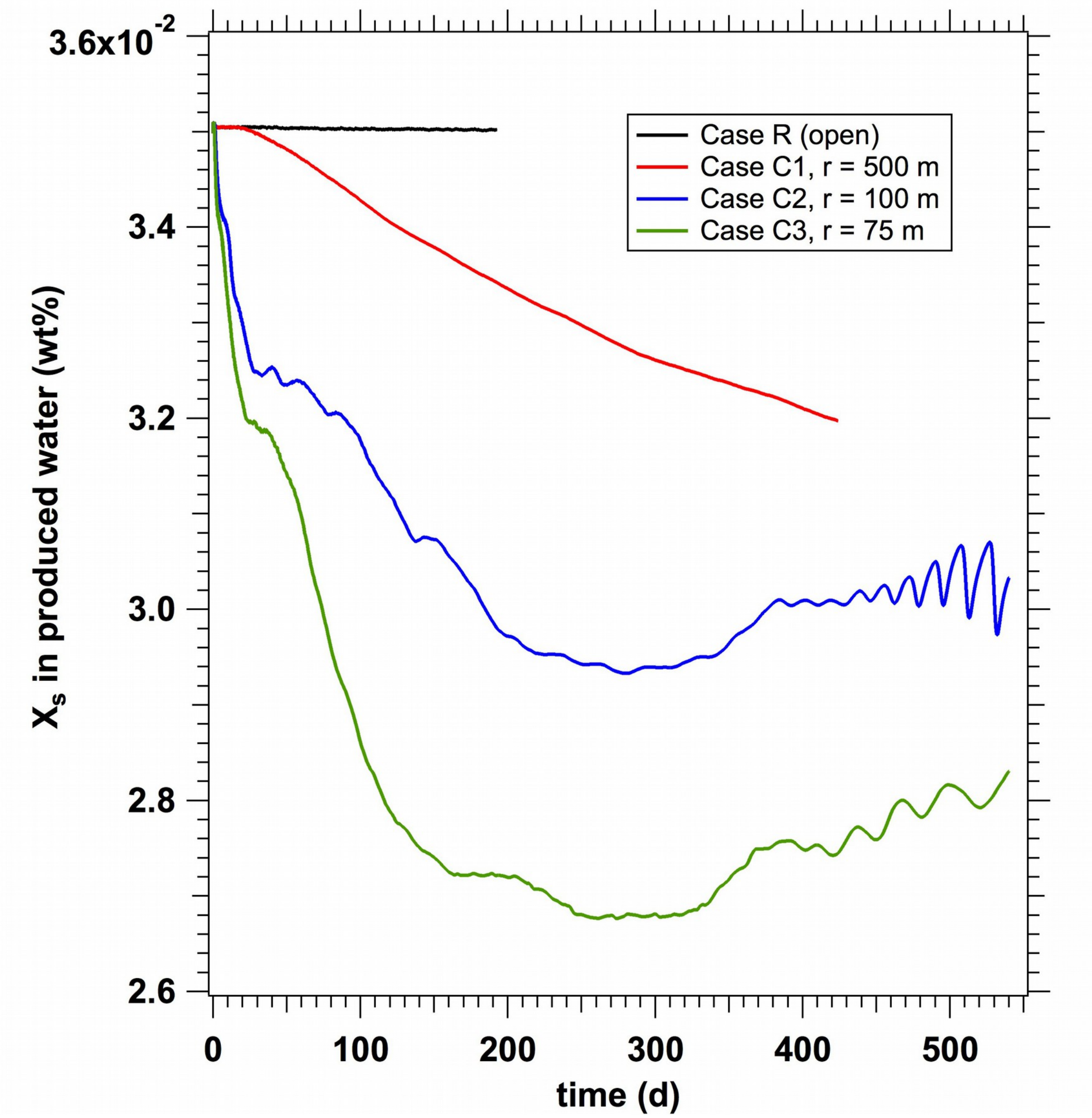

Figure 27. Cases C1, C2, C3 (closed system): evolution of the salt mass fraction in the produced water (X_S) over time during multi-well operations at Site NGHP-02-09 of the KG Basin. Note the different behavior of the X_S in the reference Case R (open system) that is included for comparison.

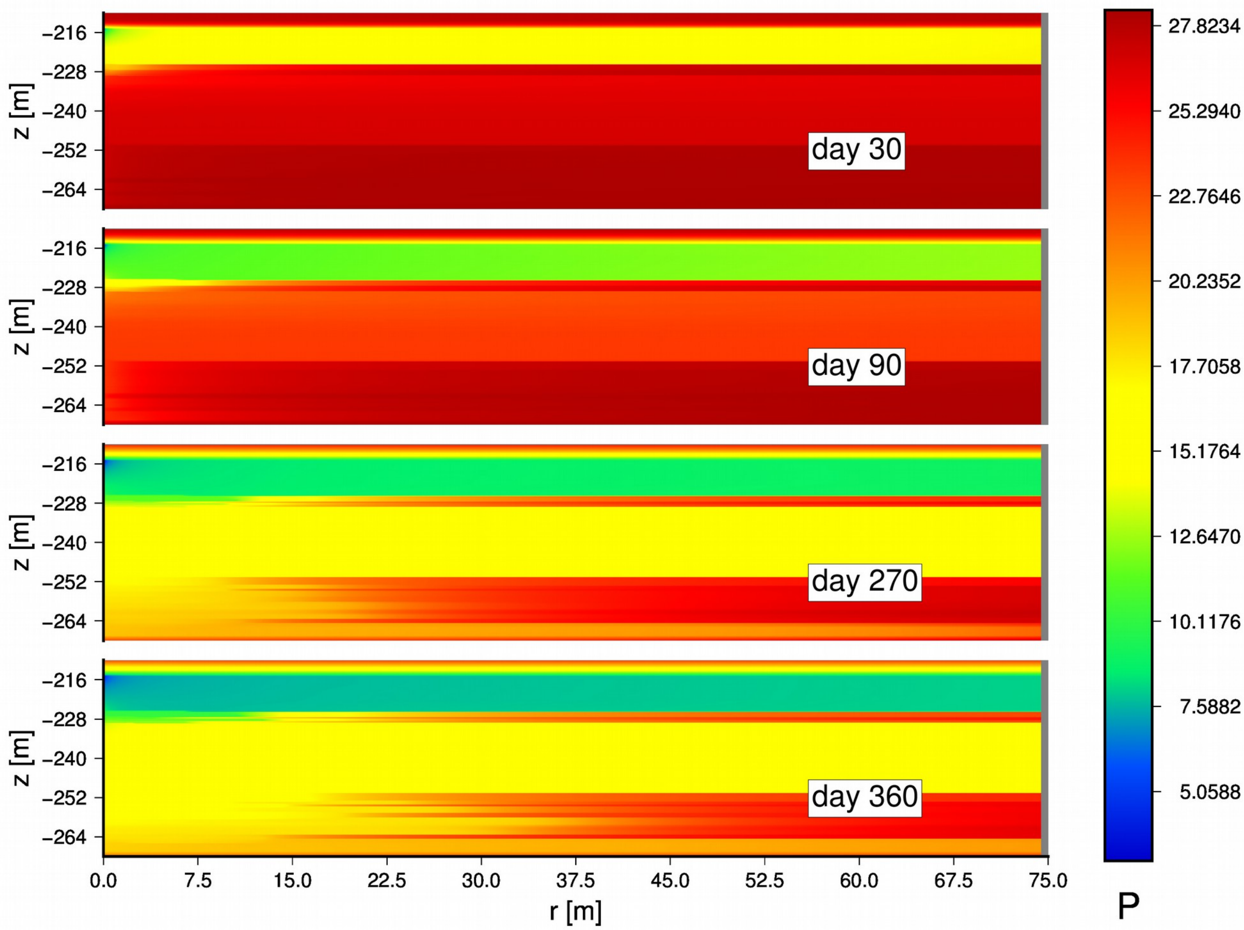

Figure 28. Case C1: Evolution of pressure (in MPa) distribution in the system during multi-well production operations at Site NGHP-02-09 of the KG Basin (P_w = 3 MPa).

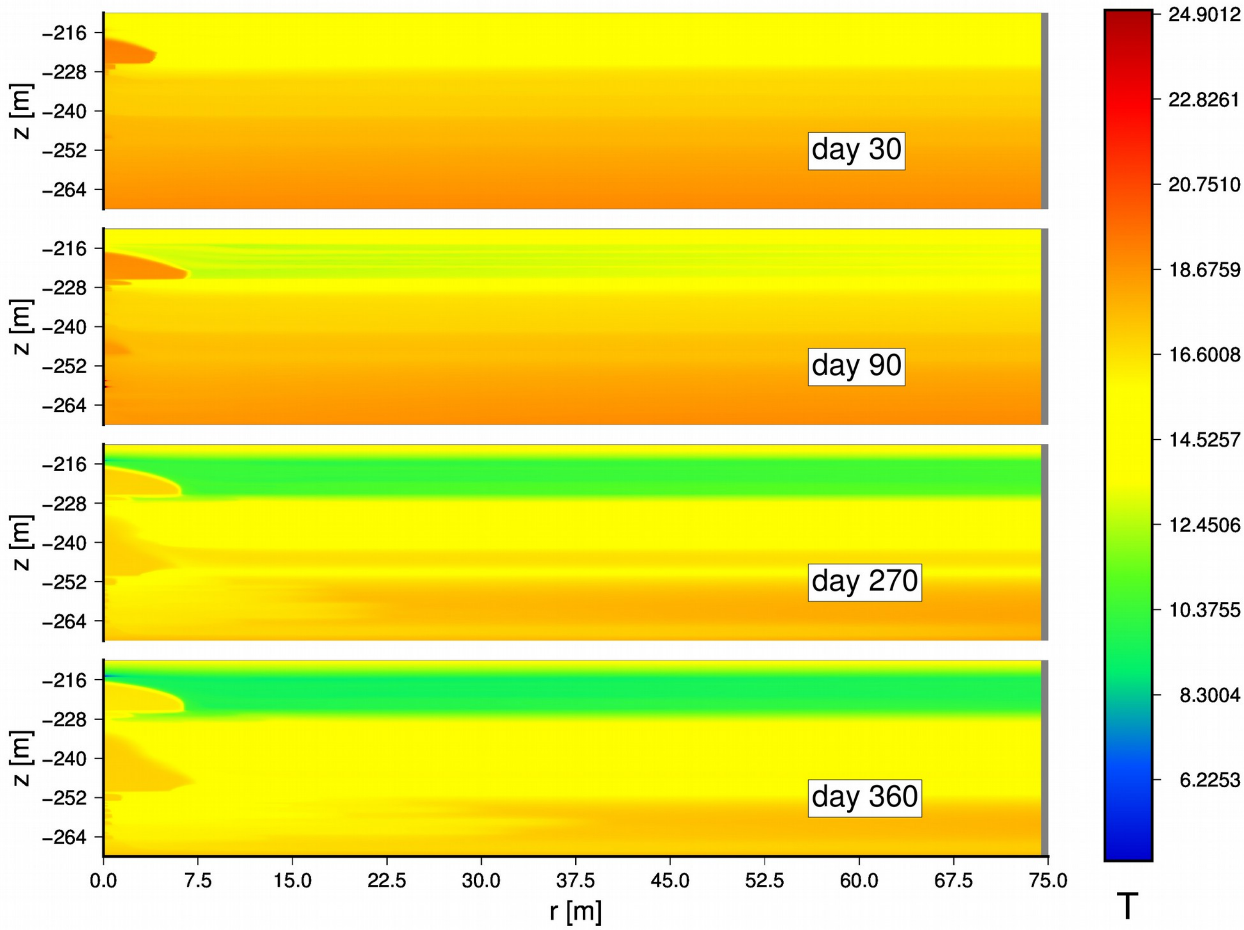

Figure 29. Case C1: Evolution of temperature (in ºC) distribution in the system during multi-well production operations at Site NGHP-02-09 of the KG Basin (P_w = 3 MPa).

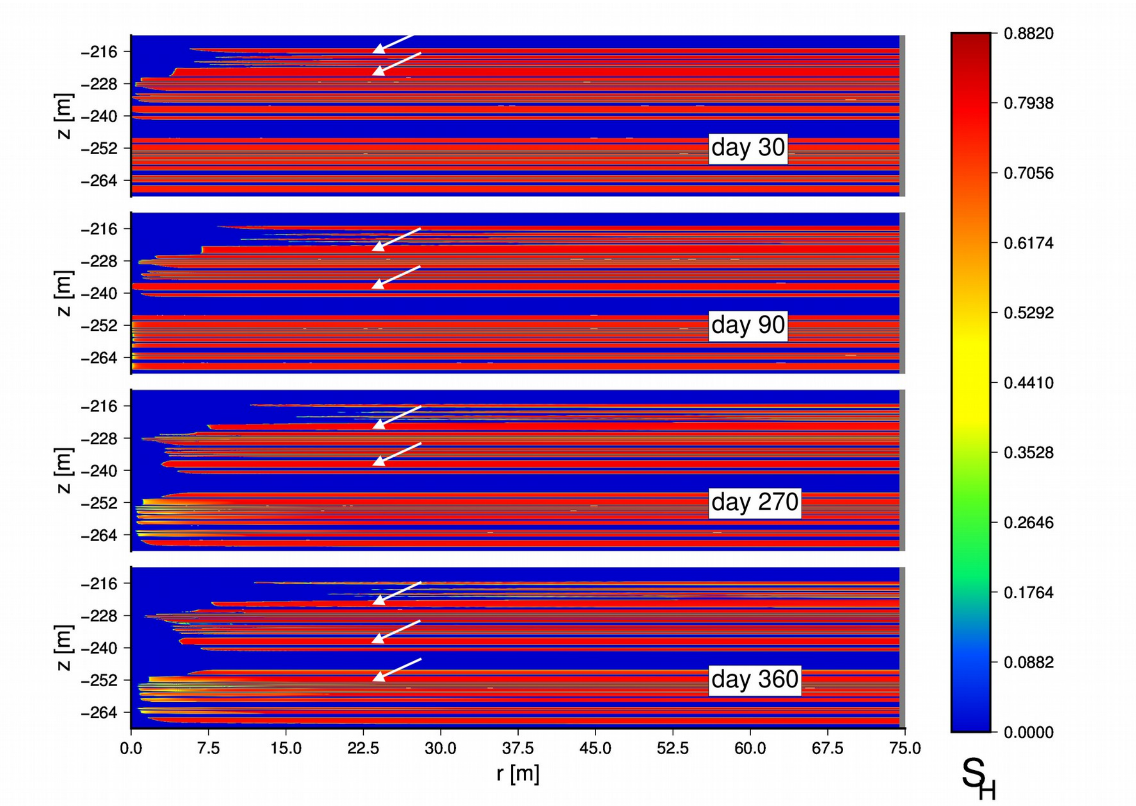

Figure 30. Case C1: Evolution of the hydrate saturation S_H distribution in the system during multi-well production operations at Site NGHP-02-09 of the KG Basin (P_w = 3 MPa). Arrows indicate hydrate layers with S_H > 0.75.

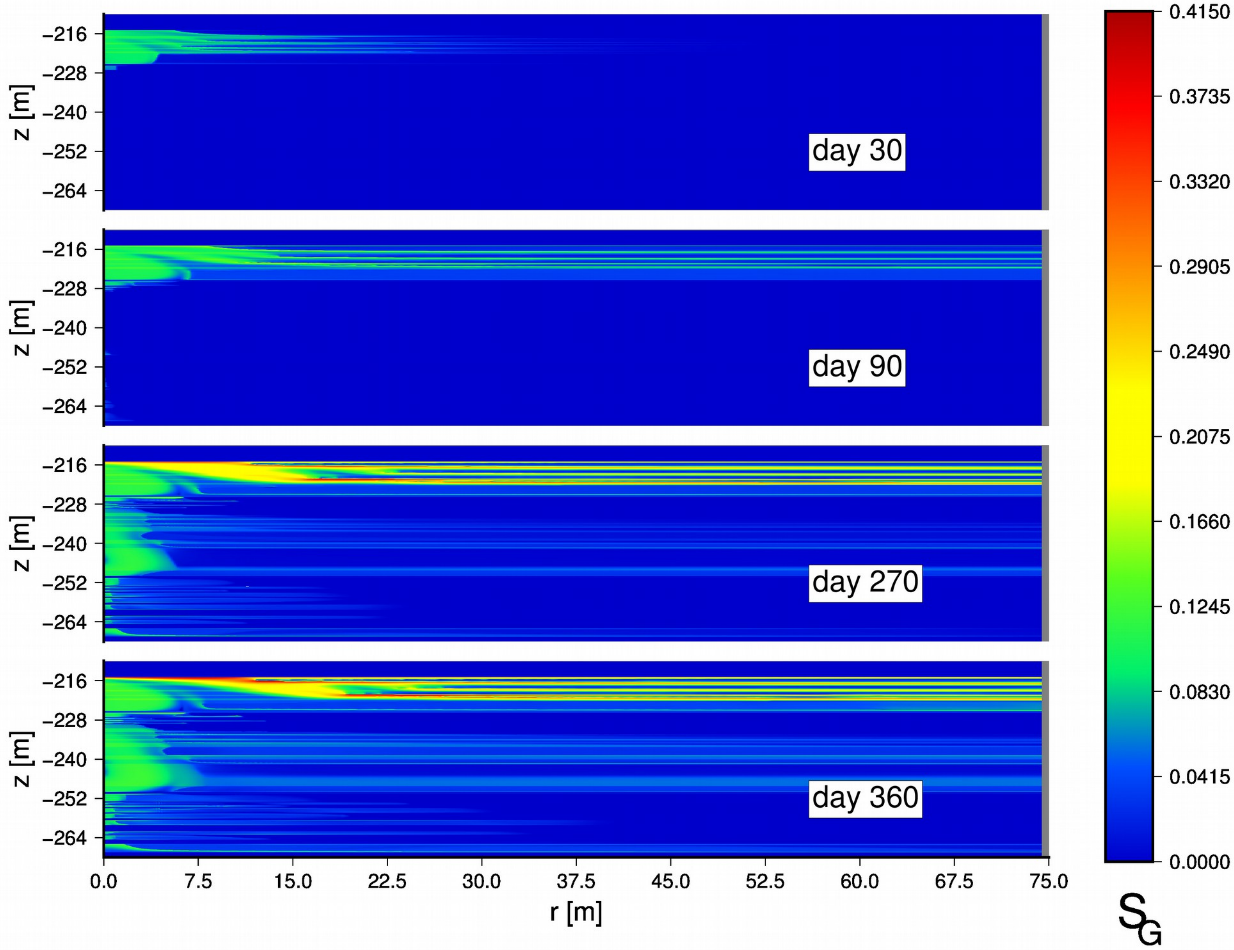

Figure 31. Case C1: Evolution of the gas saturation S_G distribution in the system during multi-well production operations at Site NGHP-02-09 of the KG Basin (P_w = 3 MPa).

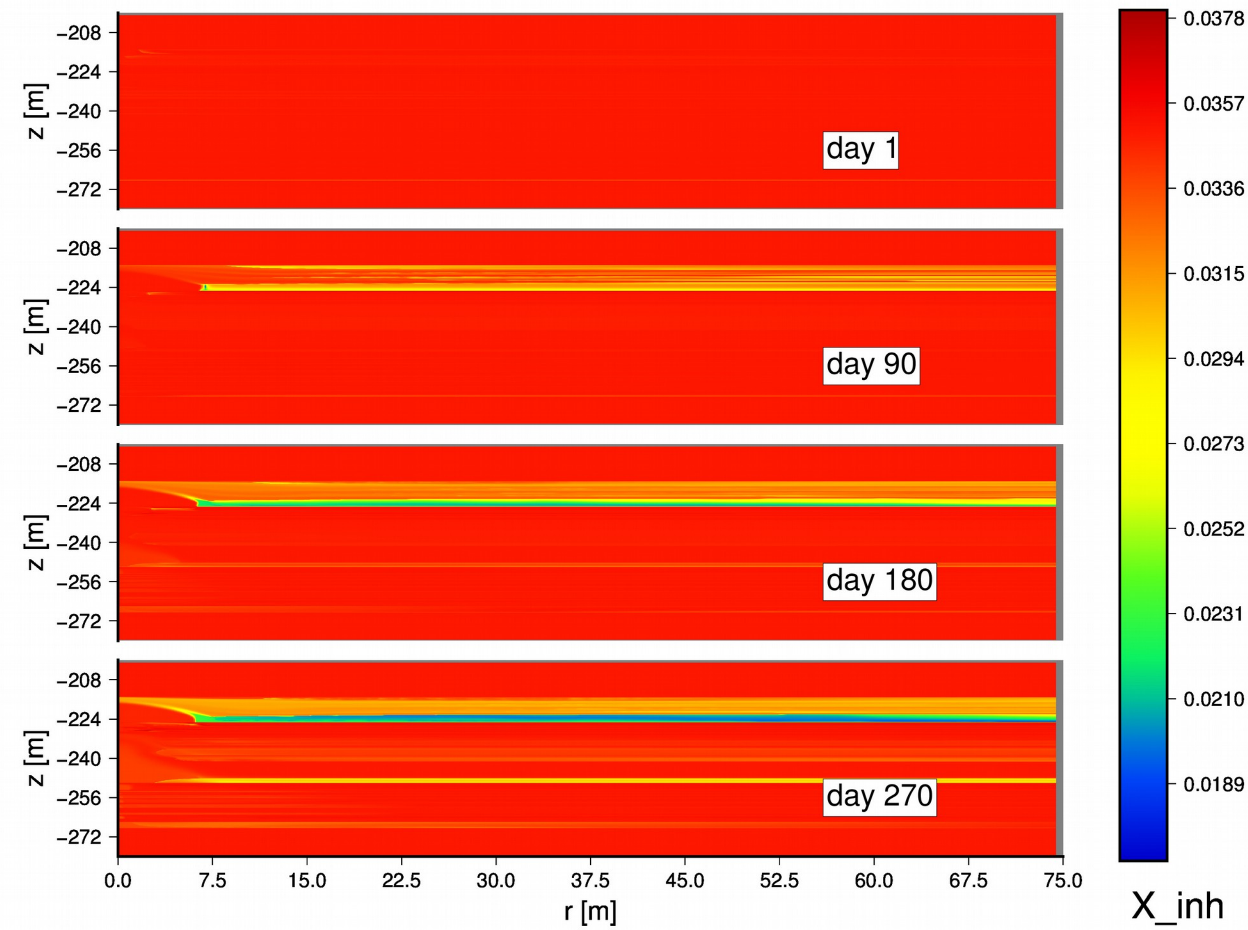

Figure 32. Case C1: Evolution of the distribution of the salt mass fraction X_S in the aqueous phase of the system during multi-well production operations at Site NGHP-02-09 of the KG Basin (P_w = 3 MPa).

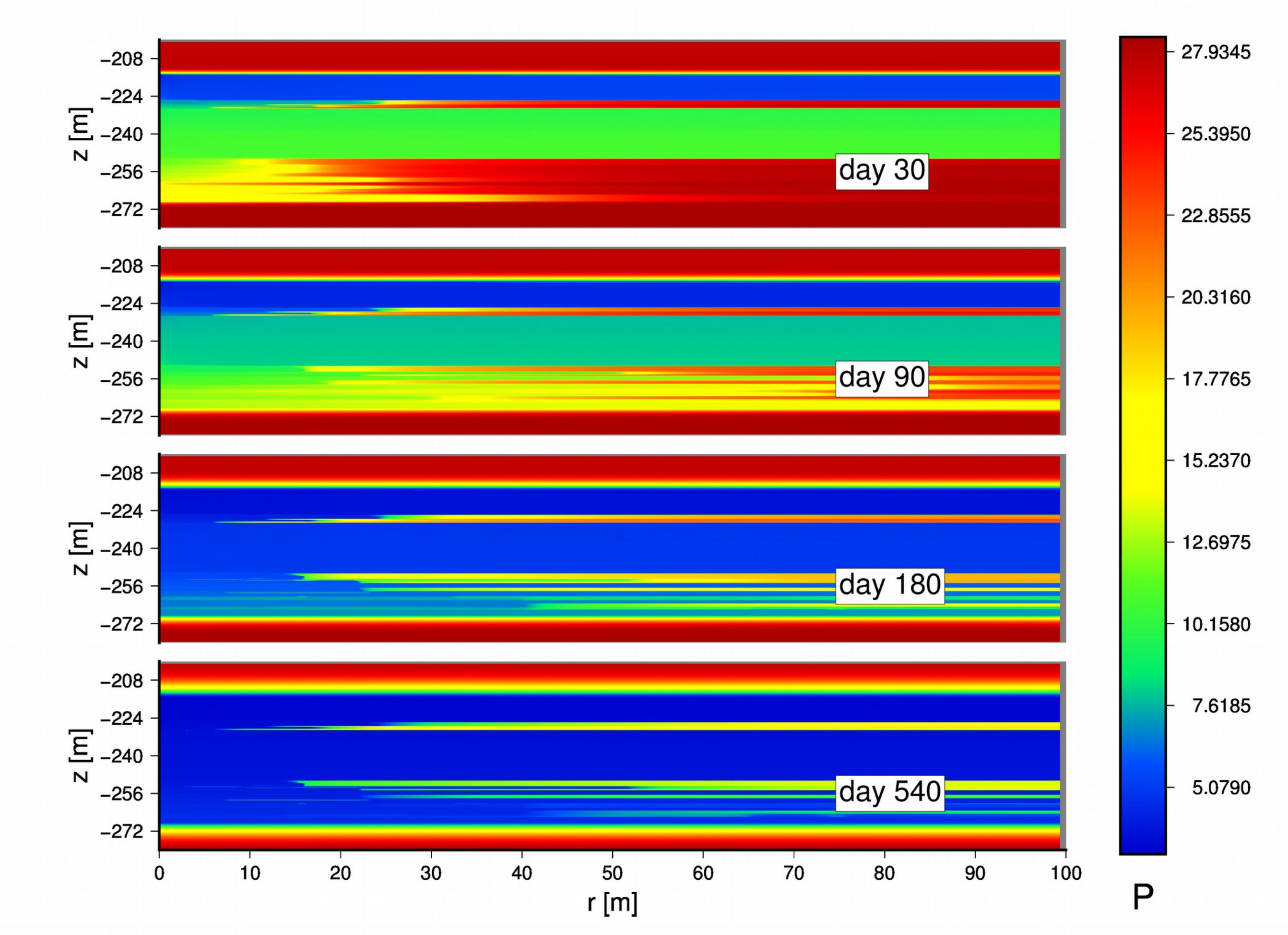

Figure 33. Case C2: Evolution of pressure (in MPa) distribution in the system during multi-well production operations at Site NGHP-02-09 of the KG Basin (P_w = 3 MPa).

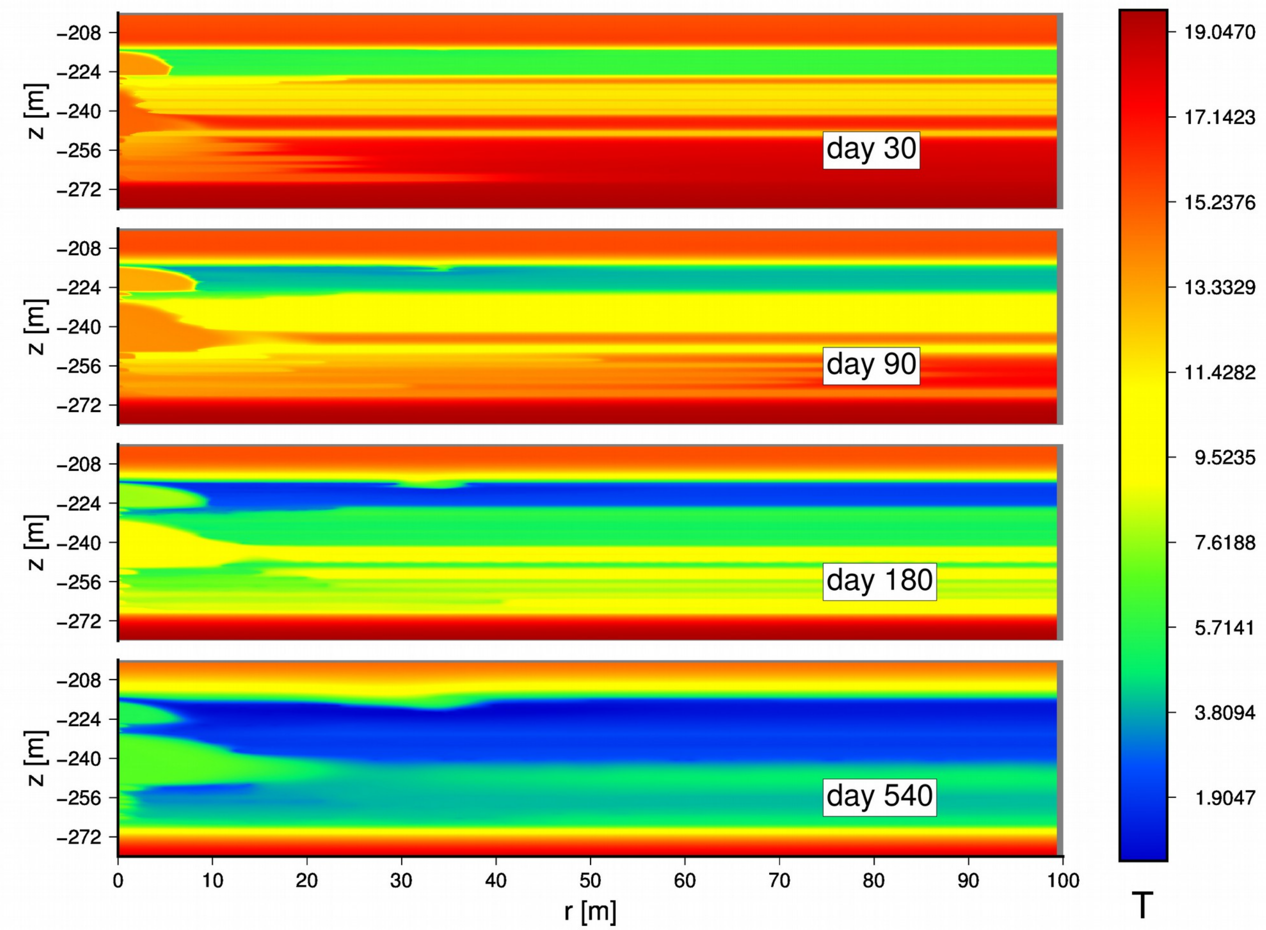

Figure 34. Case C2: Evolution of temperature (in ºC) distribution in the system during multi-well production operations at Site NGHP-02-09 of the KG Basin (P_w = 3 MPa).

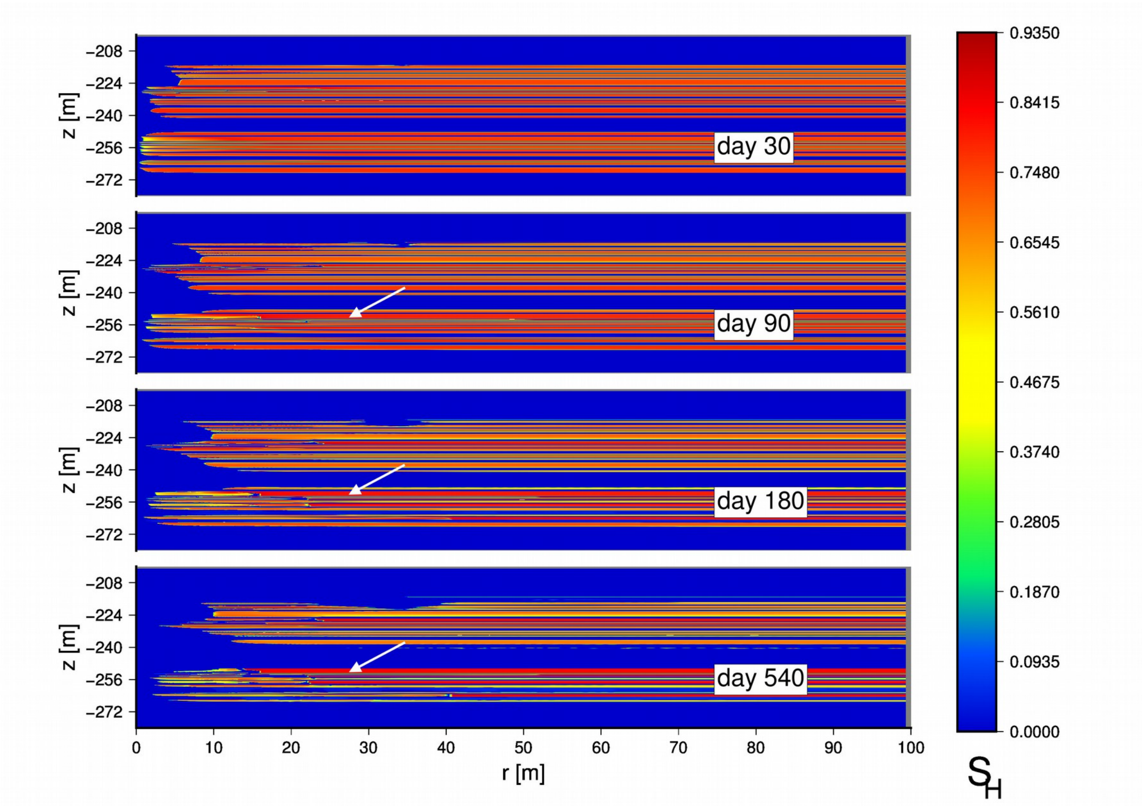

Figure 35. Case C2: Evolution of the hydrate saturation S_H distribution in the system during multi-well production operations at Site NGHP-02-09 of the KG Basin (P_w = 3 MPa). Arrows indicate hydrate layers with S_H > 0.75.

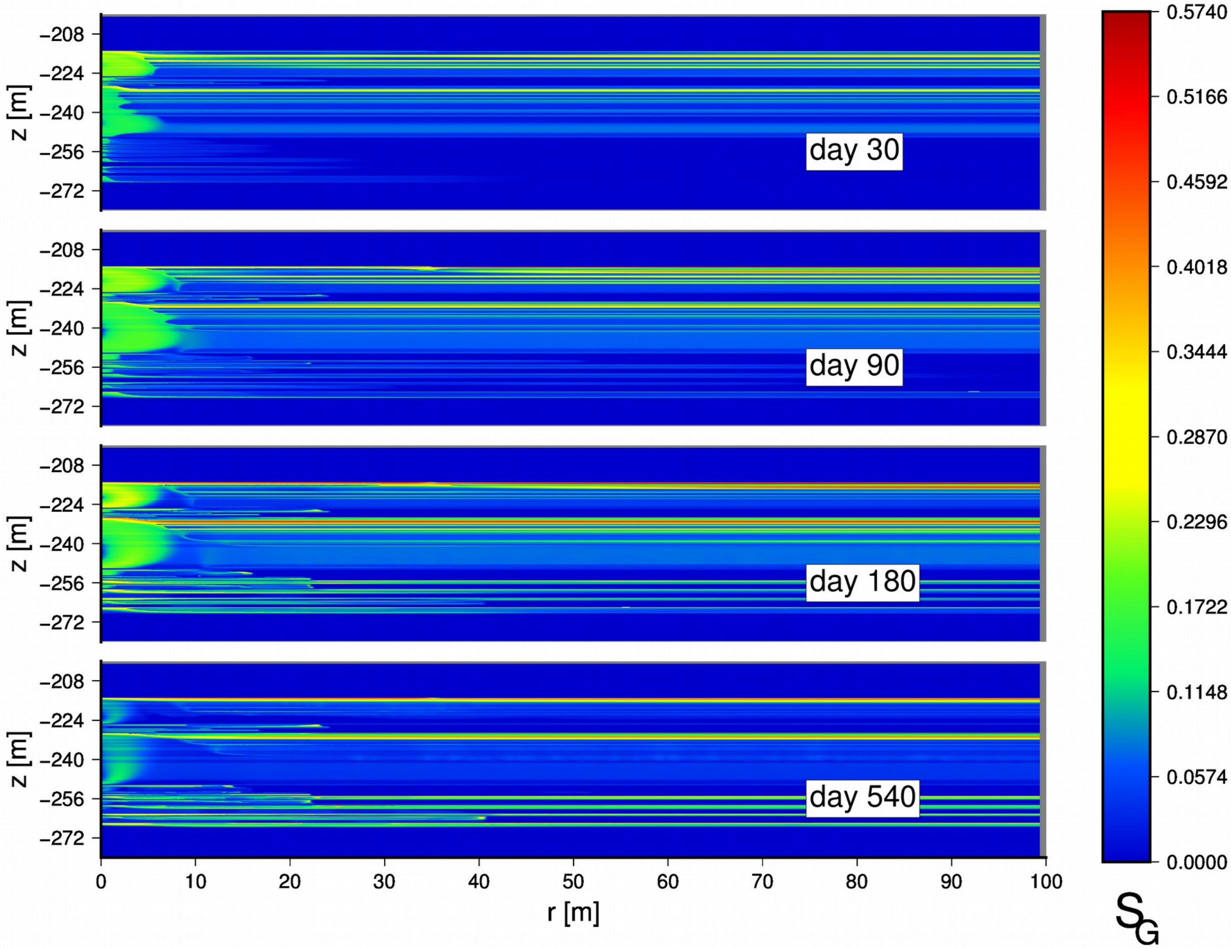

Figure 36. Case C2: Evolution of the gas saturation S_G distribution in the system during multi-well production operations at Site NGHP-02-09 of the KG Basin (P_w = 3 MPa).

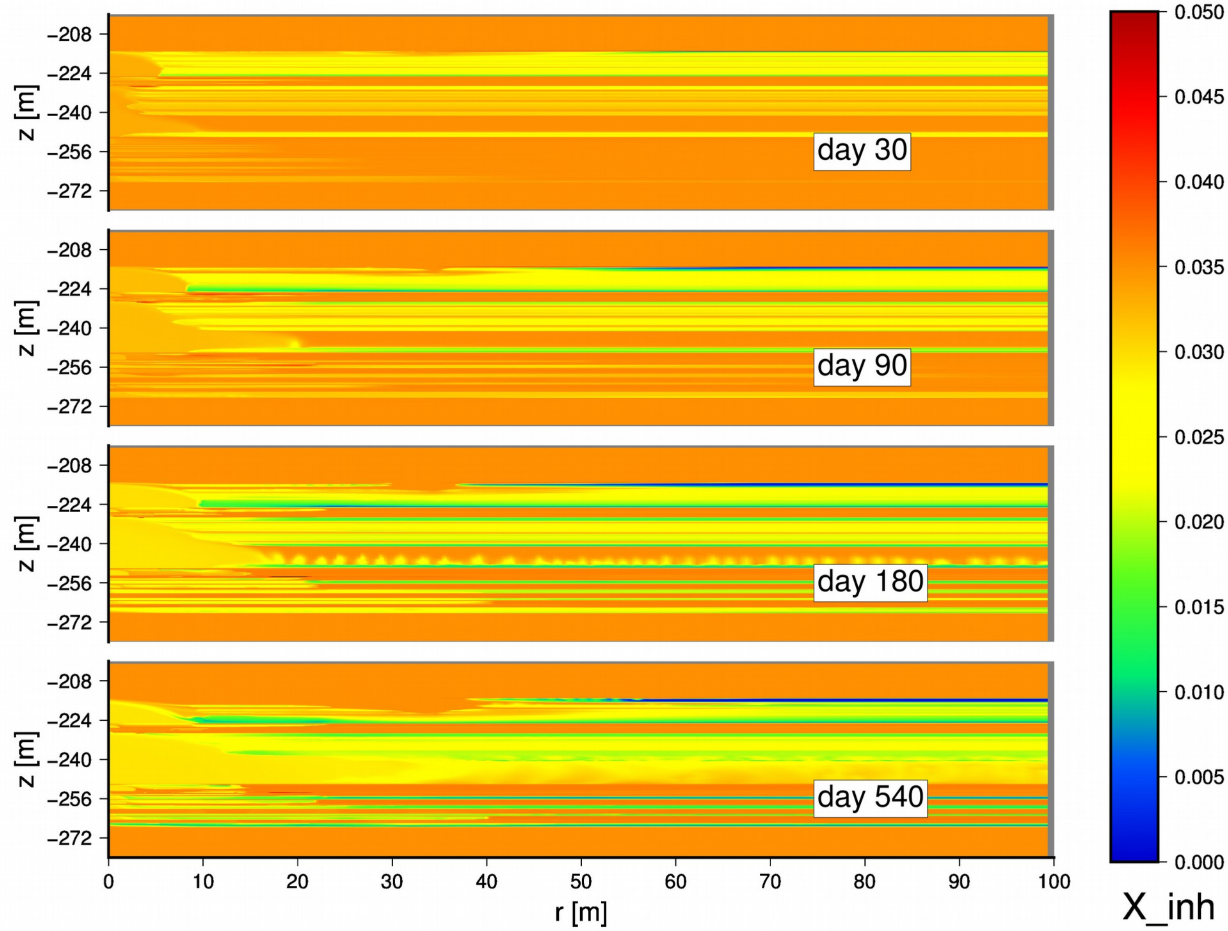

Figure 37. Case C2: Evolution of the distribution of the salt mass fraction X_S in the aqueous phase of the system during multi-well production operations at Site NGHP-02-09 of the KG Basin (P_w = 3 MPa).

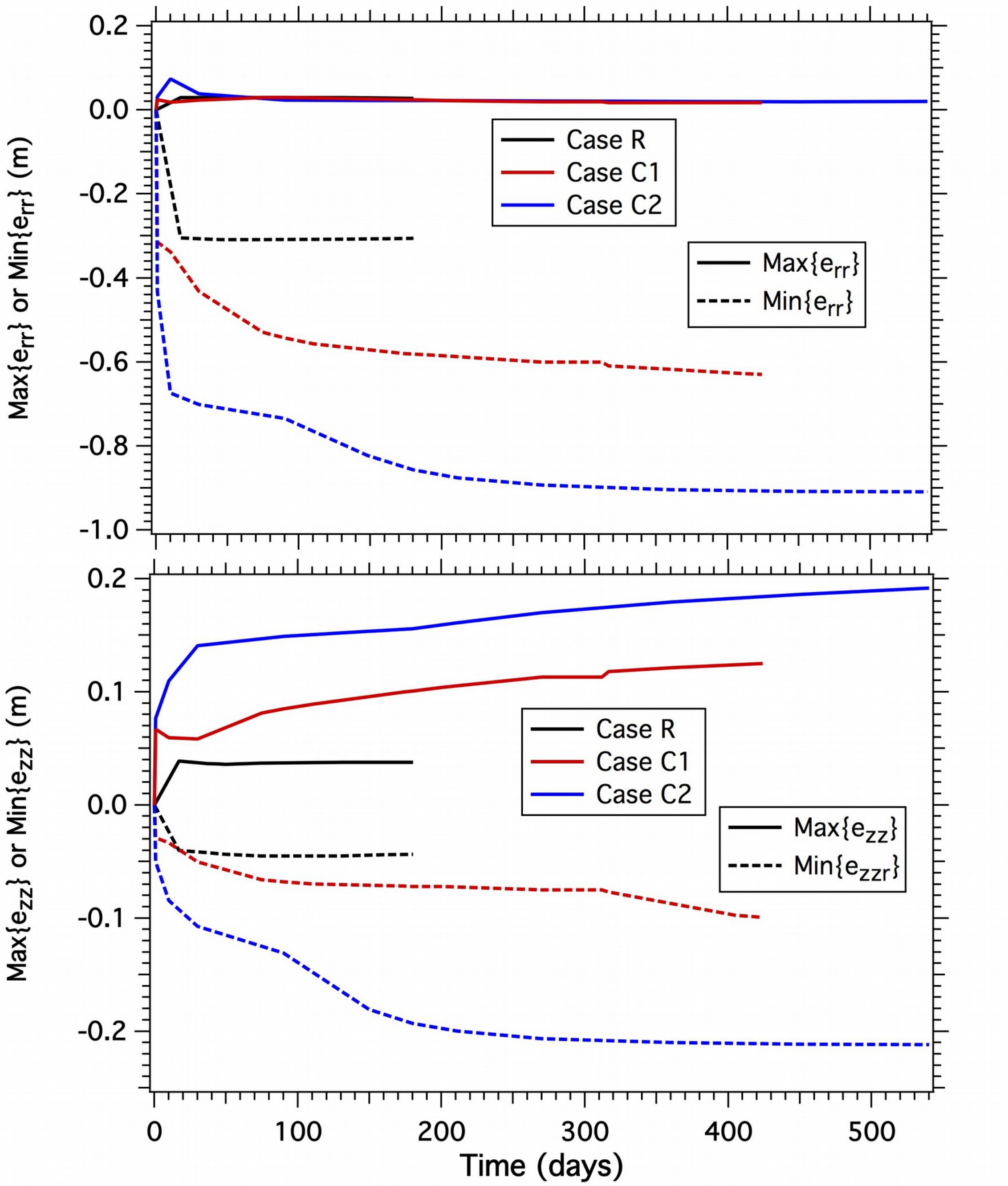

Figure 38. Evolution of maximum and minimum strains ε_{zz} and ε_{rr} in the domain in Cases R, C1 and C2.

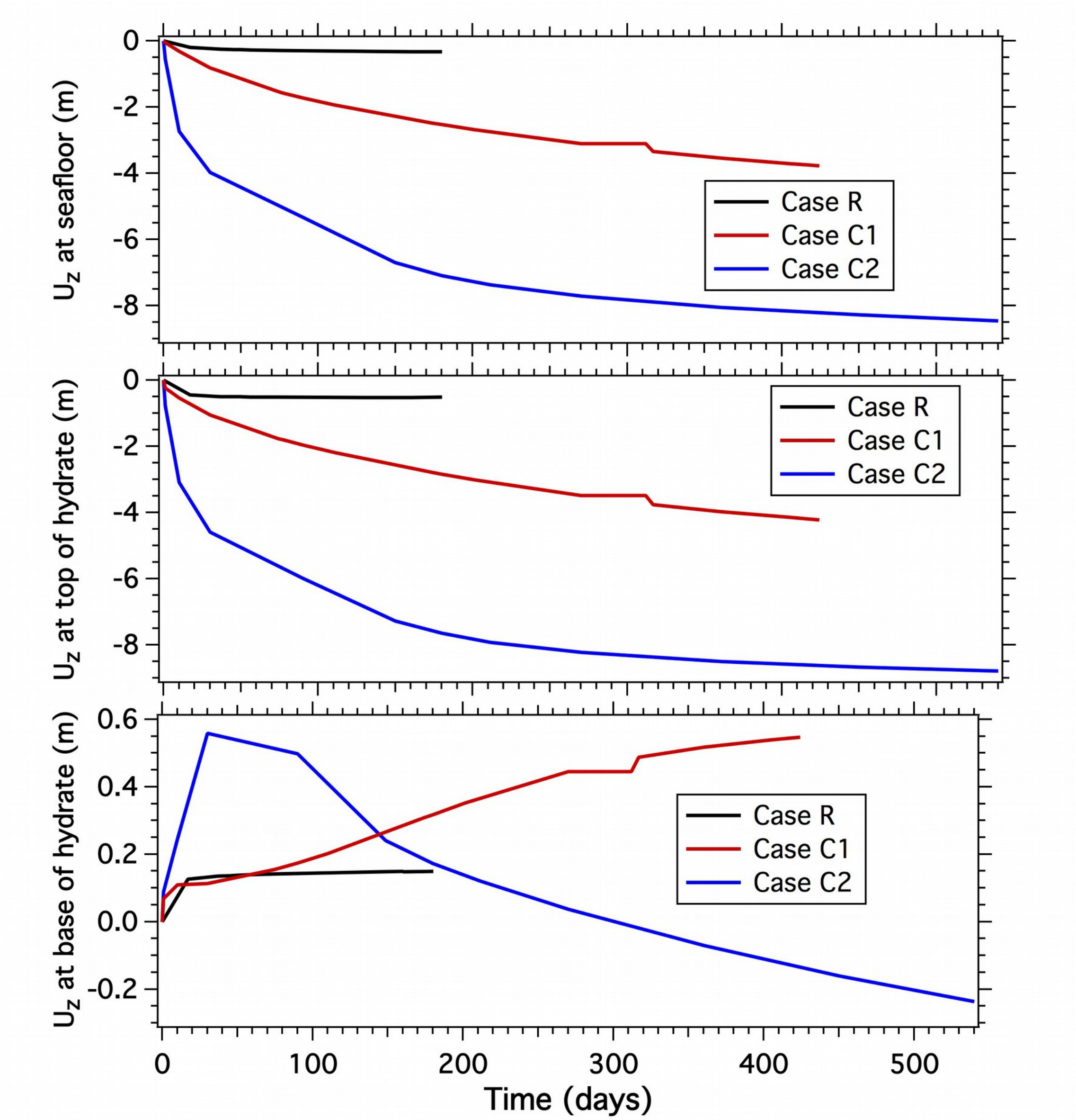

Figure 39. Evolution of displacements u_z in the vicinity of the well in the domain in Cases R, C1 and C2.

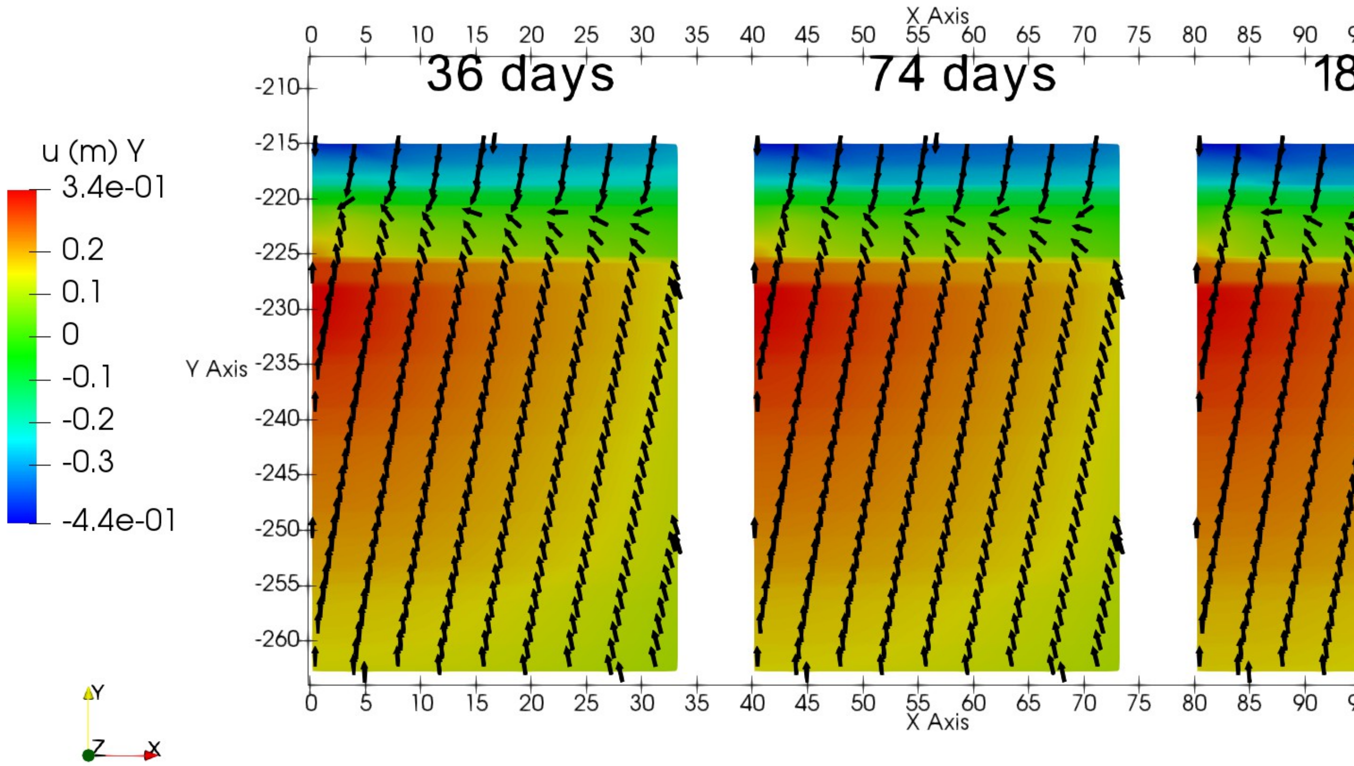

Figure 40: Evolution of the z-displacements (u_z) in Case R (open system). The arrows show the direction of the displacement. The z-coordinate (Y in the labels due to the rendering software) represents elevation in meters measured from the ocean floor and the x-coordinate represents the distance from the well. The two right images are offset by 40m and 80 m, respectively.

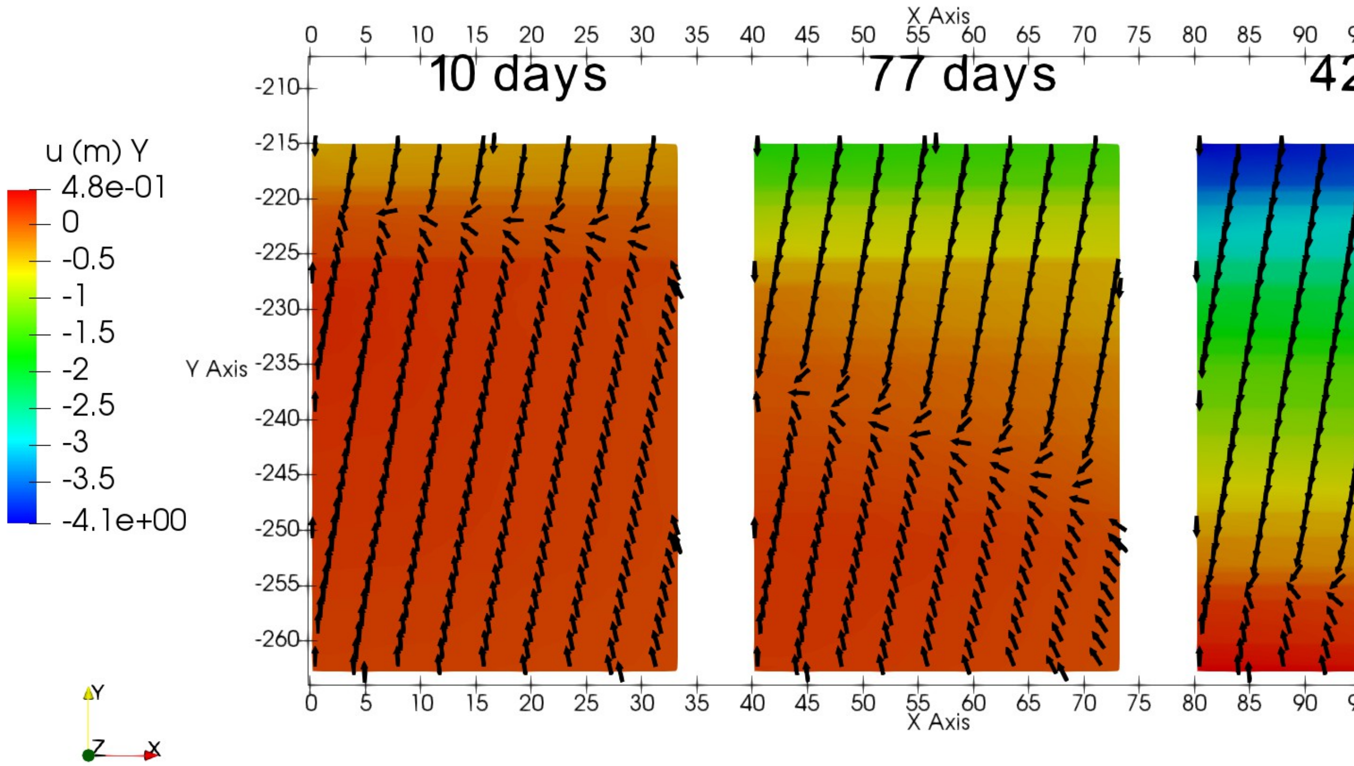

Figure 41: Evolution of the z-displacements (u_Z) in Case C1 (closed system, r = 500m). The arrows show the direction of the displacement. The z-coordinate (Y in the labels due to the rendering software) represents elevation in meters measured from the ocean floor and the x-coordinate represents the distance from the well. The two right images are offset by 40m and 80 m, respectively.

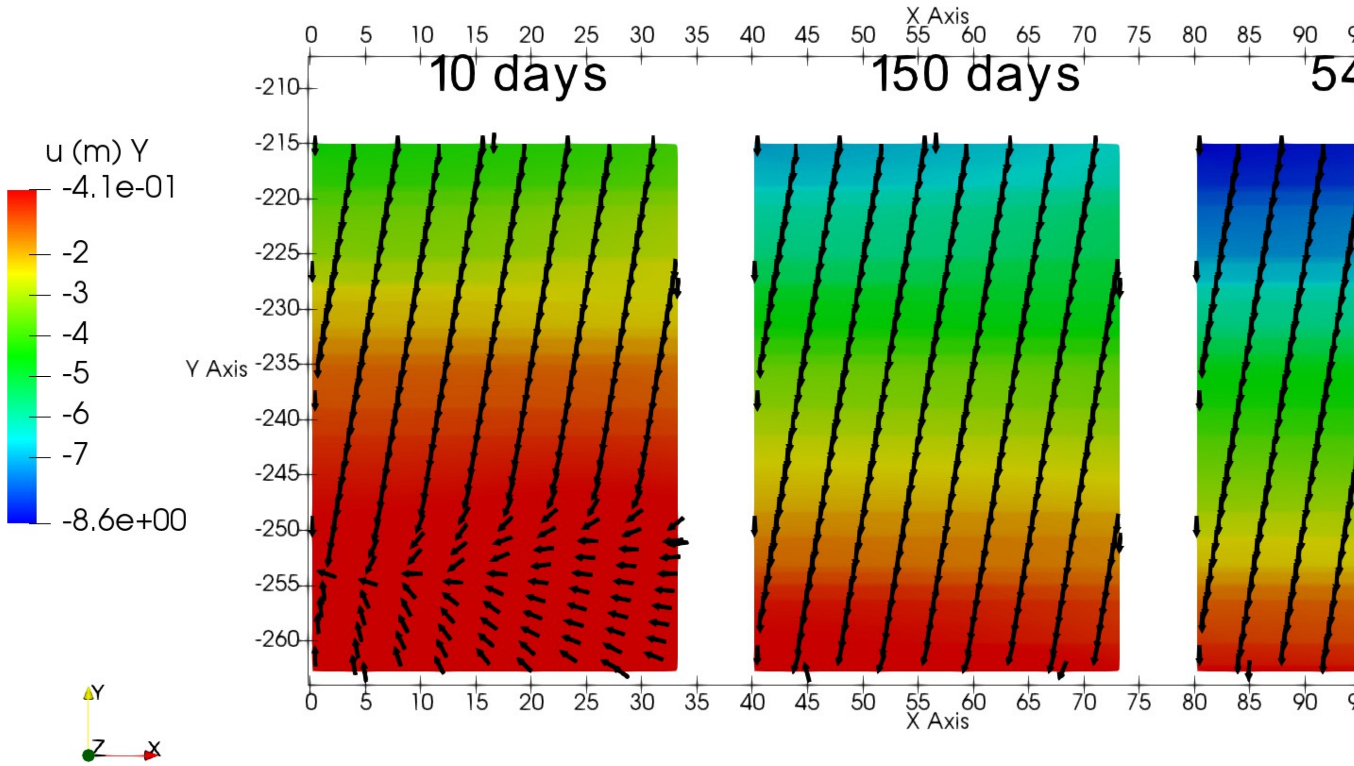

Figure 42: Evolution of the z-displacements (u_Z) in Case C2 (closed system, r = 100m). The arrows show the direction of the displacement. The z-coordinate (Y in the labels due to the rendering software) represents elevation in meters measured from the ocean floor and the x-coordinate represents the distance from the well. The two right images are offset by 40m and 80 m, respectively.

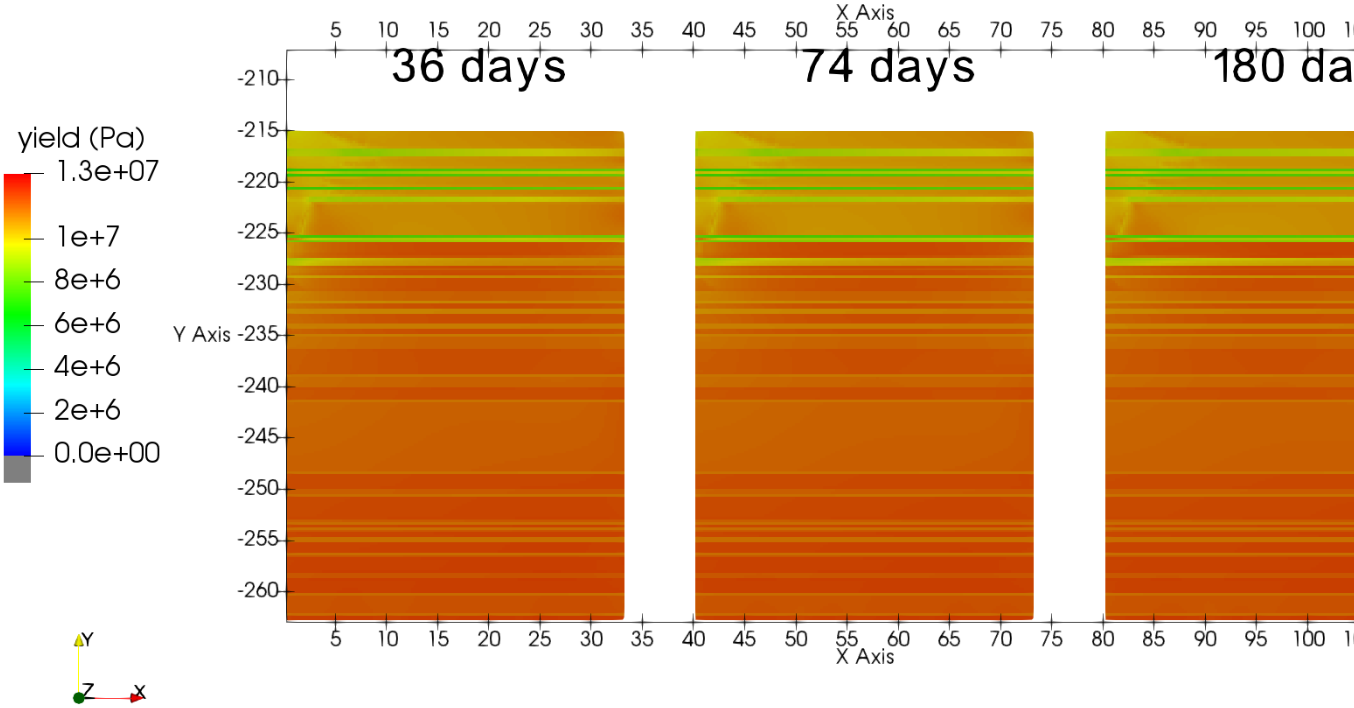

Figure 43: Evolution of the Drucker Prager yield criterion in Case R (open system). The z-coordinate (Y in the labels due to the rendering software) represents elevation in meters measured from the ocean floor and the x-coordinate represents the distance from the well. The two right images are offset by 40m and 80 m, respectively.

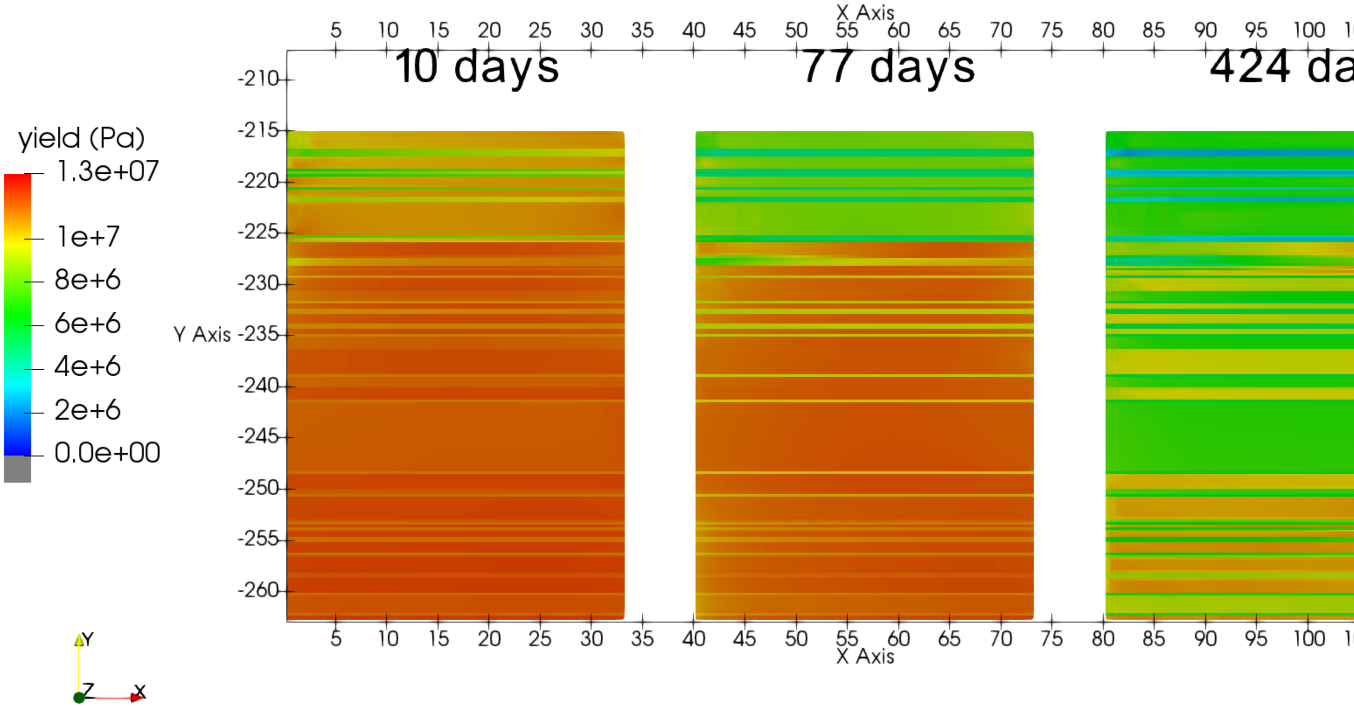

Figure 44: Evolution of the Drucker Prager yield criterion in Case C1 (closed system, r = 500m). The z-coordinate (Y in the labels due to the rendering software) represents elevation in meters measured from the ocean floor and the x-coordinate represents the distance from the well. The two right images are offset by 40m and 80 m, respectively.

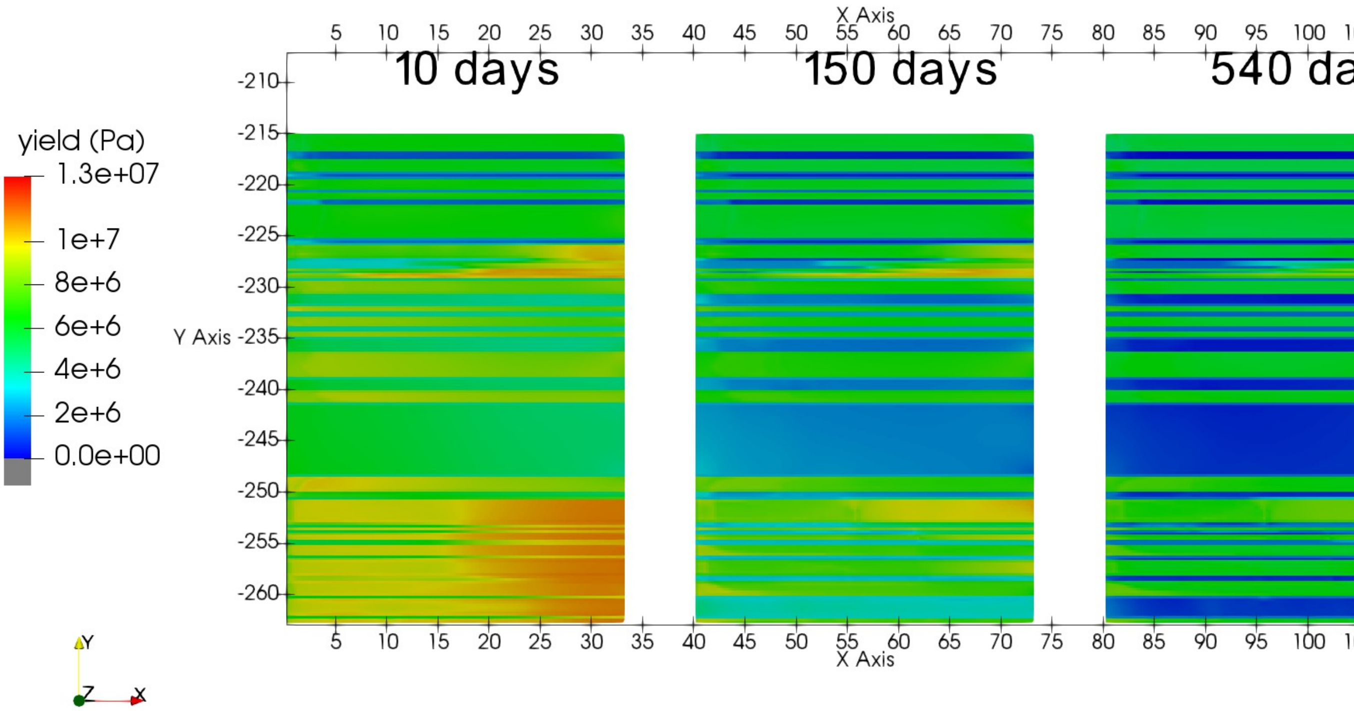

Figure 45: Evolution of the Drucker Prager yield criterion in Case C2 (closed system, r = 100m). The z-coordinate (Y in the labels due to the rendering software) represents elevation in meters measured from the ocean floor and the x-coordinate represents the distance from the well. The two right images are offset by 40m and 80 m, respectively. In this case, by the end of the simulated production time the yield criterion goes below zero in the region encircled in red and colored by gray in the color range.